Mathematical Modeling of Sinoatrial Node Dynamics at the Subcellular, Cellular, and Tissue Scales

By

EMILY E. MEYER
DISSERTATION

Submitted in partial satisfaction of the requirements for the degree of

DOCTOR OF PHILOSOPHY

in

APPLIED MATHEMATICS

in the

OFFICE OF GRADUATE STUDIES

of the

UNIVERSITY OF CALIFORNIA

DAVIS

Approved:

Timothy J. Lewis

Colleen E. Clancy

Becca Thomases

Committee in Charge

2021

Contents

Mathematical Modeling of Sinoatrial Node Dynamics at the Subcellular, Cellular, and Tissue Scales

Abstract

Cardiac pacing is an important area of scientific inquiry, and provides a rich opportunity for mathematical study due to the dynamic interplay of robustness and flexibility required for healthy function. The sinoatrial node (SAN) is key to understanding pacing, since the spontaneous periodic action potentials in the SAN pace the action potentials – and thus mechanical contraction – in the cardiac muscle tissue. However, several components of SAN function remain unclear; in the present work, we address three questions related to the rhythmicity and pacing activity of the SAN at multiple scales. First, we use model reduction and dynamical systems analysis to elucidate the rate-limiting steps in the subcellular kinetics of changes in SAN cell firing frequency resulting from sympathetic nervous system activity. This sheds light on the key biochemical factors involved in the potential arrhythmogenicity of sympathetic surges, and generates implications for pharmaceutical interventions for pathologies involving cardiac sympathetic dysregulation. Next, we apply the theory of weakly coupled oscillators to analyze the role of voltage-dependent gap junction gating on phase-locking in a differential equation model of SAN cell electrophysiology. This approach explores the potential effects of the distinct type of gap junctions in the SAN on synchrony. Finally, we use a combination of bifurcation analysis, spectral analysis, and simulations to investigate the role of size and curvature of the SAN or an ischemic region on its ability to drive action potentials in a neighboring excitable region of tissue. This elucidates how emergent properties of the physiology and geometry of a spontaneously active region impact threshold behavior for periodic propagating waves. Taken together, our results provide insight into the theoretical underpinnings for several complex processes involved in cardiac pacing, and inspiration for future computational and experimental work to apply the predictions made by our models.

Acknowledgments

I want to thank my advisor Tim Lewis for his patience, for wisdom and guidance in directing my research, and for advice on being a mathematician, being an educator, and making life decisions. Thanks for knowing when to give me creative control and when to tell me what to do, and for never trying to get me to stop prefacing my dumb questions with "this is going to be a dumb question." I appreciate your agility in adapting to my unique and dramatically changing needs throughout my PhD. I'm grateful to Colleen for all of the resources and community that you provided in the lab, for life advice and perspective, for showing me what it means to be a scientist, and for constantly guiding me to mature and grow. I'm grateful to Becca for helping me navigate the math department and providing advice on all kinds of different life situations when needed.

Thanks to Stephanie Dodson for invaluable guidance and advice on Project 3, and especially for continuing to show up during fall 2020. Thanks to Korana Burke for always providing advice and support, and for co-founding Book Club. Thanks to Rohit for including my first-year self on your trivia team, and for always providing support and guidance whenever I had a problem or concern. Thanks to the department staff, especially Tina Denena, for providing unrelenting support, help, advice, and answers to every question or challenge that arose throughout the last five years.

I've been incredibly fortunate to have opportunities to develop my very interdisciplinary academic and professional interests during my time in grad school. I owe many thanks to the FUTURE program for teaching me the strategies and tools I needed to find my dream job and then go out and get it. I'm tremendously grateful to the Writing Across the Curriculum program for taking me on as a Graduate Writing Fellow in 2019, and for the ways in which being a GWF enabled me to learn from peers across departments and to develop my understanding of the role of communication, storytelling, community and identity in academia and in science.

Lastly, I need to thank my friends inside and outside of grad school. I'm grateful to Jamie Haddock for mentoring me throughout the early years. Thanks also to Ben Schiffman, Steffen Docken, Calina Copos, and Nate Gallup for guiding and teaching me how to be a grad student. Thanks to Carter Johnson, Divya Kernik, Gonzalo Hernandez, and Adam Rose for research cameraderie, and to Sam Fleischer, Annie Laurie Mauhs-Pugh, Sabrina Enriquez, Ryan Chris Moreno-Vazquez, and Esha Datta for your friendship in the department – I wouldn't have made it without y'all. Thanks so much to Becky Neufeld for truly keeping me afloat during fall 2019, and for your incredibly generous friendship and support ever since – and for all things cat advice! I also want to thank Gabrielle Badie and Gabrielle Siegel for consistently providing encouragement and outside-of-academia perspective, and Amy Shoemaker for constantly inspiring me to be a better human.

CHAPTER 1

Introduction

As both an essential component of overall health and a complex biophysical system, cardiac physiology is an important area of scientific inquiry. Cardiac pacemaking provides an especially compelling subject for mathematical study due to the dynamic interplay of robustness and flexibility required for healthy function within an organism. The heart must beat consistently throughout the entire lifespan, maintaining blood flow throughout the body; at the same time, the frequency of contraction and volume of flow must respond adaptively to physical and situational needs, as well as to a variety of input from the autonomic nervous system.

Cardiac pacing begins in a small region in the right upper atrium known as the sinoatrial node (SAN). Cells in the SAN fire spontaneous, rhythmic action potentials, and receive input from the sympathetic and parasympathetic nervous system (SNS and PNS) that speed up or slow down their frequency. Action potentials in the SAN initiate from a "lead pacemaker site," which can shift depending on the frequency of firing, and propagate outward via cell-to-cell electrical coupling in a characteristic direction known as the conduction pathway [**10**, **46**]. These action potential waves then spread into the surrounding atrial tissue, pass through the atrioventricular (AV) node, and travel into the ventricles. In cardiac muscle cells, the triggered action potentials are coupled to mechanical contraction. The coordinated contraction of the ventricle muscle constitutes the heartbeat. In this work we apply mathematical modeling to provide a theoretical understanding of several components of the cardiac pacing process, with an emphasis on the function of the SAN. We focus on three problems in cardiac pacing at the subcellular, cellular, and tissue scales within the SAN and in its immediate vicinity.

In humans and other mammals, the physiology of cardiac pacing is modulated by the autonomic nervous system (ANS). The ANS – which consists of the sympathetic nervous system (SNS) and parasympathetic nervous system (PNS) – sends signals to the heart that result in changes to the frequency of the heartbeat and the contractility of the cardiac muscle. This signaling is accomplished by, in the PNS, nerves that project directly through the vagus nerve into the heart and form synapses directly onto cardiac cells. The SNS forms a multi-layered network consisting of neurons that project from the brainstem to ganglia just outside the spinal cord, neurons that conduct signals within and between the paravertebral ganglia, and postganglionic neurons that project to the heart and form synapses onto cardiac cells [**29**, **36**]. It is estimated that each cardiac cell, including those in the SAN as well as in the atrial and ventricular tissue, receives synaptic input from efferent neurons [**23**, **75**]. The ANS uses this synaptic signaling, with several points of feedback in the SNS and PNS networks, to influence cardiac output in response to the situational needs of the organism, such as increased heart rate in the presence of a perceived threat.

Dysregulated SNS activity, including elevated abrupt-onset sympathetic activity in heart failure, is known to be associated with exacerbation of prior heart failure and sudden cardiac death [**12**,**49**]. The cardiac cellular response to SNS activity results in increased production of the second messenger cyclic AMP (cAMP), which leads to changes to the electrophysiological properties of the cell. Therefore, cAMP is likely involved in the arrhythmogenicity of SNS signaling in pathological settings. However, the mechanisms governing the kinetics of cAMP concentration changes in cardiac cells are not well understood. In Chapter 2, we apply model reduction and analysis to investigate the rate-limiting steps modulating the transduction of stimuli from the SNS into electrophysiological changes via increased cAMP concentration in a cardiac cell. This work was published in *Journal of Theoretical Biology* in 2021 [**45**].

In the SAN, numerous cell types are present including intrinsically oscillatory SAN cells with heterogeneous electrophysiological properties; atrial or atrial-like cells; and fibroblasts [**41**,**51**]. However, cells in the SAN must achieve synchrony in order to successfully pace

the cardiac muscle tissue. Current conduction between cells in the SAN and throughout the heart relies on current transfer through electrical coupling between individual cells. Such cell-to-cell electrical coupling is primarily accomplished by gap junctions, which are plaques formed at the interface between adjacent cell membranes containing multi-protein channels through which ions can travel betwee adjacent cells. Several distinct types of gap junctions are expressed differentially across regions of the heart; in particular, the SAN predominantly contains connexin 45 (Cx45) gap junctions, whereas connexin 43 (Cx43) gap junctions are much more common throughout the atria and ventricles [**15**, **18**]. Although the functional role of these differences in expression of gap junction type is not known, one prominent factor distinguishing the function of gap junction types is the dependence of conductance on junctional voltage, i.e., the difference in membrane potential between the two coupled cells. Voltage-clamp studies show that the conductance across gap junctions is maximized when the membrane potentials of the two adjacent cells are similar; as the difference between membrane potentials increases, the conductance across the gap junction decreases. Conduction through Cx45 gap junctions displays a steeper dependence on junctional voltage than does conduction across Cx43 gap junctions, and a narrower window of junctional voltage in which the conductance is close to its maximal value. In Chapter 3, we examine the potential role of voltage-dependent coupling between cells in the SAN by applying the theory of weakly coupled oscillators to SAN cells.

Action potentials originate in and around the central area of the crescent-shaped SAN, but the precise location of first activation shifts along the superior-inferior axis of the node as the frequency of oscillations changes [**3**, **8**]. These action potentials propagate outward in a particular direction, passing into the surrounding atrial tissue through a limited number of "exit sites" [**21**, **44**, **58**]. This restricted pathway may be due to anatomical barriers, a lack of coupling between SAN cells and atrial tissue, or emergent properties of the physiology and geometry of the SAN [**46**]. Outside the SAN, ischemia or infarction can cause a

region of tissue in the myocardium to become spontaneously active and to produce electrical waves [**27**, **61**], which constitute dangerous and often fatal arrhythmias. Conventional understanding suggests that electrical waves propagate more rapidly from stronger "source" regions, including regions of higher negative curvature due to their higher area and therefore greater quantity of current as compared with regions of positive curvature [**66**]. However, recent work using both *in vitro* experiments and a combination of mathematical analysis and computational simulation contradicts this argument, suggesting that positive curvature may *increase* the propensity for a spontaneously active electrical source region to produce periodic waves [**69**]. In Chapter 4, we use dynamical systems approaches including bifurcation theory as well as PDE linearization and spectral analysis to study the effects of the shape and curvature of the SAN, or of an ischemic region, on the propagation of action potentials into the surrounding tissue.

Our work provides insight into the theoretical underpinnings of several components of the cardiac pacemaking process. The results of Chapter 2 identify the key regulatory components of the process by which the SNS accelerates heart rate and generate predictions for cardiac disease and treatment. The results of Chapter 3 suggest that the impact of voltage-dependent gating on cell-to-cell synchrony does not justify the presence of distinct populations of gap junctions in different regions of the cardiac conduction pathway. Instead, the distinct expression of gap junctions in different regions of the heart might allow for differential modulation of gap junctions by the downstream products of SNS signaling, as suggested in [**39**]. Finally, the results in Chapter 4 demonstrate that in the SAN, or any spontaneously active region of tissue, the electrical excitability and the size and shape of the region interact in a complex manner to determine the (in)stability of stationary solutions and of periodic, propagating waves. Taken together, our results provide inspiration for future computational and experimental work to apply the predictions made by our models to more realistic settings.

CHAPTER 2

Dynamics of Adrenergic Signaling in Cardiac Myocytes and Implications for Pharmacological Treatment

This work was published in Journal of Theoretical Biology in 2021 [**45**].

Abstract

Dense innervation of the heart by the sympathetic nervous system (SNS) allows cardiac output to respond appropriately to the needs of the body under varying conditions, but occasionally the abrupt onset of SNS activity can trigger cardiac arrhythmias. Sympathetic activity leads to the release of norepinephrine (NE) onto cardiomyocytes, activating β_1-adrenergic receptors (β_1-ARs) and leading to the production of the second messenger cyclic AMP (cAMP). Upon sudden activation of β_1-ARs in experiments, intracellular cAMP can transiently rise to a high concentration before converging to a steady state level. Although changes to cellular cAMP concentration are important in modulating the overall cardiovascular response to sympathetic tone, the underlying mechanisms of the cAMP transients and the parameters that control their magnitude are unclear.

We reduce a detailed computational model of the β_1-adrenergic signaling cascade to a system of two differential equations by eliminating extraneous variables and applying quasi-steady state approximation. The structure of the reduced model reveals that the large cAMP transients associated with abrupt β_1-AR activation are generated by the interplay of production/degradation of cAMP and desensitization/resensitization of β_1-ARs. The reduced model is used to predict how the dynamics of intracellular cAMP depend on the concentrations of norepinephrine (NE), phosphodiesterases 3 and 4 (PDE3,4), G-protein

coupled receptor kinase 2 (GRK2), and β_1-AR, in healthy conditions and a simple model of early stages of heart failure.

The key findings of the study are as follows: 1) Applying a reduced model of the dynamics of cardiac sympathetic signaling we show that the concentration of two variables, cAMP and non-desensitized β_1-AR, capture the overall dynamics of sympathetic signaling; 2) The key factors influencing cAMP production are AC activity and PDE3,4 activity, while those that directly impact β_1-AR phosphorylation are GRK2 and PKA_1. Thus, disease states that affect sympathetic control of the heart can be thoroughly assessed by studying AC activity, PDE3,4, GRK2 and PKA activity, as these factors directly impact cAMP production/degradation and β_1-AR (de)phosphorylation and are therefore predicted to comprise the most effective pharmaceutical targets in diseases affecting cardiac β_1-adrenergic signaling.

2.0.1. Key Words. sympathetic nervous system; cyclic AMP; heart failure; β-blockers; mathematical model

2.1. Introduction

Activity of the sympathetic nervous system (SNS) modulates overall cardiovascular function: in healthy mammals, heart rate and contractile force adapt dynamically in response to sympathetic activity. However, dysregulation of the SNS has been linked to proarrhythmia and heart failure [**22**, **42**, **57**, **70**]. Enhanced sympathetic activity is associated with exacerbation of prior heart failure and sudden cardiac death [**12**, **49**]. The changes resulting from the onset of SNS activity require cardiomyocytes to increase their production of the second messenger cyclic AMP (cAMP), which suggests that cAMP is an important component of the cardiac response to the SNS in physiological and pathological conditions. It is therefore critical to understand the dynamical mechanisms of adrenergic signaling in cardiac myocytes and how this signaling modulates cellular cAMP levels in health and disease.

Cardiac modulation by the SNS occurs via the release of epinephrine and norepinephrine (NE) from sympathetic neurons directly onto cardiac myocytes expressing β-adrenergic receptors (β-ARs). The heart is densely innervated, such that individual cardiac cells in both the conduction pathway and the myocardium receive synaptic input from the SNS [**23**, **75**]. Cardiac cells predominantly express β_1-adrenergic receptors (β_1-ARs), which bind synaptic NE or adrenergic agonist and induce changes to electrophysiology and contractility. The activation of β_1-ARs modulates an intracellular signaling pathway that, when activated, stimulates adenylyl cyclases 5 and 6 to increase production of cyclic AMP (cAMP), releasing the catalytic subunit of protein kinase A (PKA) to phosphorylate cellular targets (Figure 1). Activated PKA phosphorylates delayed rectifier potassium channels I_{Kr} and I_{Ks}, L-type calcium channels, and troponin I, as well as both ligand-bound and unbound β_1-ARs, which are desensitized by phosphorylation. Ligand-bound receptors are also selectively phosphorylated and desensitized by G-protein coupled receptor kinase 2 (GRK2).

Although the mechanisms for sympathetic-induced arrhythmias are not fully understood, it is known that the effects of SNS activity are largely mediated through changes at a cellular scale, which occur via changes to the concentration of cAMP in individual myocytes. In single cells, β_1-adrenergic activity can increase the propensity for arrhythmias by various means: enhancement of late sodium current or L-type calcium current increases the risk of EADs [**14**,**74**], especially in long-QT syndrome (LQTS) in cells with I_{Ks} block or I_{Kr}/I_{Ks} mismatch [**4**, **63**, **73**], while increased calcium influx increases the propensity for DADs [**5**]. At the scale of the organ, the cellular changes induced by β_1-AR activation can be arrhythmogenic in various pathologies including LQTS, myocardial infarction, atrial fibrillation, and heart failure [**24**], and it is estimated that roughly 50% of sudden deaths in heart failure are due to electrophysiological aberrations [**16**, **33**]. Since each of these arrhythmogenic processes depends on the excess production of cAMP via β-adrenergic signaling, it is essential to decipher the key dynamical mechanisms of the kinetics of the β_1-AR biochemical cascade.

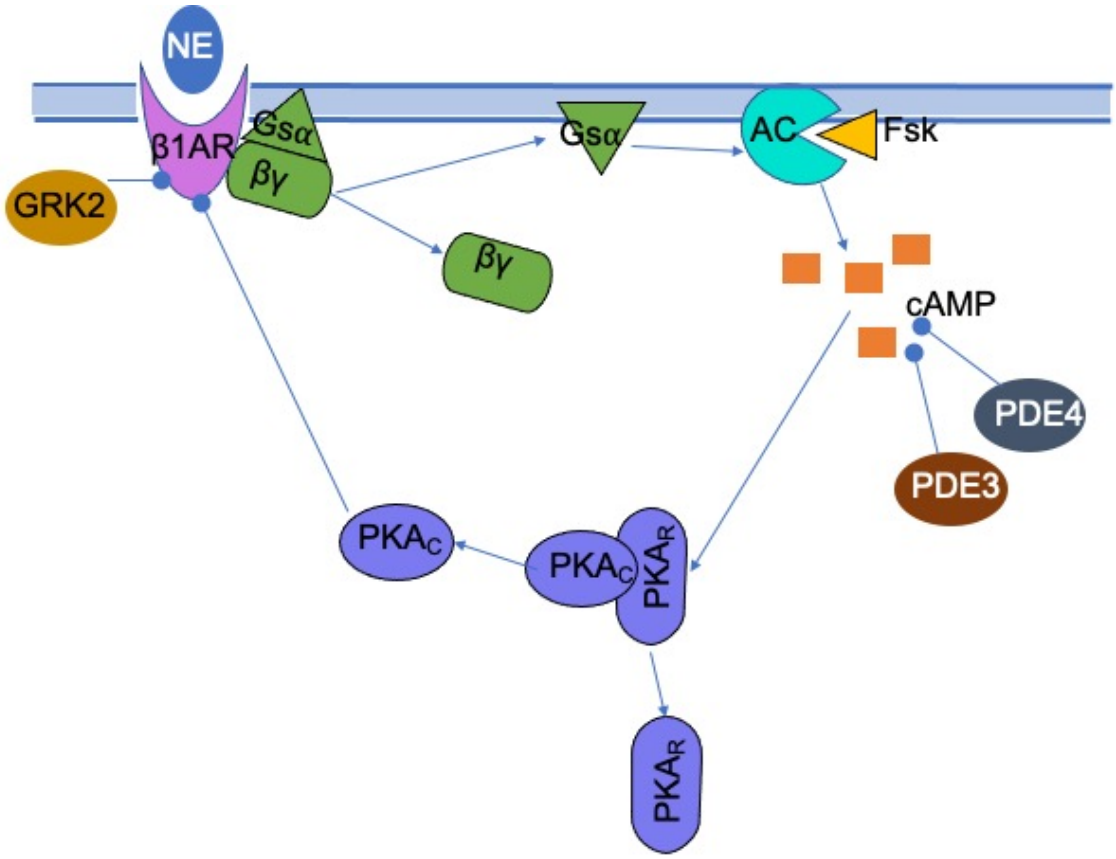

FIGURE 2.1. The release of norepinephrine activates a biochemical signaling pathway that results in intracellular physiological changes in a cardiac myocyte. The adrenergic agonist binds to a β_1-AR, which activates the Gs_α subunit to stimulate adenylyl cyclases V and VI (AC), which then produces cAMP. cAMP activates PKA, the catalytic subunit (PKA_C) of which phosphorylates numerous targets including the β_1-AR, potassium channels, calcium channels, ryanodine receptors, phospholamban, and troponin I. Meanwhile, cAMP is degraded by phosphodiesterase 3 and 4 (PDE3, PDE4).

To elucidate the dynamics of cAMP in cardiac cells, it is necessary to analyze the kinetics of the transduction of a sympathetic stimulus from β_1-AR activation to the increased production of cAMP and resulting active PKA. Upon sudden and prolonged activation of β_1-adrenergic receptors, as occurs during a sympathetic surge, cAMP increases over one to two minutes and then gradually decreases to an intermediate level [**60**]; the maximum achieved during the transient rise is often markedly higher than the final steady state. We refer to this transient cAMP over-elevation during the initial phase of the stimulus as "overshoot". It is of interest to identify biological parameters that modulate overshoot, and how these

parameters may be manipulated to change the amplitude of the large overshoots in cAMP concentration while maintaining the functional dynamic range of physiological output – that is, the range of attainable steady state cellular concentrations of cAMP. Mathematical modeling is a useful tool to analyze the mechanisms responsible for the temporal complexity of cAMP concentration in cardiac myocytes and to explore the changes in parameters that influence the dynamics of this behavior. Of the biophysically detailed computational models for the adrenergic signaling cascade in myocytes that have been constructed, perhaps most widely used is the Soltis-Saucerman model [**59**, **60**, **65**], which connects β-AR signaling with electrophysiology in rabbit ventricular myocytes, including the processes outlined above and depicted in fig. 2.1. Although the Soltis-Saucerman model is for ventricular cells rather than SAN cells, a more complex but nonetheless cAMP-dependent mechanism exists in SAN cells (see [**38**], esp. fig. 1B); therefore, these results shed light on the kinetics of the increase in frequency in SAN cells as a result of SNS activity.

The present work uses the Soltis-Saucerman model as a foundation, owing to its biophysical detail, and aims to simplify this model to identify the rate-determining processes for the kinetics of the adrenergic signaling pathway. We use dimension reduction techniques to reduce the signaling subsystem of the original model to a two-dimensional system of differential equations. We then use phase plane techniques to analyze the mechanisms of overshoot in cAMP concentration and to identify ways to modify the amplitude of the overshoot, as well as to clarify the general relationships between parameters and outcomes of cAMP production across a range of conditions. Finally, we note that GRK2 is both known to interact with a variety of targets [**53**] and associated with cardiac pathology [**43**]. It is not known whether the effects of GRK2 overexpression and inhibition are mediated by adrenergic signaling or by other targets. Given that downregulation of GRK2 has been proposed as a synergistic therapy alongside β-blockers [**13**, **47**], we consider the potential mechanisms by which changes to GRK2 activity might impact cellular cAMP signaling. Analysis of these mechanisms in the two-variable model using the phase plane elucidates how concurrent GRK2 inhibition

might modify the effects of β-blockers on myocytes. Our results suggest that a simplified two-dimensional model can capture the extent to which the isolated adrenergic signaling pathway mediates both the potentially harmful effects of GRK2 in heart failure and the therapeutic benefits of its downregulation by pharmaceutical agents.

2.2. Model of β_1-adrenergic signaling pathway

The Soltis-Saucerman model for electrophysiology [**59**, **60**, **65**] uses a system of mass-action-based differential equations to simulate the processes of electrophysiology, calcium flux, and signaling from CaMKII and the sympathetic nervous system in a rabbit ventricular myocyte. We isolate the β-adrenergic signaling subsystem of the Soltis-Saucerman model, which stands alone and does not receive feedback from the downstream cellular targets or other model components.

The adrenergic signaling portion of the Soltis-Saucerman model contains sixteen variables (see Appendix A.1) that model the sequence of biochemical reactions triggered by the binding of norepinephrine (NE) or an adrenergic agonist to a β_1-adrenergic receptor and lead to the activation of PKA. Seven of the variables are governed by differential equations. Of these seven dynamic variables, two variables are "read-out" components that do not affect other variables; two other variables can be removed using the conservation conditions, and a fifth variable can be removed by exploiting separation of time scales and setting the variable to its quasi-steady state. The resulting reduce system has two dynamics variables: the concentration of cAMP (c) and the concentration of non-desensitized β_1-AR (β). The algebraic equations for variables in pseudo-equilibrium are left unchanged. A detailed description of the model reduction in presented in Appendix A.2.

The two-dimensional system of differential equations that describes β_1-adrenergic signaling is:

$$
\begin{aligned}
(2.1) \qquad \frac{d\beta}{dt} &= p_{10}(\beta_{tot} - \beta) - p_9 \beta PKA_{c_1}(c) - F_1(\beta; L_{tot}) \\
\frac{dc}{dt} &= \left(\frac{p_{15}p_{20}}{p_{15} + p_{23}}\right) AC_b(\beta; L_{tot}) + \left(\frac{p_{15}p_{21}}{p_{26}(p_{15} + p_{23})}\right) AC_s(\beta; L_{tot}) \\
&\quad - \left(\frac{p_{16}p_{28}c_f(c)}{p_{29} + c_f(c)} + \frac{p_{17}p_{30}c_f(c)}{p_{31} + c_f(c)}\right)
\end{aligned}
$$

where L_{tot} is the total concentration of norepinephrine (NE) or adrenergic agonist; β_{tot} is the total concentration of β_1-ARs; F_1 is the rate of β_1-AR desensitization by GRK2; c_f is the concentration of "free" cAMP (not bound to PKA); p_9 is the rate constant of β_1-AR desensitization by PKA; p_{10} is the resensitization rate of phosphorylated β_1-AR; p_{15} is cellular ATP concentration; and p_{16}, p_{17}, p_{20}, p_{21} and p_{23} are rate constants and saturation constants associated with production of cAMP by AC and degradation of cAMP by PDE3 and PDE4. Details of the functions PKA_{c1}, F_1, AC_b, AC_2 and c_f are provided in the appendix. Parameters were unchanged from the full model described in [**59**] and [**60**], except in specific cases described in sections 4.3-4.5. Simulations were performed in MATLAB using `ode15s`, and algebraic equations were solved using the `fsolve` root-finding algorithm with appropriate initial conditions.

The reduced model captures the four dynamic processes that govern the temporal dynamics of β_1-adrenergic signaling: (1) the terms $\left(\frac{p_{15}p_{20}}{p_{15}+p_{23}}\right) AC_b(\beta; L_{tot})$ and $\left(\frac{p_{15}p_{21}}{p_{26}(p_{15}+p_{23})}\right) AC_s(\beta; L_{tot})$ model the rate of production of cAMP by adenylyl cyclases V and VI at a basal rate and a rate stimulated by $G^{GTP}_{s,\alpha}$; (2) the terms $\left(\frac{p_{16}p_{28}c_f(c)}{p_{29}+c_f(c)} + \frac{p_{17}p_{30}c_f(c)}{p_{31}+c_f(c)}\right)$ model the rate of degradation of cAMP by phosphodiesterases 3 and 4; (3) the terms $p_9 PKA_{c_1}(c)\beta + F_1(\beta; L_{tot})$ model the rate of desensitization of β_1-ARs by PKA and by GRK2, respectively; and (4) the term $p_{10}(\beta_{tot} - \beta)$ models the rate of resensitization of desensitized β_1-ARs. Details of the functions PKA_{c1}, F_1, AC_b, AC_2 and c_f are provided in Appendix A.2.

We validate the reduced model by comparing its predictions against those made by the full model for cAMP and non-desensitized β_1-AR concentrations, as well as for concentrations

of PKA and other components of the signaling pathway, under the abrupt application and removal of NE. As shown in the example in fig. **??**, the reduced model (red dashed curves) exhibits behavior almost indistinguishable from the full model (blue curves). This excellent agreement between the full model and the reduced model holds across a wide range of NE concentrations (0.001-10 μM) and parameter regimes (see Appendix A.3, fig. A.2).

2.3. Results

2.3.1. Reduced Model Behavior. When norepinephrine or adrenergic agonist is added to a ligand-free system (fig. 2.2), the concentration of non-desensitized β_1-ARs gradually decays over tens of minutes (fig. 2.2A). Cellular concentration of cyclic AMP increases over a period of approximately 1 minute, reaching a transient maximum, and then gradually decreases to an intermediate value between the ligand-free resting state and the maximal concentration (fig. 2.2B). In particular, fig. 2.2 depicts the "overshoot" phenomenon that occurs when the initial condition is the steady state for the ligand-free system, and a high dose of 100 nM NE is added.

2.3.2. Phase Plane Analysis. We further examine the underlying mechanisms for the dynamics of the system by using the phase plane, which divides state space into regions where the variables each increase and decrease. The curves or "nullclines" delineating these regions are the zero contours for the derivatives of each dynamic variable. The resulting half-planes on either side of each nullcline form the regions of increase and decrease for each variable; the full plot is called a phase plane.

Figure 2.3 shows the phase plane for the reduced signaling model (2.1) both in the NE-free condition (NE−) and in the presence of high NE or adrenergic agonist concentration (NE+). With no agonist (fig. 2.3B), the cAMP nullcline is nearly horizontal, while the β nullcline is approximately vertical, and there is one stable steady state at their intersection. The cAMP variable c changes more rapidly than does concentration of non-desensitized β_1-ARs, so that the system initialized away from the steady state reaches the c nullcline first

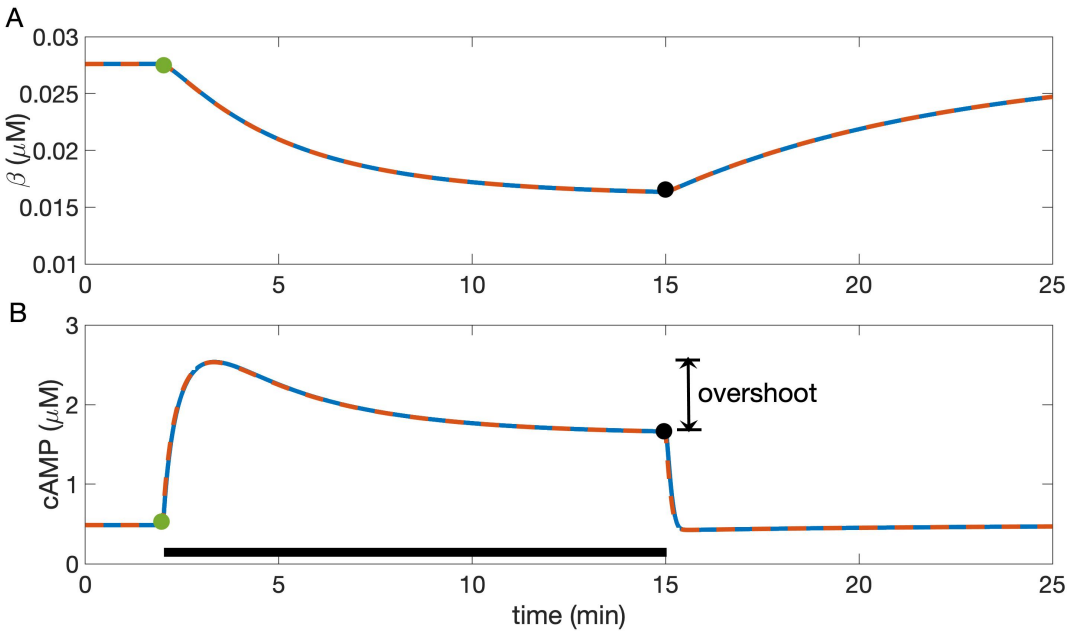

FIGURE 2.2. Predictions for cellular response to a change from basal conditions to 100 nM NE and subsequent return to 0 NE in the full (solid blue line) and reduced (dashed red line) Soltis-Saucerman model. Agonist is applied from 2 to 15 minutes of the simulation (black bar in B). A: both models predict a slow decrease in β upon application of NE, followed by a slow increase when NE is removed. B: in both models, cyclic AMP concentration transiently increases for 1-2 minutes and then gradually decays to a steady state in the presence of a high NE concentration. Overlay includes the trajectory from fig. S1, panel A in [**60**] and data (circles), taken from [**28**]. Vertical double-arrow depicts "overshoot," the difference between transient maximum and elevated steady state. Removal of NE leads to a small undershoot and return to the basal steady state. The models show nearly identical outputs, indicating that the reduction does not substantially change predictions. Green and black circles indicate steady-state values of variables for NE- and NE+ conditions, just preceding application and removal of NE respectively (see fig. 2.3).

before slowly tracing this nullcline to the global steady state. This transition is depicted by the green trajectory in fig. 2.3A.

The cAMP and β_1-AR nullclines shift in response to changes to the ligand concentration. When agonist concentration increases suddenly from 0 to 100 nM, as in the transition from fig. 2.3B to 2.3A, the slope of the cAMP nullcline increases and the β_1-AR nullcline moves to the left in the phase plane. Because c changes much more rapidly than β, the state of the system first moves almost vertically in the phase plane towards the cAMP nullcline, then

traces this nullcline downward to the new global steady state as β adjusts more slowly (green curve in fig. 2.3A). Note that the steepness of the cAMP nullcline under high-NE conditions paired with the difference in time scales between the dynamics of c and β creates the cAMP "overshoot" as the system evolves from the initial condition at the NE- steady state to the new at NE+ steady state. The magnitude of overshoot can be estimated by the vertical difference in (β, c) state space between the NE- steady state and the corresponding point on the cAMP nullcline in the NE+ condition (vertical difference between green circle and red curve in fig. 2.3A). Note that this metric consistently overestimates the the magnitude of the overshoot, but it enables a direct, mechanistic analysis of the relationships between parameters and cAMP dynamics, and it can provide an efficient approximation over a broad range of parameter conditions (e.g., the maximal error of the approximation in the result presented below is 20%).

The "dynamic range" of the β_1-AR signaling pathway can be defined as the difference between the steady state cAMP concentration with no NE and the steady state with a high dose of NE. Under default parameter conditions, the dynamic range of cAMP is approximately 1 μM (difference in cAMP between green and black circles in fig. 2.3A and B). This range measures the overall responsiveness of the cell to adrenergic input. Moreover, this measure provides a relative estimate of the responsiveness of overall cardiac response to sympathetic tone, as heart rate increases with cAMP concentration.

2.3.3. Norepinephrine and Phosphodiesterase Modulate cAMP Overshoot. Phase plane analysis can be used to efficiently quantify the relationship between cellular conditions and predicted outcomes, and to directly show how these outcomes depend on the steady-state relationships between the two variables. We selected parameters important to the four dynamic processes that affect the two-variable model: total phosphodiesterase concentration, total β_1-AR concentration, and β_1-AR GRK2 desensitization rate constant (k_{GRK2}). As in section 3.2, we approximated overshoot as the vertical difference in (β, c) state

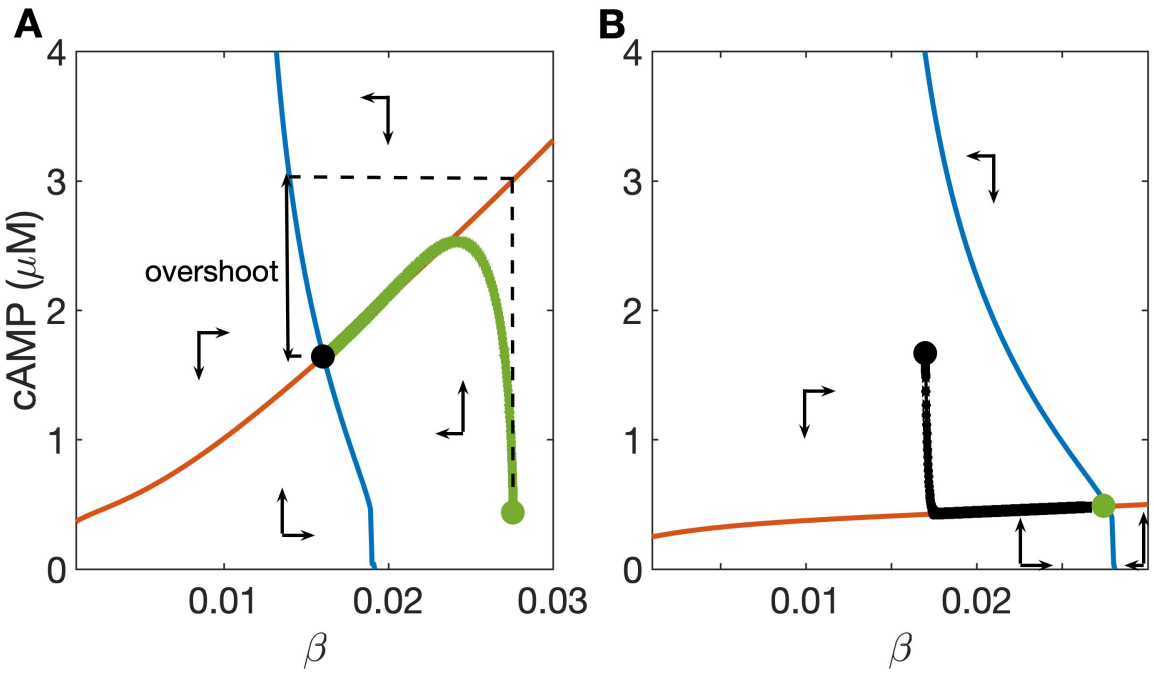

FIGURE 2.3. Phase plane for the two-variable reduced model: cAMP nullcline (red) and β nullcline (blue) divide state space into regions where cAMP concentration and active β_1-AR concentration increase and decrease (see text). A: high dose, 100 nM NE; B: NE-free condition. Synaptic NE concentration changes the slope of the cAMP nullcline and the position of the β nullcline. Green and black circles are located at the steady states for the NE-free and high-dose NE conditions, respectively, and used as initial data for the alternate condition, producing the trajectories corresponding to the solutions shown in fig. 2.2. Vertical arrow depicts the "overshoot," in which the nearly vertical rise to the cAMP nullcline precedes a slower decay to the NE+ steady state. Note that cAMP concentration changes more rapidly than does the β concentration, leading to overshoot when the cAMP nullcline moves abruptly. The amplitude of the overshoot can be estimated by the height of the cAMP nullcline at the NE- steady state (i.e., vertical distance between green circle and red curve in A). The vertical difference between NE+ and NE- steady states (green and black circles) represents "dynamic range", i.e. cellular responsiveness to ligand.

space between the NE- steady state and the corresponding point on the cAMP nullcline in the NE+ condition (e.g. vertical difference between green circle and red curve in fig. 2.3A).

As shown in fig. 2.4A, with default parameters, overshoot amplitude increases markedly with NE concentration up to [NE] $\approx$ 100 nM, beyond which both the maximum and steady-state cAMP concentration saturate with respect to NE concentration (fig. 2.4 A). The

dynamics of cAMP concentration are modulated by phosphodiesterases 3 and 4, depicted in fig. 2.4B-D. Default PDE bulk concentration was taken to be 0.072 μM, as in [**59**] and [**60**]. Increased PDE concentration (0.144 μM) reduces the slope of the high-NE cAMP nullcline (fig. 2.4C). This diminishes the amplitude of cAMP overshoot, as the maximal cAMP concentration reached in the NE+ case is close to the steady state for the NE- case. Moreover, increased PDE concentration reduces the steady states and maximal cAMP concentrations over a broad range of NE concentrations, including at very high NE (fig. 2.4B). Thus, the dynamic range of cAMP concentration, and therefore the responsiveness of the cell to a range of adrenergic input, is markedly diminished when PDE concentration is increased. This reduction in both overshoot amplitude and dynamic range of cAMP concentration takes place over a narrow range of total PDE concentrations (fig. 2.4D).

2.3.4. Phase Plane Analysis of Early Heart Failure and β-blockers. The relationships between various parameters and the phase plane can be used to investigate changes to cellular signaling akin to those that occur early in heart failure, which is associated with both chronic elevation of resting catecholamines and enhanced activity of GRK2. While β-blockers competitively inhibit β_1-ARs, GRK2 has recently been proposed as an additional therapeutic target in heart failure [**13**]. In fig. 2.5, we demonstrate how cellular conditions associated with β_1AR inhibition and GRK2 downregulation impact the adrenergic signaling system.

In fig. 2.5, we examine the separate and joint effects of heart failure described above in fig. 2.5. In all panels, blue curves represent β nullclines and red curves are c nullclines. Solid lines represent the 0 or "low" NE case (NE$-$) while dashed lines indicate the "high" NE (NE+) cases. Green curves represent trajectories of transition from the NE- steady state to the NE+ steady state, indicative of the cAMP response when NE is applied suddenly.

First, we assess the consequence of changes to baseline NE levels in early HF by changing the "low concentration" of ligand to 10 nM NE rather than 0, and considering the difference between a relatively high dose of 10 nM NE in a healthy condition with an increased high

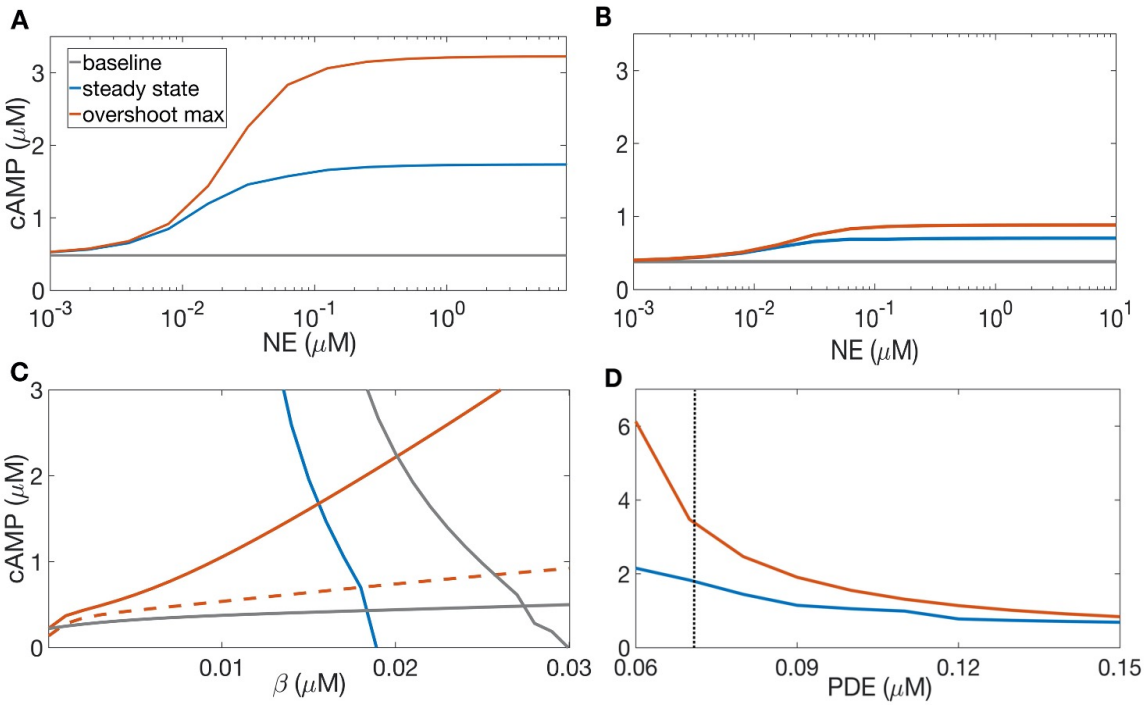

FIGURE 2.4. Effects of phosphodiesterase bulk concentration on cAMP overshoot. A: cAMP steady state (blue) and maximum (red), compared to the NE- steady state (gray), with total PDE concentration 0.072 μM as in [**59**] and [**60**]. As NE increases through several orders of magnitude, overshoot amplitude increases most sharply between 10 and 100 nM NE. B: cAMP steady state and maximal concentration, as in A, with bulk PDE concentration doubled to 0.144 μM. The steady state and maximal concentrations of cAMP are both reduced. C: c and β nullclines with 1μM NE, and total PDE concentrations 0.072 μM (solid red curve) and 0.144 μM (dashed red curve). The gray curves denote the NE- nullclines, and the blue curve depicts the NE+ β nullcline, which is unaltered by increased PDE. Increased concentration of PDE reduces the slope of the cAMP nullcline, changing the steady state concentrations of both c and β and the amplitude of the cAMP overshoot. D: cAMP steady state (blue) and maximum (red) for 1μM NE, with varying concentrations of total phosphodiesterase (sum of PDE3 and PDE4). As PDE concentration increases over a narrow range of values, the amplitude of cAMP overshoot decreases.

dose of 100 nM in heart failure (compare fig. 2.5A and B). Higher β_1-AR activity increases the slope of the cAMP nullcline, which increases the amplitude of the transient "overshoot" in cAMP concentration.

In fig. 2.5C we plot the nullclines for 10 and 100 nM NE, as in B, and additionally increase k_{GRK2} by a factor of 2, corresponding to up-regulation of GRK2. The up-regulation of GRK2 shifts the NE+ β-nullcline (dashed blue curve) to the left, reducing the dynamic range of cAMP concentration. The phase plane in each of these cases depicts a markedly larger transient increase in cAMP production than is observed in the "healthy" case (contrast fig. 2.5 B and C with A) due to the steeper cAMP nullcline, due to the elevated levels of NE both at rest and in heightened SNS activity. Meanwhile the high-NE β nullcline shifts to the left due to the increased GRK2 activity (fig. 2.5B compared with C), reducing the difference between the NE- and NE+ steady state cAMP concentrations. These changes act to increase the overshoot amplitude and decrease the dynamic range. That is, they increase the high cAMP concentrations but reduce the overall responsiveness of the cell to adrenergic input.

In Fig. 2.5D-F, we consider the pharmacological effects of β-blockade and downregulation of GRK2 by varying the available β_1-AR concentration β_{tot} and the GRK2 desensitization rate constant k_{GRK2}. Panel D shows the phase plane for 10 and 100 nM NE with total β_1-AR concentration reduced by half and other parameters at default values. Reducing total β_1-AR concentration mimics inhibition of β_1-ARs. Comparison between panels B and D shows the role of β_1-AR availability alone in determining cellular cAMP dynamics. Comparison between C and D considers the joint effect of β_1-AR inhibition and GRK2 inhibition in reducing β_1-AR availability and reversing the up-regulation of GRK2. Panel E displays the phase plane with 10 and 100 nM NE, with β_1-AR concentration halved and k_{GRK2} doubled. Comparison between C and E can be thought of as the scenario in which GRK2 activity increases in early heart failure, and β-blockers do not reduce this upregulation. Finally, in fig. 2.5F we show the phase plane with 10 and 100 nM NE with both β_1-AR concentration and k_{GRK2} halved. Comparison between C and F represents the case where β-blockers reduce β_1-AR availability and inhibit GRK2, compensating for k_{GRK2} upregulation in early heart failure. In contrast to the "heart failure" conditions, the decrease in available β_1-AR

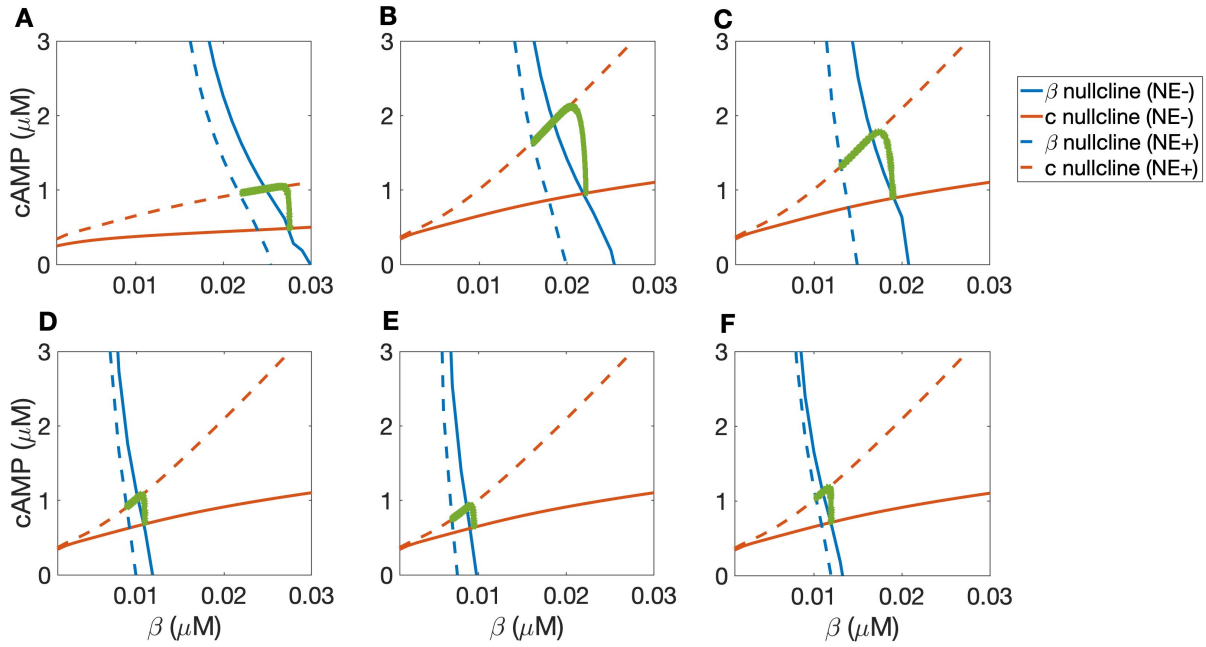

FIGURE 2.5. Putative effects of β-blocker treatment on markers of early heart failure. In all panels, blue curves represent β nullclines and red curves are c nullclines. Solid lines represent 0 NE (NE$-$) while dashed lines indicate the NE+ cases with varying concentrations of NE. Green curves are trajectories from simulations with initial condition at the NE- steady state transitioning to the NE+ steady state. A: phase plane with 0 and 10 nM NE and default parameters, corresponding to a healthy system. B: phase plane with cAMP and β nullclines for 10 and 100 nM NE, corresponding to elevated catecholamine levels at rest as in early heart failure. C: nullclines for 10 and 100 nM NE, as in early heart failure; additionally, k_{GRK2} is increased by a factor of 2, corresponding to up-regulation of GRK2. D: phase plane for 10 and 100 nM NE with total β_1-AR concentration reduced by half and other parameters at default values. E: phase plane with 10 and 100 nM NE, with β_1-AR concentration halved and k_{GRK2} doubled. F: phase plane with 10 and 100 nM NE with both β_1-AR concentration and k_{GRK2} halved.

concentration shifts both NE$-$ and NE+ β-nullclines to the left (fig. 2.5, compare B and D), while the inhibition of GRK2 shifts the NE+ β-nullcline to the right, closer to the NE- β nullcline (fig. 2.5, D-F). These changes jointly counteract the two simulated effects of early heart failure, reducing the amplitude of cAMP overshoot while partially restoring the dynamic range of cAMP concentration.

The important implication of the findings in fig. 2.5 is that the two pathways of β-block and GRK2 downregulation counteract each other to move the NE$-$ β-nullcline to the left

and the NE+ β nullcline to the right, closer to the NE− β-nullcline, thereby controlling the amplitude of the overshoot while maintaining a portion of the dynamic range.

2.3.5. Quantifying Overshoot and Dynamic Range in HF and treatment with β-blockers. The phase plane predicts that the two proposed mechanisms of pharmaceutical treatment, inhibition of β_1-ARs and downregulation of GRK2, act synergistically to reduce the overshoot amplitude of cAMP while maintaining cellular responsiveness to changes in adrenergic agonist concentration. In fig. 2.6, we quantify these effects using predictions generated by nullcline analysis.

Figure 2.6A compares the total accessible dynamic range in four conditions. We simulate the elevated catecholamine levels in early heart failure by raising the "low dose" (NE-) of NE from 0 to 10 μM and the "high dose" (NE+) from 10 to 100 μM in the "heart failure "model. Upregulation of GRK2 is modeled by doubling the rate constant k_{GRK2} associated with GRK2 phosphorylation of the β_1AR. Together, elevated NE and reduced k_{GRK2} act to reduce dynamic range in the "heart failure" case compared to the "healthy" system. We simulate the action of selective β-blockers by reducing the total number of β_1ARs by half, which further reduces the dynamic range. We simulate the additional effect of downregulation of GRK2 concurrent with β_1-AR inhibition by reducing k_{GRK2} to its baseline level, which recovers a portion of the dynamic range.

Fig. 2.6B compares the transient maximal cAMP concentration across parameter regimes for fixed values of dynamic range. Specifically, fig. 2.6B shows the maximal cAMP concentration attained in each scenario during overshoot for the concentration of NE required to achieve a difference of 0.26μM cAMP between NE- and NE+ steady states, corresponding to the dynamic range seen in the concomitant drug treatment condition (β-block + $\downarrow$ GRK2). Respective NE concentrations were 6.5 nM in the "healthy" case, 27 nM in the "HF" case, and 1μM in the "β-block + $\downarrow$ GRK2" case. The early heart failure model attains a higher "overshoot" cAMP concentration (1.4μM) than does the healthy model (0.82μM), due to

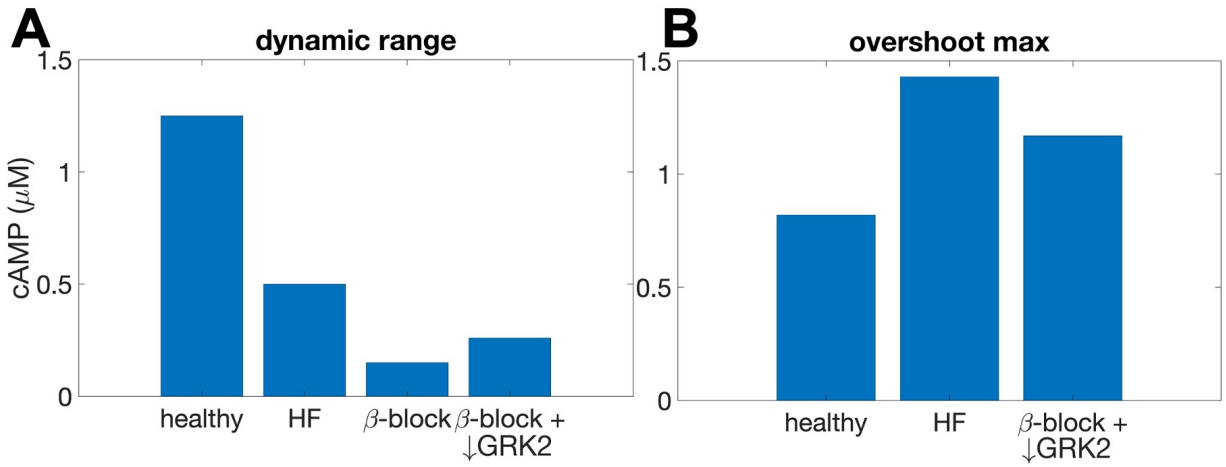

FIGURE 2.6. Effects of early heart failure and β_1-AR inhibition on cellular cAMP baseline, maximum concentration attained during overshoot, and dynamic range as predicted by nullcline analysis. A: dynamic range in four conditions: healthy (baseline 0μM NE and "high dose" 10 μM NE; early heart failure (elevated baseline NE [10μM] and elevated "high dose" NE [100μM]; β-block (as in HF, and with total concentration of β-ARs reduced by 50%); and β-block with concurrent GRK2 downregulation (as in β-block, and with k_{GRK2} reduced by 50%). B: maximal cAMP concentration attained during overshoot for the amount of NE required to achieve a dynamic range of 0.26μM cAMP, compared across the "healthy", "HF", and "β-block + $\downarrow GRK2$" scenarios.

the elevated baseline levels of NE and consequently further elevated "high dose" NE concentration. With NE levels corresponding to the elevated baseline used to simulate early heart failure, the joint treatment of β-blockers with GRK2 downregulation reduces the overshoot amplitude (1.18μM cAMP) for a fixed dynamic range of 0.26 μM cAMP. These results suggest that GRK2 downregulation could act synergistically with β_1-AR inhibition to maintain the cellular responsiveness to adrenergic activity while reducing the transiently high levels of cAMP.

2.4. Discussion

The β-adrenergic signaling pathway is a complex biochemical cascade that is triggered by the binding of norepinephrine to β-adrenergic receptor and leads to the modulation of intracellular cAMP and PKA concentration, which in turn precipitate a wide variety

of downstream effects that alter cellular electrochemical behavior. The Soltis-Saucerman model [**59**, **60**] is a widely-used mathematical model that provides a detailed description of this signaling pathway, using seven dynamic variables and several auxiliary variables. By eliminating non-essential variables and using quasi-steady state approximations, we reduce the β_1-adrenergic signaling component of the Soltis-Saucerman model to a system of two ordinary differential equations for cellular cAMP concentration and non-desensitized β_1-AR concentration. The success of this reduced model in replicating predictions of the full model reveals the rate-determining steps for the kinetics of the portion of the β_1-adrenergic signaling cascade up to PKA activation. Namely, production of cAMP by adenylyl cyclase and degradation of cAMP by phosphodiesterase are the primary determinants for the kinetics of the sympathetic-induced rise in cellular cAMP concentration, on a time scale of $\sim$1 minute. The desensitization of β_1-ARs by PKA and by GRK2, and subsequent resensitization of the receptors, control the time scale of the slow decline of cAMP concentration to steady state during prolonged norepinephrine exposure, which occurs over $\sim$10 minutes. Thus, the reduced Soltis-Saucerman model suggests that cAMP production and degradation and β_1-AR desensitization and resensitization dictate the temporal kinetics of cAMP, and the associated changes in heart rate and contractility, in response to changes in SNS activity as in physical and emotional arousal.

The analysis presented here explicitly quantifies the relationship between synaptic adrenergic agonist concentration and magnitude of cellular response. Moreover, the phase plane makes apparent that the size of this overshoot is modulated by the steepness of the cAMP nullcline in (β, c) space, the position of the β-AR nullcline, and the difference in time scales between relatively fast cAMP dynamics and relatively slow desensitization and resensitization of β_1-ARs.

Given the time scale of tens of seconds between the onset of receptor activation and increased cAMP concentration, the cAMP overshoot requires a sufficiently abrupt increase in adrenergic agonist. As demonstrated in our results, a sudden large increase in agonist

concentration leads to transiently high cAMP concentration, i.e., overshoot. However, in the hypothetical scenario in which norepinephrine were to be applied at a more gradual rate commensurate with the stimulated production of cAMP by adenylyl cyclase, the quasi-steady-state cAMP concentration would also shift gradually, preventing the initial rise in cAMP concentration seen in overshoot. Instead, cAMP would increase monotonically to the NE+ steady state. Thus, we expect slow increases in SNS activity to cause markedly lower transient cAMP amplitude as compared with rapid increases in SNS activity, i.e. sympathetic surges.

Our analysis generates predictions regarding how cellular cAMP overshoot will respond to various changes to cellular conditions. Changes to bulk PDE concentration, for instance, alter the amplitude of cAMP overshoot, but also greatly reduce the range of attainable steady-state cAMP concentrations, impairing the heart's ability to respond to fluctuations in sympathetic tone. Thus, PDE in cardiac myocytes is likely not an effective pharmacological target in counteracting the cellular adaptations present in heart failure. It has recently been shown, however, that PDE2A in stellate ganglion neurons may be an effective target for reducing sympathetic hyperactivity [**40**].

Adrenergic surges are known to be especially arrhythmogenic in individuals with heart failure and other pathologies. The success of the reduced model at replicating the predictions made by the full Soltis-Saucerman model demonstrates that the concentration of two variables, cAMP and non-desensitized β_1AR, capture the overall dynamics of sympathetic signaling. Therefore, the effects of heart failure, and other diseases of the sympathetic nervous system, on components of the β_1-adrenergic signaling pathway can be reduced to how disease alters the factors that directly impact cAMP production/degradation and beta-AR (de)phosphorylation. The key factors influencing cAMP production are AC activity and PDE3,4 activity, while those that directly impact β_1AR phosphorylation are βARK and PKA_I activity; thus, we expect these factors to be effective targets for pharmaceutical therapy in diseases affecting the cardiac nervous system. It should be noted that we do not

address chronic heart failure, which results in a wide array of structural and biochemical changes throughout the heart, including a reduction in β_1AR density as well as changes to sympathetic cardiac innervation [**57**].

Our work demonstrates that the dynamics of only the cellular concentrations of cAMP and non-desensitized β_1AR can capture how two of the effects of early heart failure, alteration of the resting levels of adrenergic agonists and upregulation of GRK2, jointly act to change the maximal transient cAMP concentration and the longer-term overall responsiveness of the cell to sympathetic stimulation. Among the many structural and physiological changes in heart failure, up-regulation of GRK2 is frequently observed and suspected to play a role in cardiac pathology, whether due to its effects on adrenergic signaling or other interactions [**43**]. Increased levels of baseline norepinephrine increase the slope of the cAMP nullcline, which heightens the transient cAMP amplitude during "overshoot". Meanwhile, the upregulation of GRK2 activity shifts the β nullcline to favor lower concentrations of β, reducing the cAMP concentration at the stimulated steady state and therefore diminishing the cell's responsiveness to NE concentration changes. These results, while omitting the complexity of the compensatory mechanisms present in various stages of heart failure, provide a qualitative proof of concept demonstrating that the effects of early stages of heart failure on the adrenergic signaling pathway can be captured by the processes controlling the dynamics of cAMP and non-desensitized β_1 adrenergic receptors.

Pharmacological inhibitors of β-adrenergic receptors, known as β-blockers, are generally considered protective in heart failure, but often also come with cardiac and other medical risk [**6**, **7**, **17**, **37**]. Modeling work has considered the effects of β-blockers on both the "maintenance" and the "inhibition" of cellular responsiveness to adrenergic stimulation [**2**], suggesting that these two processes need not be viewed as mutually contradictory. Separately, recent work has identified a wide range of targets of GRK2 [**53**] and demonstrated that reduction of GRK2 activity, either genetic or pharmacologic, may improve overall cardiovascular function, particularly in heart failure [**42**, **62**]. Some experiments suggest that

diminished GRK2 activity may act synergistically with β-blocker therapeutic drugs to prevent mortality risk in individuals with heart failure [**13**, **42**, **47**, **62**]. Our results suggest a mechanistic justification for this hypothesis: lowering GRK2 activity alongside β_1-AR inhibition reduces the amplitude of cAMP overshoot, and partially rescues the dynamic range of cAMP concentration compared with β-blockers alone in heart failure conditions. Taken together, these "maintenance" and "inhibition" processes work to counteract the simulated effects of early heart failure. To evaluate these predictions, our simulations should be compared with the efficacy of various β-blockers and GRK2 inhibitors, administered both separately and concurrently, for reducing mortality and heart failure symptoms particularly in early HF. While the predictions made by this model are qualitative rather than precise, the two-variable model provides a simple framework by which to assess and compare how various pharmaceutical treatments may affect adrenergic signaling.

It has been posited that an imbalance between the magnitude and timing of sympathetic and parasympathetic nervous system activity is a primary driver for arrhythmias in heart disease. Prior modeling work [**30**, **31**] has explained a cellular cAMP "overshoot" phenomenon with similar temporal dynamics to that shown here as a consequence of this time-scale mismatch along with subcellular compartmentation of separate pools of cAMP and signaling components. By examining the isolated G_s-mediated pathway, we have demonstrated that overshoot can occur and can be modified independent of parasympathetic input. Given the prior evidence that mismatch between sympathetic and parasympathetic activity enhances cAMP transient elevation and heightens arrhythmogenic risk, it would be beneficial to further explore the subcellular signaling pathways involved in these two systems, and the interaction between the two. For instance, experiments with cells containing the β_1-adrenergic signaling machinery, but lacking muscarinic receptors or inhibitory G-protein, could differentiate between β_1-AR desensitization and parasympathetic nervous system activity as mechanisms for cellular cAMP overshoot during sympathetic stimulation.

Variable Number	Variable Name	Description
1	L	β-AR agonist
2	R	β-AR
3	G	available G-protein
4	β	unphosphorylated β_1-AR
5	β_{BARK}	β-AR phosphorylated (inhibited) by β-ARK
6	β_{PKA}	β-AR phosphorylated by PKA
7	$G_{\alpha,\,GTP}$	Total G_α^{GTP}
8	$G_{\alpha,\,GDP}$	G_α^{GDP}
9	$G_{\beta\gamma}$	$G_{\beta\gamma}$
10	$G^f_{\alpha,\,GTP}$	Free G_α^{GTP}
11	Fsk	Forskolin
12	AC	adenylyl cyclase
15	c	total cAMP
16	c_f	free cAMP
17	PKA_{c_1}	Catalytic subunit of PKA_I
18	PKA_{c_2}	Catalytic subunit of PKA_{II}

TABLE 2.1. Variable names and definitions for the β_1-adrenergic signaling subsystem of the Soltis-Saucerman model.

2.5. Appendix

2.5.1. Soltis-Saucerman model. The adrenergic signaling subsystem of the original model [**59**, **60**, **65**]) has 16 variables (Table A.1):

The variables obey a system of ordinary differential equations (ODEs) and differential algebraic equations (DAEs), as follows. The algebraic equations reflect conservation laws and steady-state concentrations for reactions assumed to reach steady state instantaneously.

Algebraic Equations:

Ligand-Receptor Equations

$$L = L_{tot} - \frac{L \cdot R}{p_4} - \frac{L \cdot R \cdot G}{p_4 \cdot p_5}$$

$$R = \beta - \frac{L \cdot R}{p_4} - \frac{L \cdot R \cdot G}{p_4 \cdot p_5} - \frac{R \cdot G}{p_6}$$

$$G = p_3 - \frac{L \cdot R \cdot G}{p_4 \cdot p_5} - \frac{R \cdot G}{p_6}$$

G-protein-AC activation equations

$$G^f_{\alpha,\,GTP} = G_{\alpha,\,GTP} - \frac{G^f_{\alpha,\,GTP} \cdot AC}{p_{26}}$$

$$AC = p_{14} - \frac{G^f_{\alpha,\,GTP} \cdot AC}{p_{26}}$$

cAMP-PKA equations

$$\begin{aligned}
c_f = c &- \left[\frac{p_{36}}{c_f} \cdot \frac{PKA_{c_1}}{p_{38}} \cdot PKA_{c_1} \cdot \left(1 + \frac{p_{35}}{p_{39} + PKA_{c_1} + PKA_{c_2}}\right)\right] \\
&2\frac{PKA_{c_1}}{p_{38}} \cdot PKA_{c_1} \cdot \left(1 + \frac{p_{35}}{p_{39} + PKA_{c_1} + PKA_{c_2}}\right) \\
&- 2PKA_{c_1} \cdot \left(1 + \frac{p_{35}}{p_{39} + PKA_{c_1} + PKA_{c_2}}\right) \\
&- \left[\frac{p_{36}}{c_f} \cdot \frac{PKA_{c_2}}{p_{38}} \cdot PKA_{c_2} \cdot \left(1 + \frac{p_{35}}{p_{39} + PKA_{c_1} + PKA_{c_2}}\right)\right] \\
&- 2\frac{PKA_{c_2}}{p_{38}} \cdot PKA_{c_2} \cdot \left(1 + \frac{p_{35}}{p_{39} + PKA_{c_1} + PKA_{c_2}}\right) \\
&- 2PKA_{c_2} \cdot \left(1 + \frac{p_{35}}{p_{39} + PKA_{c_1} + PKA_{c_2}}\right)
\end{aligned}$$

$$0 = 2p_{33}c_f^2 - PKA_{c_1}\left(1 + \frac{p_{35}}{p_{39} + PKA_{c_1} + PKA_{c_2}}\right)\left[\left(\frac{p_{36} \cdot p_{37}}{p_{38}} + \frac{p_{36} \cdot c_f}{p_{38}} + \frac{c_f^2}{p_{38}}\right) PKA_{c_1} + c_f^2\right]$$

$$0 = 2p_{34}c_f^2 - PKA_{c_2}\left(1 + \frac{p_{35}}{p_{39} + PKA_{c_1} + PKA_{c_2}}\right)\left[\left(\frac{p_{36} \cdot p_{37}}{p_{38}} + \frac{p_{36} \cdot c_f}{p_{38}} + \frac{c_f^2}{p_{38}}\right) PKA_{c_2} + c_f^2\right]$$

Differential Equations:

$\beta_1 - AR$ **dynamics**

$$\begin{aligned}
\frac{d\beta}{dt} &= p_8\beta_{BARK} - \frac{p_7}{p_4}L \cdot R - \frac{p_7}{p_4 \cdot p_5}L \cdot R \cdot G + p_{10}\beta_{PKA} - p_9\beta PKA_{c_1} \\
\frac{d\beta_{BARK}}{dt} &= -p_8\beta_{BARK} + \frac{p_7}{p_4}L \cdot R + \frac{p_7}{p_4 \cdot p_5}L \cdot R \cdot G \\
\frac{d\beta_{PKA}}{dt} &= -p_{10}\beta_{PKA} + p_9\beta PKA_{c_1}
\end{aligned}$$

G-protein dynamics

$$\frac{dG_{\alpha,\,GTP}}{dt} = \frac{p_{11}}{p_6} R \cdot G + \frac{p_{11}}{p_4 \cdot p_5} L \cdot R \cdot G - p_{12} G_{\alpha,\,GTP}$$
$$\frac{dG_{\alpha,\,GDP}}{dt} = p_{12} G_{\alpha,\,GTP} - p_{13} G_{\alpha,\,GDP} G_{\beta\gamma}$$
$$\frac{dG_{\beta\gamma}}{dt} = \frac{p_{11}}{p_6} R \cdot G + \frac{p_{11}}{p_4 \cdot p_5} L \cdot R \cdot G - p_{13} G_{\alpha,\,GDP} G_{\beta\gamma}$$

cAMP dynamics

$$\frac{dc}{dt} = \left(\frac{p_{15} p_{20}}{p_{23} + p_{15}}\right) AC + \left(\frac{p_{15} p_{21}}{p_{24} + p_{15}}\right) G^f_{\alpha,\,GTP} AC$$
$$- \frac{p_{16} p_{28} c_f}{p_{29} + c_f} - \frac{p_{17} p_{30} c_f}{p_{31} + c_f}$$

2.5.2. Reduction to two-variable model. STEP 1 (G-protein dynamics): Note that the he variables $G_{\alpha,GDP}$ and $G_{\beta\gamma}$ do not appear in any equations other than the differential equations governing their own dynamics. Therefore, the equations for $G_{\alpha,GDP}$ and $G_{\beta\gamma}$ can be removed from the system, leaving only the single differential equation for $G_{\alpha,GTP}$ in the G-protein subsystem.

STEP 2 (β_1-AR dynamics): Note that the three states of the β_1-AR (β, β_{BARK}, and β_{PKA}) obey the conservation law

$$\beta + \beta_{\beta ARK} + \beta_{PKA} = \beta_{tot}$$

where the constant β_{tot} is the total concentration of β_1-ARs. Furthermore, because $p_8 = p_{10}$ in the Soltis-Saucerman model, the variables β_{BARK} and β_{PKA} representing phosphorylated β_1-AR states only appear as a sum in the differential equation for β. Therefore, β_{BARK} and β_{PKA} can be removed by replacing their sum with $\beta_{tot} - \beta$, which yields the single differential equation for the dynamics of β.

Thus, these observations yield a system of three differential equations for cAMP dynamics:

$$\begin{aligned}
\frac{d\beta}{dt} &= p_{10}(\beta_{tot} - \beta) - \frac{p_7}{p_4} L \cdot R - \frac{p_7}{p_4 \cdot p_5} L \cdot R \cdot G - p_9 \beta PKA_{c_1} \\
\frac{dG_{\alpha,\,GTP}}{dt} &= \frac{p_{11}}{p_6} R \cdot G + \frac{p_{11}}{p_4 \cdot p_5} L \cdot R \cdot G - p_{12} G_{\alpha,\,GTP} \\
\frac{dc}{dt} &= \left(\frac{p_{15} p_{20}}{p_{23} + p_{15}} \right) AC(G_{\alpha,GTP}) + \left(\frac{p_{15} p_{21}}{p_{24} + p_{15}} \right) G^f_{\alpha,\,GTP} \cdot AC(G_{\alpha,GTP}) \\
&\quad - \frac{p_{16} p_{28} c_f}{p_{29} + c_f} - \frac{p_{17} p_{30} c_f}{p_{31} + c_f}
\end{aligned}$$

We define $F_1(\beta; L_{tot})$ as the desensitization rate of β_1-AR phosphorylated by GRK2:

$$F_1(\beta; L_{tot}) = k_{GRK2} \left(\frac{1}{p_4} L \cdot R + \frac{1}{p_4 \cdot p_5} L \cdot R \cdot G \right)$$

and $F_2(\beta; L_{tot})$ as the rate of G-protein activation:

$$F_2(\beta; L_{tot}) = \frac{p_{11}}{p_6} R \cdot G + \frac{p_{11}}{p_4 \cdot p_5} L \cdot R \cdot G$$

where L, R, and G are obtained by solving the LRG equations. (Note that k_{GRK2} is named as $k_{\beta ARKp}$ in [**60**].) Both $AC(G_{\alpha,GTP})$ and $G^f_{\alpha,GTP}$ can be obtained explicitly by solving the G-protein-AC algebraic equations:

$$\begin{aligned}
AC &= \frac{-G_{\alpha,\,GTP} + p_{14} - p_{26} + \sqrt{(p_{14} + p_{26} - G_{\alpha,\,GTP})^2 + 4 p_{26} G_{\alpha,\,GTP}}}{2} \\
G^f_{\alpha,GTP} &= \frac{G_{\alpha,\,GTP} - p_{14} + p_{26} + \sqrt{(p_{14} + p_{26} - G_{\alpha,\,GTP})^2 + 4 p_{26} G_{\alpha,\,GTP}}}{2}
\end{aligned}$$

and $PKA_{c_1}(c)$ and $c_f(c)$ are obtained by solving the cAMP-PKA algebraic equations.

This system of three differential equations can be further reduced to a system of two differential equations. Note that $G_{\alpha,GTP}$ changes much more rapidly than do β and c (see fig. 2.1). Therefore, we can exploit this separation of time scales and eliminate $G_{\alpha,GTP}$ by equilibrating to its quasi-steady value:

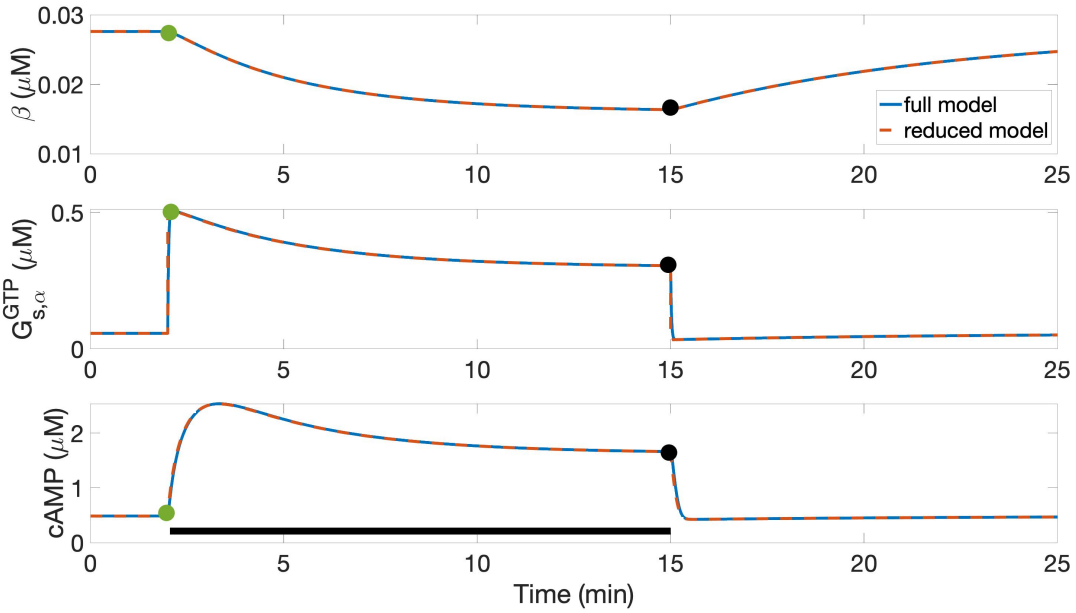

FIGURE 2.1. When the full model is initialized from a steady state with 0 NE, and 1μM NE is abruptly added, $G_{s,\alpha}^{GTP}$ adapts to its quasi-steady state value much more rapidly than do cAMP and $\beta_1 AR$ concentrations. This justifies the simplification that $G_{s,\alpha}^{GTP}$ reaches quasi-steady state instantaneously, reducing the system of three variables to a two-dimensional system.

$$G_{\alpha,GTP} = \frac{p_{11}}{p_{12}}\left(\frac{RG}{p_6} + \frac{LRG}{p_4 p_5}\right) = \frac{F_2(\beta; L_{tot})}{p_{12}}$$

Thus, we obtain our reduced model (2.1):

$$\begin{aligned}
\frac{d\beta}{dt} &= p_{10}(\beta_{tot} - \beta) - F_1(\beta; L_{tot}) - p_9 \beta PKA_{c_1} \\
\frac{dc}{dt} &= \left(\frac{p_{15}p_{20}}{p_{23} + p_{15}}\right) AC_b(\beta; L_{tot}) + \left(\frac{p_{15}p_{21}}{p_{24} + p_{15}}\right) AC_s(\beta; L_{tot}) \\
&\quad - \frac{p_{16}p_{28}c_f}{p_{29} + c_f} - \frac{p_{17}p_{30}c_f}{p_{31} + c_f}
\end{aligned}$$

where $AC_b = AC$, so that $\left(\frac{p_{15}p_{20}}{p_{23}+p_{15}}\right) AC_b(\beta; L_{tot})$ represents the rate of cAMP produced by adenylyl cyclase at a basal rate, not activated by $G_{\alpha,GTP}$ and $AC_s = AC \cdot G_{\alpha,GTP}^f$, so that $\left(\frac{p_{15}p_{21}}{p_{24}+p_{15}}\right) AC_s(\beta; L_{tot})$ represents the rate of cAMP produced by adenylyl cyclase stimulated by $G_{\alpha,GTP}$.

2.5.3. Validation of Reduced Model. We validated the reduced model by comparing its predictions to those made by the full model across a range of NE concentrations in each of the scenarios described in fig. 2.5. In fig. 2.2A, we compare the cAMP steady states with 0 $\$mu$M NE (NE- ss) and a range of nonzero NE concentrations (NE+ss), and overshoot max (OS max) attained from an initial condition at the NE- steady state, in the healthy condition ($\beta_{tot} = 0.028\mu$M, $k_{GRK2} = 1.1e{-}3\ \text{sec}^{-1}$). The reduced model replicates the predictions made by the full model for the steady states. As described in fig. 2.3, the overshoot maximum is estimated for the reduced model using the point on the cAMP nullcline corresponding to the β value at the NE- steady state. In the full model, the overshoot maximum is computed using the maximum value of cAMP attained during the simulation. This results in a consistent overestimate of the overshoot maximum for the reduced model. In fig. 2.2B, we compute NE- cAMP steady states using 0.01 μM NE, and increase k_{GRK2} to $2.2e{-}3\ \text{sec}^{-1}$, to simulate early heart failure. In fig. 2.2C we consider the effect of β-block by reducing β_{tot} to 0.014 μM, with baseline NE and k_{GRK2} corresponding to the "HF" model. Finally, in fig. 2.2D we consider the joint effect of β-block with k_{GRK2} inhibition by reducing k_{GRK2} to its standard value of $1.1e-3\ \text{sec}^{-1}$, while keeping all other parameters fixed from fig. 2.2C. In all four situations, the reduced model closely captures the steady states predicted by the full model, and the overshoot calculation using the nullclines slightly overestimates the maximum cAMP concentration.

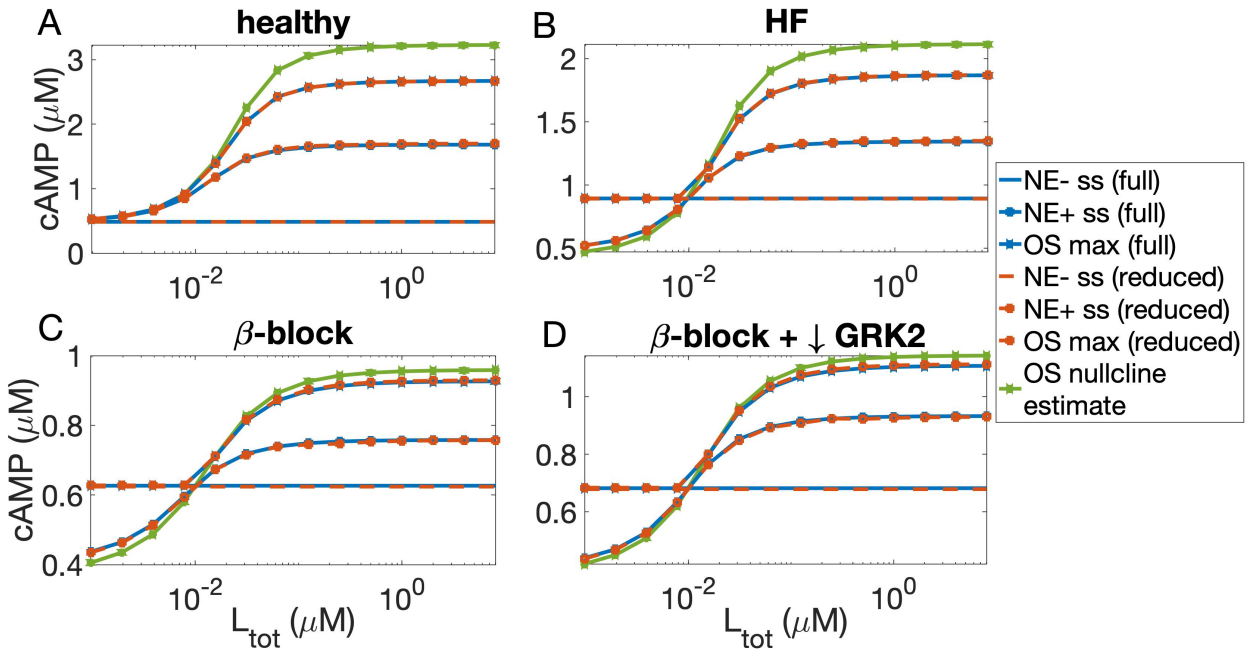

FIGURE 2.2. Comparison between the predictions of the full and reduced model across a range of L_{tot} values in each scenario described in fig. 2.5. A: cAMP steady states with 0 μM NE (NE- ss) and a nonzero NE concentration, and overshoot max (OS max) attained from an initial condition at the NE- ss, in the healthy condition ($\beta_{tot} = 0.028\mu$M, $k_{GRK2} = 1.1e-3$ sec^{-1}). B: as in A, but with NE- cAMP steady states computed using 0.01 μM NE and $k_{GRK2} = 2.2e-3$ sec^{-1}. C: as in B, with $\beta_{tot} = 0.014\mu$M. D: as in C, with $k_{GRK2} = 1.1e-3$. In all panels, the overshoot max in the full and reduced model are computed from simulations (red and blue curves) and compared with the estimate of overshoot max (green) computed using the value of the cAMP nullcline corresponding to the β concentration at the NE- steady state. The nullclines consistently overestimate the overshoot.

2.6. Acknowledgments

This work is supported by the National Institutes of Health (NIH) Stimulating Peripheral Activity to Relieve Conditions grant OT2OD026580 (CC and TL).

CHAPTER 3

Gap Junctional Voltage Dependence and Weakly Coupled Oscillators in SAN Pacemaker Synchrony

3.1. Introduction

As discussed in the Introduction, the SAN must generate tissue-scale electrical oscillations robustly over a range of frequencies, depending on physical needs of the body and input from the nervous system, in order to consistently pace the cardiac muscle tissue. Given that the success of the SAN in pacing the myocardium relies on current transfer through electrical coupling between individual cells, it is important to understand how the mechanisms of such electrical coupling facilitate cardiac pacing.

Electrical conduction throughout the heart depends on cell-to-cell coupling primarily accomplished by gap junctions. Gap junctions are plaques formed at the interface between adjacent cell membranes containing multi-protein channels through which ions can travel from one cell to an adjacent cell. By allowing current conduction between cells, gap junctions are crucial in coordinating electrical activity throughout the heart, and therefore they are vital to the overall pacemaking function in the heart.

Gap junctions are composed of subunits of proteins called connexins, of which several isoforms are expressed differentially across regions of the heart. The SAN and AVN predominantly contain Cx45 gap junctions, whereas Cx43 gap junctions are much more common throughout the atria and ventricles ([**15**, **18**]; see Table 1 in [**18**] for approximate abundance levels of Cx40, Cx43, and Cx45 throughout each region of the heart). The differences in expression of gap junction type over space and in pathology raise the question of why Cx45 gap junctions are expressed in the sinoatrial node, rather than the Cx43 gap junctions expressed elsewhere in the heart.

In order to examine how Cx45 gap junctions might be uniquely suited for the SAN, we consider the functional differences between types of gap junctions. One prominent factor distinguishing the function of gap junction types is the dependence of conductance on junctional voltage, i.e., the difference in membrane potential between the two coupled cells. Although many electrophysiological models incorporate gap junctional coupling between cells, it is conventionally assumed that coupling strength is constant; thus, the effects of voltage dependence of gap junctional conductance are not well studied. Voltage-clamp studies show that the conductance across gap junctions is maximized when the membrane potentials of the two adjacent cells are similar; as the difference between membrane potentials (transjunctional voltage, ΔV) increases in absolute value, the conductance across the gap junction decreases (see fig. 3.1 left panel). Conduction through Cx45 gap junctions displays a steeper dependence on junctional voltage than does conduction across Cx43 gap junctions, and a narrower window of junctional voltage in which the conductance is close to its maximal value. Moreover, for any fixed junctional voltage, the conductance does not develop instantaneously but displays time-dependent gating characteristcs and reaches the steady-state conductance over a period of 10-100 milliseconds (fig. 3.1, right panel). This voltage-dependence develops more rapidly in Cx45 than in Cx43 gap junctions (figure 3.1, taken from [**19**]).

Perhaps the most obvious explanation for the predominance of Cx45 gap junctions in the SAN as compared with the atria is that Cx45 gap junctions help to achieve an overall lower level of coupling within the SAN than in the atria. As argued in [**9**], the SAN (and AVN) may need to maintain lower conductivity in order to allow for insulation from the surrounding tissue, which acts as an electrical sink. The single-channel conductance of Cx45 gap junctions is lower than that of Cx43 gap junctions, and there are fewer overall gap junctions in the SAN than in the atria, both of which result in a lower average coupling conductance through the SAN than the surrounding atrium [**18**]. The steeper voltage dependence of conductance in Cx45 gap junctions, as compared with Cx43 gap junctions, further contributes to the reduction in relative overall conductance in the SAN. However, in intrinsically oscillatory

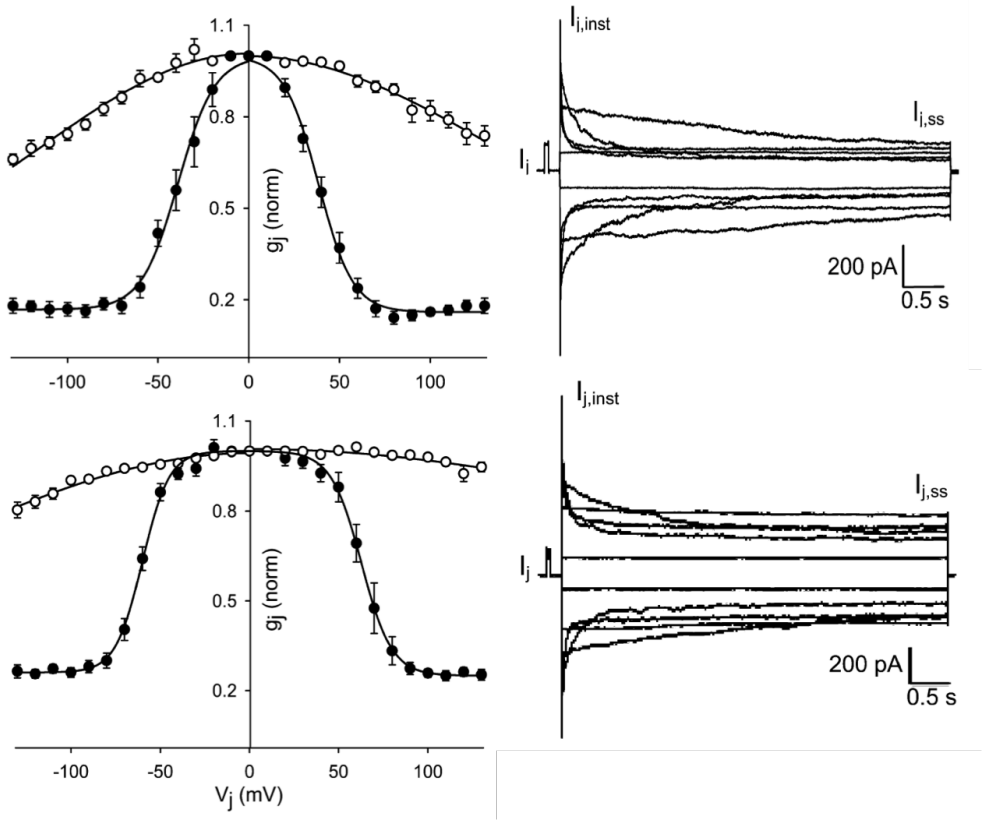

FIGURE 3.1. Voltage dependent gating of gap junctions composed of Cx45 (top left, present in the sinoatrial node) and Cx43 (bottom, present in the atrium). Note that Cx45 gap junctions exhibit steeper voltage dependence, that is, as voltage difference between the two cells increases, conduction across the gap junction decreases. Right panel: time course of voltage dependence in Cx45 (top right) and Cx43 (top right) gap junctions. Reproduced with permission from [**19**].

SAN cells, the voltage-dependence of gating in Cx45 gap junctions may influence the phase-locking properties in non-trivial ways, which would provide a more complex explanation for the expression of Cx45 gap junctions in the SAN.

In the present work, we aim to analyze how the properties of voltage-dependent conductance in gap junctions influence synchrony in paired sinoatrial node cells. The nonlinearity of the intrinsic cellular dynamics makes it difficult to fully understand the effects of voltage-dependent coupling on synchronization of activity, and therefore it is helpful to separate the intrinsic electrical properties of individual SAN cells from the particular form of coupling in pairs of cells. The theory of weakly coupled oscillators provides a convenient and useful

framework for our study, as it reduces the intrinsic electrical activity of each cell to a single periodic variable and isolates this intrinsic activity from the effects of coupling. We apply this framework to understand the robustness of synchrony to heterogeneities in cellular properties and in gap junctional coupling in groups of two or more cells in the sinoatrial node. The theory of weakly coupled oscillators has been widely used to study synchronization in networks of biological oscillators [**64**]. In particular, prior work has applied a reduced phase model [**41**] and the theory of weakly coupled oscillators [**35**] to analyze synchrony and conduction patterns in the SAN; however, this work has not addressed the role of voltage-dependent coupling in influencing pacemaking properties.

Here, we specifically investigate the effects of voltage-dependent gap junction gating in the SAN. We utilize the theory of weakly coupled oscillators to examine how voltage-gated conductance affects the robustness of synchrony in 2- and 3-cell networks of SAN cells. In a pair of two coupled cells, we analyze and interpret the effects of the parameters that define voltage-dependence of gap junction gating on the robustness of 1:1 phase-locking to heterogeneity and noise. We then consider how voltage-dependent conductance may influence a larger network beyond a single pair of cells by studying a three-cell system with both nearest-neighbor coupling and all-to-all coupling. This allows us to examine the effects of one cell on a group of coupled cells, as well as the impact of differentially changing frequencies on the system, which may shed light on the ability of the lead pacing site within the SAN to shift spatially as in experiments [**10**, **46**]. Finally, the voltage dependence of gating appears to develop on a time scale of hundreds of milliseconds (fig. 3.1), comparable to the time-scale of the action potential in SAN cells. This suggests that the slow onset of voltage-dependence may create further complexity in the synchrony of cells coupled by voltage-dependent gap junctions. In order to account for the non-instantaneous onset of voltage dependence, we consider the effects of slow voltage-dependent conductance that changes on the same time scale as the changes to frequency due to coupling.

3.2. Sinoatrial Node Cell Model

The three-variable ionic model for sinoatrial node cell electrophysiology by Guevara [**26**] was developed by exploiting differences in time scales in order to reduce a prior SAN cell model by Irisawa and Noma [**32**]. We consider the Guevara model for its simplicity, and reduce it to a single-variable phase model. The original model includes variables for membrane potential (V), inactivation gate for the slow inward current I_s (f), and potassium channel activation (p):

$$\begin{aligned}
\frac{dV}{dt} &= -d_\infty f(V)\bar{i}_S(V) - p(V)\bar{i}_K(V) - I_l(V) + I_{app} \\
\frac{df}{dt} &= \alpha_f(V)(1-f) - \beta_f(V)f \\
\frac{dp}{dt} &= \alpha_p(V)(1-p) - \beta_p(V)p
\end{aligned}$$

The system exhibits periodic behavior in which V fires repeated action potentials with period $\approx$ 350 ms, while the gating parameters f and p oscillate between 0 and 1 with the same period. We show the oscillatory behavior of the model in fig. 3.2; in state space, the trajectories orbit around a stable limit cycle. See Appendix for parameters and function definitions for the Guevara model. In a pair of cells with membrane potentials V_i and V_j, gap junctional coupling between two cells is modeled as an applied current for each cell in the form $I_C = g_j \cdot (V_j - V_i)$, where g_j is the gap junctional conductance. Thus, the differential equations for the two cells' membrane potentials are:

$$\begin{aligned}
\frac{dV_i}{dt} &= -d_\infty f(V_i)\bar{i}_S(V_i) - p(V_i)\bar{i}_K(V_i) - I_L(V_i) + g_j(V_j - V_i) \\
\frac{dV_j}{dt} &= -d_\infty f(V_j)\bar{i}_S(V_j) - p(V_j)\bar{i}_K(V_j) - I_L(V_j) + g_j(V_i - V_j).
\end{aligned}$$

We use the form of voltage-dependent gap junctional conductance established by Desplantez et al. [**19**]:

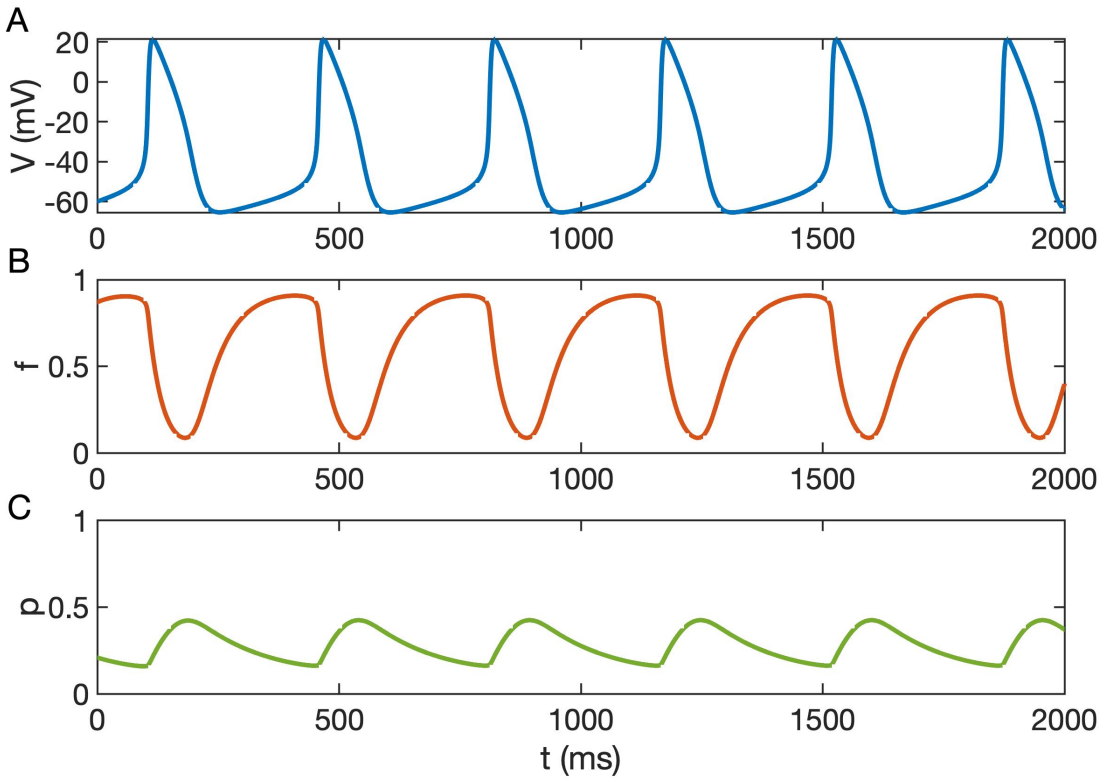

FIGURE 3.2. The Guevara model for a single cell exhibits periodic behavior. A: Membrane potential versus time; the cell fires periodic action potentials with period ≈ 350 ms. B and C: gating variables f and p versus time.

$$g_j = \bar{g} g_{j,ss}(\Delta V) = \bar{g}\left(\frac{1 - g_{j,min}}{1 + \exp[A(|\Delta V| - |V_{j,0}|)]} + g_{j,min}\right)$$

where the transjunctional voltage $\Delta V = V_j - V_i$ is the difference between the two cells' membrane potentials. The voltage dependence of gap junctions depends on three parameters $V_{j,0}$, $g_{j,min}$ and A, which determine the sensitivity and average conductance carried by gap junctions over a range of junctional potentials ΔV (fig. 3.3). Parameter values corresponding to Cx43 and Cx45 gap junctions are approximated from [**19**] and listed in Table 3.1. Notably, the overall voltage-dependence of conductance is steeper in Cx45 gap junctions than in Cx43 gap junctions, as can be observed qualitatively in fig. 3.1.

We normalize the function $g_{j,ss}(\Delta V)$ in each case such that its maximum is 1; that is, there is a maximal conductance of 1 in all cases. In order to investigate questions about

TABLE 3.1. Parameter values defining voltage-dependence of conductance for Cx43 and Cx45 gap junctions. Approximate values from [**19**].

	$g_{j,min}$	$V_{j,0}$	A
Cx43	0.26	61.5	0.11229
Cx45	0.17	39	0.093575

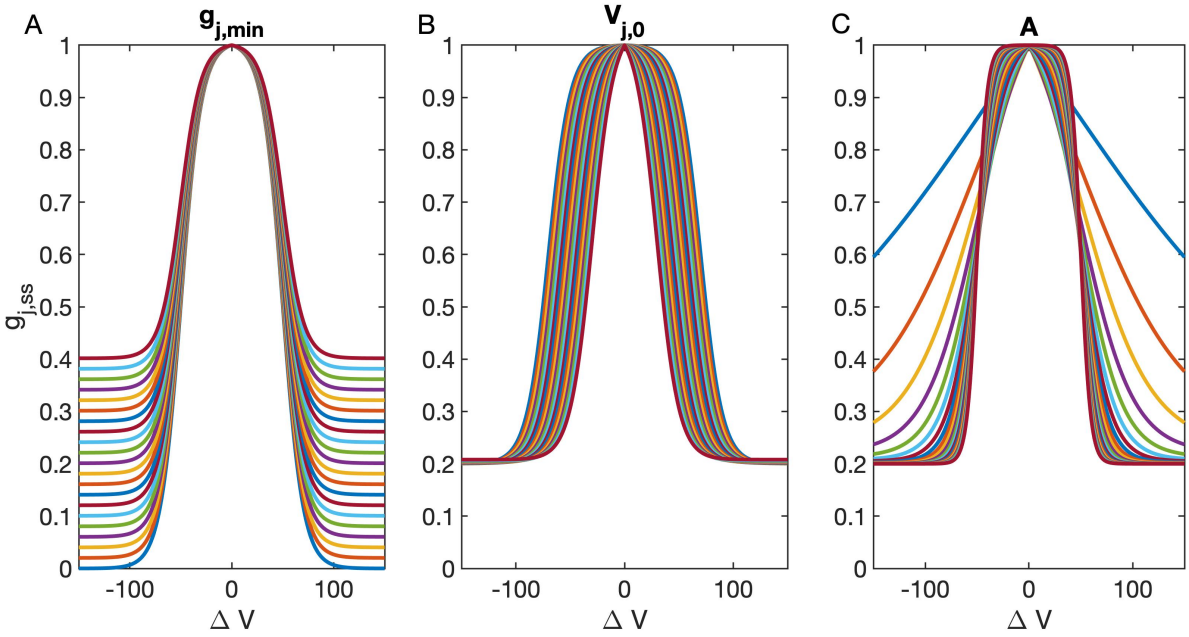

FIGURE 3.3. Gap junctional conductance depends on transmembrane voltage with the parameters $g_{j,min}$, $V_{j,0}$, and A defining the function. Panels A, B, and C respectively show how each parameter modifies the dependence of conductance on voltage. While $V_{j,0}$ primarily determines the width of the high-conductance window for transmembrane voltage, $g_{j,min}$ determine the conductance in the tails where transmembrane voltage is very high or low, and A defines the steepness of transition from the peak to the minimum conductance.

coupling between cells, we incorporate voltage dependence into the voltage-based coupling term in a model of two (or three) adjacent cells.

3.2.1. Time-dependent gating. Note that in the above, it was assumed that gap junctional conductance $g_{j,ss}$ changes instantaneously with transjunctional voltage ΔV. Evidence suggests that the coupling function $I_C = g_j \Delta V$ for the gap junctions in the heart depends not only on the transmembrane potential but also depends explicitly on time (fig. 3.1, and [**19**]). If voltage dependence develops on a time scale comparable to or slower than

the cells' intrinsic action potential or the effects of coupling, then the combined voltage dependence and time dependence of coupling may give rise to more complicated dynamics in the system that cannot be identified by examining voltage dependence alone. Therefore, we extend the coupling term in our model to take into account the possibility that conductance develops over time. We assume that there is a steady-state conductance that depends on transjunctional voltage, i.e., $g_{j,ss}(\Delta V)$ as in the previous section. However, we now assume that the conductance g_j approaches $g_{j,ss}$ in a first-order exponential decay process with time constant $\tau_j \approx 0.01$, such that it can be modeled with the following differential equation:

$$\frac{dg_j}{dt} = \frac{1}{\tau_j}(g_{j,ss} - g_j).$$

With two coupled cells, the model consists of six differential equations, and is therefore difficult to analyze in depth. We use the theory of weakly coupled oscillators to reduce the dimensionality of the model in order to analyze its behavior more effectively.

3.3. Weakly Coupled Oscillators Theory

Applying the theory of weakly coupled oscillators allows us to analyze the relationship between intrinsic cell properties and the coupling between cells. In order to apply this theory to the Guevara model, we reduce the three-dimensional single-cell model to a "phase" model, consisting of a single differential equation describing the position of the system along its limit cycle in state space. A system close to, but not on, the limit cycle, is mapped to an *asymptotic phase* corresponding to a point on the limit cycle, defined by the phase whose limit is equal to the limit of the system as time approaches $+\infty$.

First, consider an oscillating cell with a period T. We denote the phase θ_1. The phase of the cell advances with time:

$$\theta_1 = t,\ \theta_1 \in [0, T).$$

After time T, phase resets to zero, such that $\theta_1 = t \mod T$. However, for convenience, we simply write $\theta_1 = t$.

Generally, heterogeneity in SAN cells' electrical properties results in a variation in their frequency of oscillation ($\Delta\omega$). Therefore, if we consider a second cell with phase θ_2 which has slightly different electrical properties from those of the first cell, the second cell obeys the model

$$\theta_2 = t + \Delta\omega t + \phi_0$$

where ϕ_0 is a phase shift depending on the second cell's initial condition relative to that of the first cell.

A perturbation to Cell 1 will result in a phase shift that depends on time, which we denote $\phi_1(t)$:

$$\theta_1 = t + \phi_1(t).$$

We call $\phi_1(t)$ the *relative phase* of Cell 1, as this denotes the location of the cell relative to its unperturbed phase on the limit cycle. If the perturbation is small enough, then the relative phase will change slowly. Using a multi-scale or "two-timing" approach, we can write the relative phase as a function of the slow time variable $\tilde{t} = \epsilon t$ for small ϵ (note that ϵ determines $\bar{g}$, and therefore scales the coupling strength), so that the phase of Cell 1 becomes

$$\theta_1(t, \tilde{t}) = t + \phi_1(\tilde{t}).$$

Similarly, we assume a small perturbation is applied to Cell 2, resulting in a relative phase ϕ_2 that changes on the slow time-scale $\tilde{t}$:

$$\theta_2(t, \tilde{t}) = t + \Delta\omega t + \phi_0 + \phi_2(\tilde{t})$$

We also now assume that the heterogeneity in the frequency of Cell 2, $\Delta\omega$, is sufficiently small that $\frac{\Delta\omega}{\epsilon}$ is $\mathcal{O}(1)$, and therefore we write the equation for θ_2 as

$$\theta_2(t, \tilde{t}) = t + \frac{\Delta\omega}{\epsilon}\tilde{t} + \phi_0 + \phi_2(\tilde{t}).$$

The theory of weakly coupled oscillators (see [**64**] for derivation) allows us to write the following differential equations governing the dynamics of the relative phasesϕ_1 and ϕ_2 over the slow time scale $\tilde{t}$:

$$\frac{d\phi_1}{d\tilde{t}} = \frac{1}{T}\int_0^T Z(t+\phi_1)\cdot I_C(V_{LC}(t+\phi_1+(\phi_2-\phi_1))), V_{LC}(t+\phi_1))dt$$
$$\frac{d\phi_2}{d\tilde{t}} = \frac{1}{T}\int_0^T Z(t+\phi_2)\cdot I_C(V_{LC}(t+\phi_2-(\phi_2-\phi_1))), V_{LC}(t+\phi_2))dt + \Delta\omega$$

where $Z(\theta)$ denotes the phase response curve (PRC) defining the phase shift of the cell in response to a delta function-like perturbation; $V_{LC}(t)$ represents the membrane potential V of a cell at phase t relative to a periodic action potential at steady-state (i.e., along the unperturbed limit cycle); and $I_C(V_i, V_j)$ represents the coupling function defining the effect of coupling from cell j on cell i (for $i,\ j = 1,\ 2$). Thus, the instantaneous effect of cell j on cell i is defined by integrating the product of the coupling function I_C at each point V_{LC} along the limit cycle with the phase response curve $Z(\theta)$. This relies on the theory of averaging (see [**25**]), which allows us to average the system over the period T of the limit cycle and remove the explicit dependence on the "fast" time variable t. Several methods exist to compute the PRC; in this case, the PRC was generated in XPP [**20**] by solving for the unique T-periodic solution to the adjoint equation for the linear operator representing the derivative of the phase model with respect to the fast time-scale. Fig. 3.4 shows the action potential representing one cycle of the oscillation in V versus the phase θ of the period (fig. 3.4A), and the corresponding phase response curve $Z(\theta)$ indicating the sensitivity of the system to perturbation at each point along the limit cycle (fig. 3.4B).

If the coupling function I_C is symmetric, the integral term depends only on the phase difference $\psi = \theta_2 - \theta_1$. We define the interaction function $H(\psi)$ as the influence exerted on one cell's phase by another cell with phase difference ψ, averaged over a limit cycle; that is:

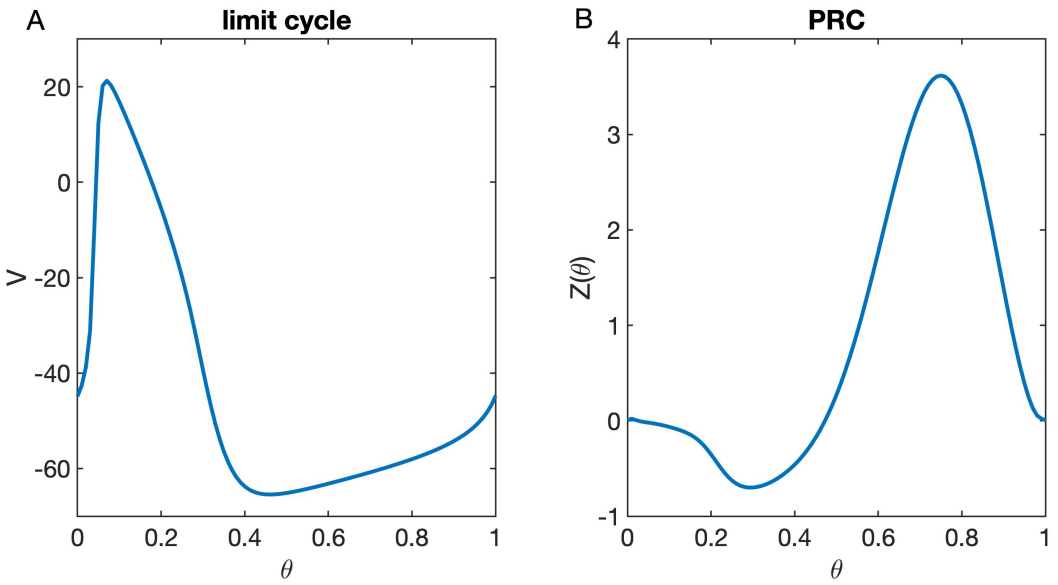

FIGURE 3.4. A: characteristic action potential for the Guevara model plotted over the phase θ describing the position of the system around the limit cycle (period $\sim$ 375ms). B: phase response curve indicating the sensitivity of the system at each point along the action potential to a delta-function-like, infinitesimal perturbation in the positive voltage direction.

$$H(-\psi) = \frac{d\phi_1}{d\tilde{t}} = \frac{1}{T}\int_0^T Z(t+\phi_1)\cdot I_C(V_{LC}(t+\phi_1+\psi)), V_{LC}(t+\phi_1))dt \tag{3.1}$$

$$H(\psi)+\Delta\omega = \frac{d\phi_2}{d\tilde{t}} = \frac{1}{T}\int_0^T Z(t+\phi_2)\cdot I_C(V_{LC}(t+\phi_2-\psi)), V_{LC}(t+\phi_2))dt + \Delta\omega.$$

Using the symmetry of $H(\psi)$ and $H(-\psi)$, we then define the function $\bar{g}G(\psi) := H(\psi) - H(-\psi)$. By subtracting the differential equations this further reduces the system to one differential equation for the phase difference ψ:

$$\frac{d\psi}{dt} = \frac{d\theta_2}{dt} - \frac{d\theta_1}{dt} = \frac{d\phi_2}{dt} - \frac{d\phi_1}{dt} = \bar{g}G(\psi) + \Delta\omega$$

That is,

$$\frac{d\psi}{dt} = \bar{g}G(\psi) + \Delta\omega.$$

The steady states of this equation determine the phase-locking of the system of two oscillators. In pairs of homogeneous SAN cells ($\Delta\omega = 0$) coupled by gap junctions, there is generally a stable equilibrium at $\psi = 0$, corresponding to synchrony, and an unstable equilibrium at $\psi = T/2$ corresponding to antiphase. Adding heterogeneity, captured by $\Delta\omega$, essentially shifts $G(\psi)$ vertically, which shifts the stable equilibrium from synchrony towards a nearby point; this stable equilibrium is referred to as a "1:1 phase-locked" steady state. Several features of the shape of $G(\psi)$ quantify the robustness of this phase-locked state:

(1) The absolute value of the slope of $G(\psi)$ at synchrony, i.e., $|G'(0)|$, determines how close or how far from synchrony the 1:1 phase-locked state will be as heterogeneity is added.

(2) The maximum absolute value of $G(\psi)$, i.e., $\max_\psi |G(\psi)|$, determines how large the frequency heterogeneity must be to abolish the 1:1 phase-locked steady state.

(3) The value of ψ at which $\max_\psi |G(\psi)|$ occurs, i.e., $\psi(G_{max})$, measures the states at which the system will accumulate as heterogeneity is increased.

While $G(\psi)$ provides statistics that measure the robustness of phase-locking to small heterogeneity, a second measure known as the cross-correlogram for the two oscillators measures the robustness to random noise. In the presence of additive white noise, the two-cell system will fluctuate between different states, taking on a variety of phase differences ψ with frequencies corresponding to the stability of each value of ψ. The probability distribution that results from this experiment captures the likelihood of the system to take on each phase shift ψ. This probability distribution, also known as the cross-correlogram and denoted $\rho(\psi)$, can be calculated explicitly using the parameters in the system (derivation in [**64**]):

$$\rho(\psi) = \frac{1}{N} e^{M(\psi)} \left[\frac{e^{-\alpha T \Delta\omega} - 1}{\int_0^T e^{-M(\bar{\psi})} d\bar{\psi}} \int_0^\psi e^{-M(\bar{\psi})} d\bar{\psi} + 1 \right],$$

where

$$M(\psi) = \alpha \int_0^\psi (\Delta\omega + G(\bar{\psi})) d\bar{\psi},$$

N is a normalization factor such that $\int_0^T \rho(\psi)d\psi = 1$, and $\alpha = \frac{\epsilon}{\delta^2\sigma_\psi^2}$ represents the ratio of the strength of the coupling to the variance of the noise. Since $\rho(\psi)$ depicts the likelihood for the system to take on each state ψ, we use the value of $\rho(0)$ as a measure of the stability of synchrony and $\rho(T/2)$ as a measure of the instability of antiphase.

3.3.1. Extension: time-dependent gating. In order to find any potential effects of time-dependent voltage-gating on synchrony in pairs of SAN cells, we extend the theory of weakly coupled oscillators to allow for conductance to develop on a slow time-scale commensurate with changes to phase shift due to coupling. We introduce a linear differential equation with a single time constant to model the conductance g_j across the gap junction:

$$\frac{dg_j}{dt} = \frac{1}{\tau_c}(g_{j,ss} - g_j)$$

We then assume that g_j changes on the same time scale as the relative phase, and therefore that, like the differential equations for relative phase of each oscillator, the ODE for conductance can be averaged over the period. We augment the system of equations (3.1) with an additional ODE for g_j, averaged over the period T:

$$\frac{d\phi_i}{d\tilde{t}} = \frac{1}{T}\int_0^T Z(t+\phi_i)\cdot I_C(V_{LC}(t+\phi_i+(\phi_j-\phi_i)), V_{LC}(t+\phi_i))dt,\ i,j=1,2$$
$$\frac{dg_j}{d\tilde{t}} = \frac{1}{\tau_c}\left[\frac{1}{T}\int_0^T g_{j,ss}(V_{LC}(t+\phi_i), V_{LC}(t+\phi_j))dt - g_j\right]$$

Recall that the differential equation for ϕ_i depends on g_j through the coupling current, $I_C = g_j \cdot \Delta V$. This system of three equations can then be reduced to a system of two equations for the phase difference $\psi = \phi_2 - \phi_1$ and the conductance g_j:

$$\frac{d\psi}{d\tilde{t}} = g_j(H(\psi) - H(-\psi))$$
$$\frac{dg_j}{d\tilde{t}} = \frac{1}{\tau_c}\left(g_{j,\infty}(\psi) - g_j\right)$$

where $g_{j,\infty}$ is the average of $g_{j,ss}(\Delta V)$ over a cycle of the action potential:

$$g_{j,\infty}(\psi) = \frac{1}{T}\int_0^T g_{j,ss}(V_{LC}(t+\psi) - V_{LC}(t))dt$$

and H is defined as in eq. (3.1). We can analyze the phase plane of the two-variable system ψ and g_j in the time-dependent conductance case to ascertain how time-dependent voltage gating affects systems of two weakly coupled oscillators in this sinoatrial node cell model.

3.4. Results

We apply several protocols involving systems of two and three coupled cells to evaluate the differences in robustness of phase locking to frequency heterogeneity and Gaussian noise.

3.4.1. Two Symmetrically Coupled SAN Cells. The most basic system in which to apply the theory of weakly coupled oscillators to a model of SAN cells is a pair of cells with symmetric coupling.

First, we investigate the role of each gap junction gating parameter ($g_{j,min}$, A, and $V_{j,0}$) on the shape of the coupling function $G(\psi) = \frac{d\psi}{dt}$ for a pair of two homogeneous SAN cells. Values of ψ where $G(\psi) = 0$ correspond to 1:1 phase-locked states for the pair of cells. In all cases with two homogeneous cells, we observe two steady states, corresponding to synchrony and antiphase. The synchronous steady state is the only stable equilibrium for the paired system; antiphase is consistently an unstable equilibrium (figure 3.5).

We examine how the voltage dependence of gap junctional coupling impacts the robustness of synchrony, or 1:1 phase locking, in the presence of small frequency heterogeneity ($\Delta\omega$) and noise. Since the dynamics of phase difference ψ are governed by the differential equation

$$\frac{d\psi}{dt} = \bar{g}G(\psi) + \Delta\omega,$$

in the presence of heterogeneity the equilibria for ψ occur at ψ^* where

$$G(\psi^*) = -\frac{\Delta\omega}{\bar{g}}.$$

Several metrics can be used to quantify the degree of "robustness" of phase locking as a stable steady state of a system of ordinary differential equations, and we evaluate the effects of parameters defining voltage dependence of gap junction conductance on each of these metrics. First, we note that a slight heterogeneity $\Delta\omega$ in the frequencies of the two cells shifts $\frac{d\psi}{dt}$ vertically, therefore shifting the equilibria for ψ and, if the heterogeneity is large enough, eliminating one or more equilibria. Therefore, one metric of the robustness of phase-locking to heterogeneity is the maximum of $G(\psi)$, as this measures the size of heterogeneity necessary to eliminate the 1:1 phase-locked steady state. Second, since the equilibrium point at synchrony ($G(0) = 0$) is stable if $\frac{dG}{d\psi}\big|_0 < 0$, robustness of the synchronous steady state can be thought of as the magnitude of the negative slope at this point, i.e., $-\frac{dG}{d\psi}\big|_0$. This indicates how close to synchrony the steady state will remain as small-amplitude frequency heterogeneity $\Delta\omega$ is added to one cell. Finally, a third, related metric is $\psi(G_{max})$, the phase at which G attains its maximum; this measures the phase shift that the cells will approach as heterogeneity is added. If $\psi(G_{max})$ is close to 0 or T, the pair will remain close to synchrony even as heteroeneity is added, just before the 1:1 phase-locking is lost; if $\psi(G_{max})$ is close to $T/2$, on the other hand, small heterogeneity will shift the pair of cells toward antiphase.

The dependence of the function $G(\psi)$ on gap junctional gating parameters are summarized in figures 3.5 and 3.6. Increasing $g_{j,min}$, the minimal conductance at high membrane potential difference ΔV, increases the amplitude of $G(\psi)$ and shifts the phase $\psi(G_{max})$ at which the maximum occurs slightly toward antiphase, and increases the slope of $G(\psi)$ at antiphase – thereby increasing the instability of the unstable equilibrium – but does not affect the slope at synchrony $|G'(0)|$ (fig. 3.5A, fig. 3.6A-C). This is consistent with the fact that increased $g_{j,min}$ enhances the gap junctional conductance for cell pairs at large membrane potential differences ΔV, but does not affect the conductance for pairs of cells with small membrane potential differences. Since gap junctional conductance acts as a synchronizing force, higher minimal conductance is expected to increase the robustness of 1:1 phase-locking in response to heterogeneity and to destabilize antiphase; however, the local

stability of synchrony is not affected since changes to $g_{j,min}$ do not affect conductance when ΔV is near zero.

As $|V_{j,0}|$ approaches zero, the relative width of the high-conductance window of $g_{j,ss}(\Delta V)$ narrows. This results in decreased amplitude of $G(\psi)$ and reduced slope at antiphase $G'(T/2)$, representing a reduction in the instability of antiphase. Shifting $V_{j,0}$ towards zero also slightly reduces the slope at synchrony (fig. 3.5B, fig. 3.6D-F). The reduced amplitude, decreased steepness at synchrony and decreased slope at antiphase are expected, as changing $V_{j,0}$ toward zero reduces the range of transjunctional voltage ΔV over which conductance is high, and therefore reduces the coupling conductance for pairs of cells with membrane potential differences. Pairs of cells at different membrane potentials therefore exert less coupling current on each other, and are thus less likely to shift towards synchrony.

Increasing A represents a steeper drop-off in the conductance $g_{j,ss}(\Delta V)$ as $|\Delta V|$ increases. In our model, increasing A reduces the amplitude of $G(\psi)$ and shifts the phase $\psi(G_{max})$ at which the maximum occurs closer to synchrony, widening the range of ψ over which $G \approx G_{max}$ so that the shape of $G(\psi)$ becomes more square pulse-like (fig. 3.5C, fig. 3.6G-I). Increased A also results in reduced slope at antiphase, and slightly increasd magnitude of the slope at synchrony $|G'(0)|$. These trends are expected: increased A decreases the conductance for cell pairs at very different membrane potentials, which will decrease the instability of antiphase and reduce the amplitude of $G(\psi)$. However, increasing A also increases the conductance for cell pairs at similar membrane potentials, i.e., small $|\Delta V|$, which increases the magnitude of the slope at synchrony, $|G'(0)|$.

The relationships between each parameter and key metrics of $G(\psi)$, namely G_{max}, $\psi(G_{max})$, and $|G'(0)|$, are captured in fig. 3.6. Together, the three parameters $V_{j,0}$, $g_{j,min}$ and A shift the function, including changing the slope of G at synchrony and antiphase, the amplitude of G and the point at which the maximum is achieved. However, within a physiological parameter range these changes do not alter the number of steady states or their stability.

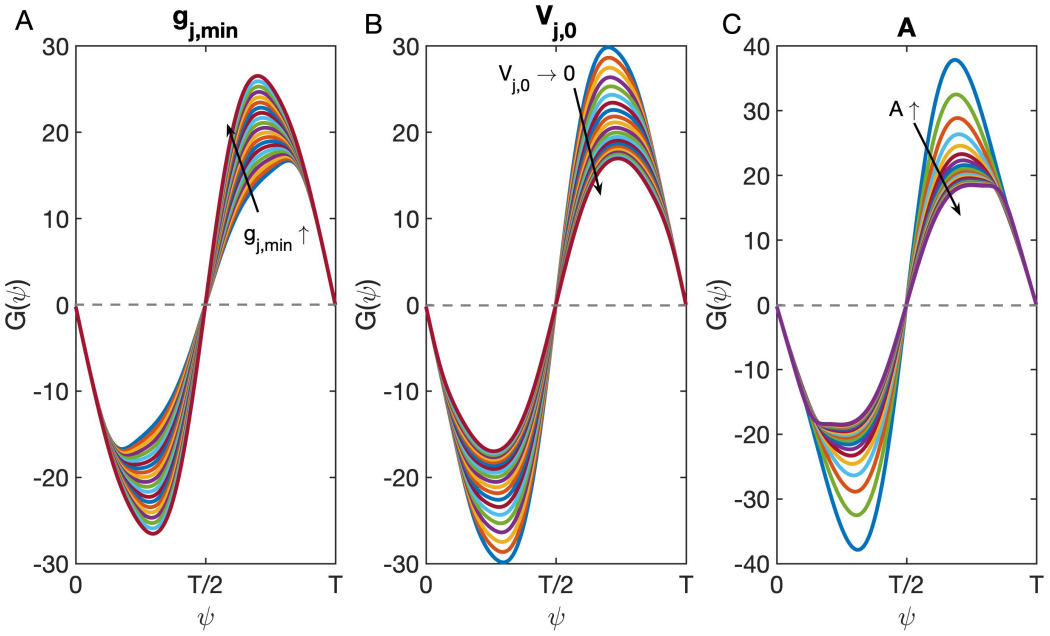

FIGURE 3.5. Effects of voltage-dependent gap junction gating parameters on $G(\psi)$ phase diagram for the phase difference between two coupled cells. The three parameters $g_{j,min}$, $V_{j,0}$, and A each shift the function $G(\psi)$ by changing the height of the maximum value and the phase at which this maximum occurs. Parameters change the amplitude of G and the slope of G at 0 and at $T/2$, modifying the stability of synchrony and the instability of antiphase. However, within a physiological parameter range these changes do not alter the number of steady states or their stability.

The cross-correlogram $\rho(\psi)$ for the two-cell system, as described in Schwemmer and Lewis [**64**], describes the expected phase differences in a coupled system in the presence of Gaussian random noise. In fig. 3.7, we show the effects of each voltage-gating parameter on the shape of the cross-correlogram with $\alpha = 0.2$. Changes to each of the three parameters $g_{j,min}$, $V_{j,0}$ and A affect the maximum of ρ at synchrony ($\psi = 0, T$), as well as the minimum at antiphase ($\psi = T/2$) and the steepness of the function between the minimum and maxima. These effects are shown in fig. 3.7. As the minimum conductance $g_{j,min}$ increases, $\rho(\psi)$ becomes steeper, such that the maxima at $\psi = 0, T$ are higher and the minimum at $\psi = T/2$ is lower (fig. 3.7A). The increased maximum of ρ at synchrony is expected, since $g_{j,min}$ increases conductance between the two cells, which increases the propensity for the cells'

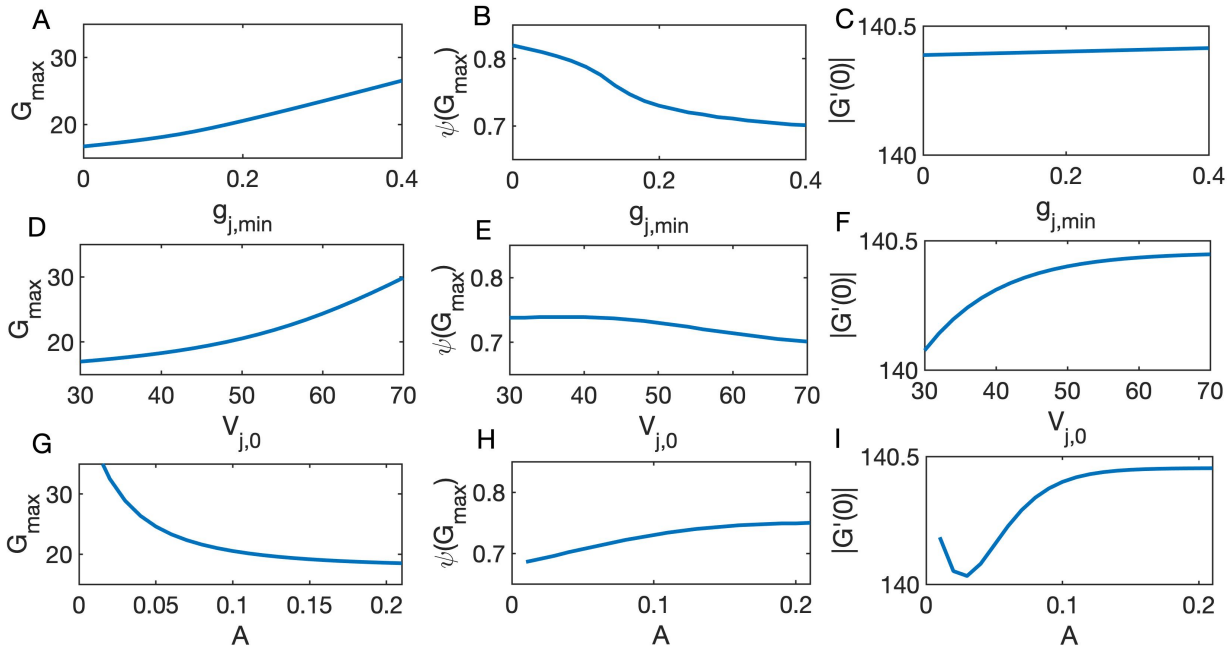

FIGURE 3.6. Effects of the three voltage-dependent gating parameters $g_{j,min}$, $V_{j,0}$, and A on metrics of robustness of 1:1 phase-locking in a pair of cells. Amplitude $G_{max} = \max_\psi(G(\psi))$ indicates the size $\Delta\omega$ of frequency heterogeneity that will abolish the steady state; the slope $|G'(0)|$ at the homogeneous stable steady state indicates how close to synchrony the steady state will remain as small-amplitude heterogeneity is added to one cell; the location $\psi(G_{max}) = \psi^*$ at which the maximum $\max_\psi(G(\psi))$ is achieved (that is, $G(\psi^*) = \max_\psi(G(\psi))$) predicts the most commonly visited phase differences of cells as frequency heterogeneity is increased.

membrane potentials to converge toward each other. As the relative width $|V_{j,0}|$ of the high-conductance window of the voltage-dependence function narrows ($|V_{j,0}| \to 0$), the maximum of $\rho(\psi)$ near synchrony decreases, but the minimum near antiphase increases (fig. 3.7B). These trends are again expected, as reducing $|V_{j,0}|$ decreases the overall conductance between the pair of cells, and therefore destabilizes their synchrony and phase-locking. As the relative steepness A of the voltage-gating function increases, ρ changes toward lower maxima at $\psi = 0, T$ and a higher minimum at $\psi = T/2$ (fig. 3.7C). This can be explained by the fact that increasing A reduces the overall conductance between the pair of cells, especially when ΔV is large.

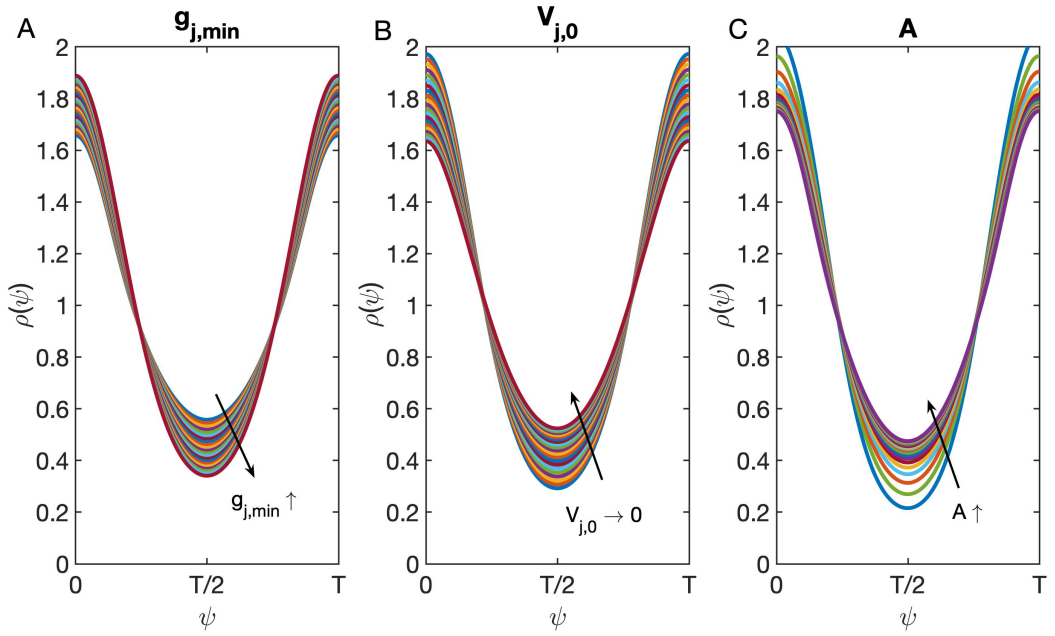

FIGURE 3.7. Cross-correlograms summarize the stability of various phase shifts in a pair of two coupled cells under random noise. The three parameters defining voltage-dependent gap junction gating $V_{j,0}$, $g_{j,min}$ and A each shift the cross-correlogram to be steeper and flatter at different phases, changing the relative stability of synchrony and antiphase and nearby regions of phase space. However, there are no notable qualitative changes in the stability or number of steady states within a physiological range of parameters.

The relationships between each parameter and the minima and maxima of ρ are quantified in figure 3.8. As the minimum conductance $g_{j,min}$ increases, ρ_{max} (stability of synchrony) increases and ρ_{min} (instability of antiphase) decreases (fig. 3.8A, D). As the width $|V_{j,0}|$ increases, similarly, ρ_{max} increases and ρ_{min} decreases (fig. 3.8 B, E). As the steepness A of gating increases, the maximum ρ_{max} decreases and the minimum ρ_{min} increases (fig. 3.8 C, F).

The shape of the cross-correlogram does not change markedly across variations in gating parameters. Although the voltage-dependence changes the relative sizes of the maxima at $\psi = 0$ and T and minimum at $\psi = T/2$, the qualitative shape of the cross-correlogram does not change. Hence, we predict that voltage-dependent gating will not change the qualitative behavior of a two-cell coupled system in response to random channel noise affecting each cell's membrane potential.

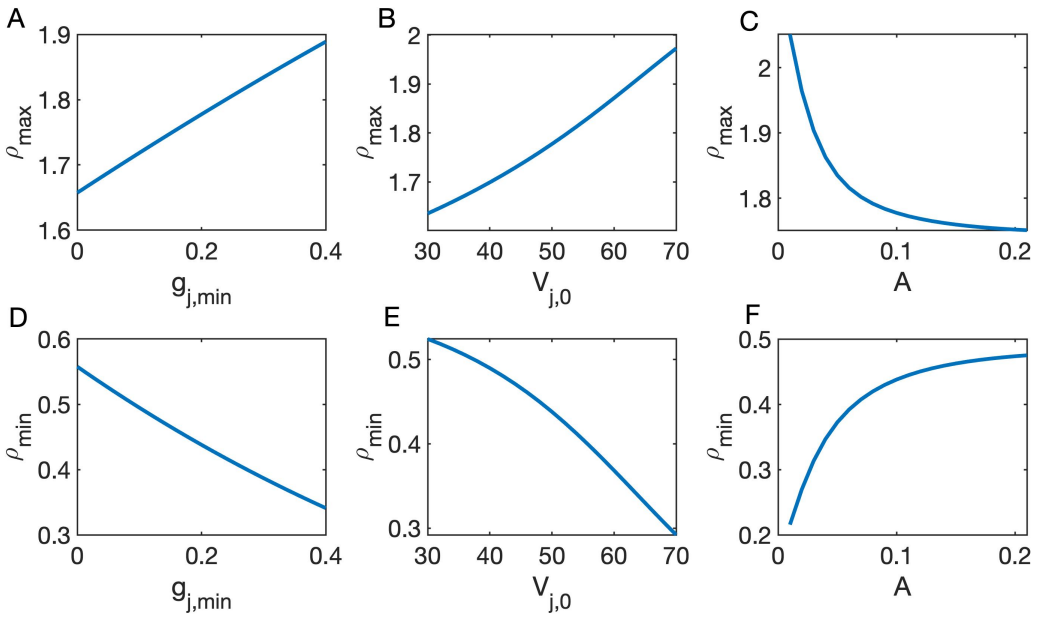

FIGURE 3.8. As each parameter changes, the maxima and minima of $\rho(\psi)$, near synchrony and antiphase respectively, shift. As $g_{j,min}$ increases, $\rho(\psi)$ becomes steeper, such that the maxima at $\psi = 0, T$ are higher and the minimum at $\psi = T/2$ is lower. Similarly, as $V_{j,0} \to 0$, the slope of $\rho(\psi)$ between 0 and $T/2$ and between $T/2$ and T becomes steeper. As A increases, ρ shifts towards lower maxima at $\psi = 0, T$ and a higher minimum at $\psi = T/2$.

Results from all of our simulations of two SAN cells with symmetric gap junctional coupling, captured in figures 3.5, 3.6, 3.7 and 3.8, indicate that each voltage gating parameter shifts the robustness of phase-locking in a pair of symmetrically coupled cells. Based on the voltage-gating parameters for Cx45 and Cx43 gap junctions, we expect synchrony in cells coupled with Cx45 gap junctions to be less robust than in cells coupled with Cx43 gap junctions. However, in all of our results, synchrony remains the only stable steady state and antiphase remains the only unstable steady state. None of the the three parameters controlling voltage-gated coupling alter the qualitative behavior, i.e. the number or stability of steady states, of the dynamical system.

3.4.2. Three SAN Cells with Symmetric Coupling. It is possible that the minimal two-cell case does not fully capture the effects of different voltage-gating properties of gap junctions on systems of weakly coupled oscillating cells, and that these effects only arise

in systems of three or more cells. Therefore, we investigate, in a network of three cells, how the parameters determining voltage-dependent gap junction conductance influence the robustness of phase-locking. For completeness, given that the sinoatrial node contains a spatially complex mesh of cells, we consider both the setup in which each cell is coupled to every other cell and in which cells are arranged in a linear array with only nearest-neighbor coupling (see next section).

The system of three cells generates two phase differences, $\psi_1 = \theta_2 - \theta_1$ and $\psi_2 = \theta_3 - \theta_2$. As in the two-cell case, each cell's phase is governed by a differential equation defined by the convolution of the phase response curve and the coupling current; in the three-cell case, however, the coupling current is either the average of the coupling current from the remaining two cells (in the case of all-all coupling) or from the adjacent cell(s) (nearest-neighbor coupling). The differential equations governing the phase differences, as in the two-cell case, arise from subtracting the differential equations for each individual phase. We analyze the dynamics of the two phase differences ψ_1 and ψ_2 using a two-dimensional phase plane, analogous to the G function in the two-cell model. The phase plane identifies steady states and the sign of the derivatives of each variable in each region of state space. We show phase planes for a default parameter set ($g_{j,min} = 0.2$, $V_{j,0} = 50$, $A = 0.1$) and demonstrate how the phase plane changes as frequency heterogeneity is added to cell 3. We then use these results to analyze how the voltage-dependence of gap junctional coupling influences the robustness of phase-locking in the three-cell network.

3.4.2.1. *Three SAN Cells with All-to-all Coupling.* We first consider a system of three cells with all-all coupling, where one cell has the potential for a slight frequency heterogeneity $\Delta\omega$. The equations for each cell are the following:

$$\frac{d\phi_1}{d\tilde{t}} = \frac{1}{T}\left(\frac{1}{2}\int_0^T Z(t+\phi_1)\cdot I_C(V_{LC}(t+\phi_1+(\phi_2-\phi_1)), V_{LC}(t+\phi_1))dt \right.$$
$$\left. + \frac{1}{2}\int_0^T Z(t+\phi_1)\cdot I_C(V_{LC}(t+\phi_1+(\phi_3-\phi_1)), V_{LC}(t+\phi_1))dt\right)$$
$$\frac{d\phi_2}{d\tilde{t}} = \frac{1}{T}\left(\frac{1}{2}\int_0^T Z(t+\phi_2)\cdot I_C(V_{LC}(t+\phi_2-(\phi_2-\phi_1)), V_{LC}(t+\phi_2))dt \right.$$
$$\left. + \frac{1}{2}\int_0^T Z(t+\phi_1)\cdot I_C(V_{LC}(t+\phi_2+(\phi_3-\phi_2)), V_{LC}(t+\phi_2))dt\right)$$
$$\frac{d\phi_3}{d\tilde{t}} = \frac{1}{T}\left(\frac{1}{2}\int_0^T Z(t+\phi_3)\cdot I_C(V_{LC}(t+\phi_3-(\phi_3-\phi_2)), V_{LC}(t+\phi_3))dt \right.$$
$$\left. + \frac{1}{2}\int_0^T Z(t+\phi_3)\cdot I_C(V_{LC}(t+\phi_3-(\phi_3-\phi_1)), V_{LC}(t+\phi_3))dt + \Delta\omega\right)$$

By subtracting and using symmetry, and observing that $\theta_3 - \theta_1 = \psi_1 + \psi_2$, we obtain the differential equations for phase differences $\psi_1 = \theta_2 - \theta_1$ and $\psi_2 = \theta_3 - \theta_2$:

$$\frac{d\psi_1}{d\tilde{t}} = \frac{1}{2}(G(\psi_1) + H(-\psi_2) - H(-(\psi_1+\psi_2)))$$
$$\frac{d\psi_2}{d\tilde{t}} = \frac{1}{2}(G(\psi_2) + H(\psi_1+\psi_2) - H(\psi_1)) + \Delta\omega$$

Fig. 3.9A depicts the (ψ_1, ψ_2) phase plane for the default parameter set, with identical cells ($\Delta\omega = 0$). Note that due to the periodicity of both phase differences, the flow is in fact on a torus rather than a plane. Nullclines are shown in blue (ψ_1) and red (ψ_2). Note that points on the ψ_i nullcline where ψ_i is equal to zero or one correspond to synchrony between a particular pair of cells. For example, $\frac{d\psi_1}{dt} = 0$ when $\psi_1 = 0$, because along this line, $\phi_1 = \phi_2$, and therefore the coupling current from ϕ_1 to ϕ_2 (and vice versa) is zero. Steady states are depicted in fig. 3.9A with filled circles (stable) and open circles (unstable); note that all four stable steady states are actually the single synchronous steady state. Arrows

depict the direction of flow in each region of the torus. Three trajectories are shown, all of which approach synchrony. In panel B of fig. 3.9, we show the time-course of the yellow trajectory in panel A, with initial conditions (0.2, 0.4). Similarly, fig. 3.9 C shows the time-course for the green trajectory in A, with initial conditions $(0.7, 0.4)$. In both B and C, after several cycles of oscillation corresponding to several cellular action potentials, all three cells synchronize; this is shown in the phase plane by the fact that each of the trajectories approaches one of the four corners of the phase plane, all of which correspond to synchrony.

As heterogeneity $\Delta\omega$ is added, the ψ_2 nullcline shifts (fig. 3.10), moving the steady states for the system. The unique stable steady state remains close to synchrony, but shifts slightly towards positive ψ_2 as the intrinsic frequency of cell 3 increases. Thus, as cell 3's frequency accelerates slightly, the system approaches a phase-locked state in which cells 1 and 2 are in synchrony, and cell 3 is phase-locked at a fixed, phase-advanced position relative to cells 1 and 2. Fig. 3.10 shows the changes to the phase plane over a range of $\Delta\omega$ from 0 to 21.2. Blue curves indicate the ψ_1 nullcline, and red curves indicate the ψ_2 nullclines for each value of $\Delta\omega$ (dash-dot curve corresponds to $\Delta\omega = 0$). At sufficiently high $\Delta\omega$, two of the unstable steady states vanish in a saddle-node bifurcation (SNB) as shown in fig. 3.10 with dashed curve ($\Delta\omega = 12$). As heterogeneity is increased beyond this point, a second SNB occurs and eliminates the stable steady states (shown in fig. 3.10 with dotted curve, $\Delta\omega = 21.2$). The value of $\Delta\omega$ at the second SNB, denoted $\Delta\omega_{SNB}$ below, provides the threshold for a frequency heterogeneity in one cell to desynchronize the third, heterogeneous cell from the two identical cells.

In fig. 3.11, we show the phase plane and corresponding trajectories with a sufficiently large heterogeneity to eliminate the steady states. Fig. 3.11A depicts the phase plane for $\Delta\omega = 21.2$; blue curves denote the ψ_1 nullcline and red curve, the ψ_2 nullcline. The heterogeneity shifts the ψ_2 nullcline sufficiently so that there are no equilibria. Yellow and green trajectories in fig. 3.11A are those with initial conditions $(0.2, 0.4)$ and $(0.4, 0.7)$ as in fig. 3.9A. In the absence of a stable equilibrium, the third cell fails to synchronize with the

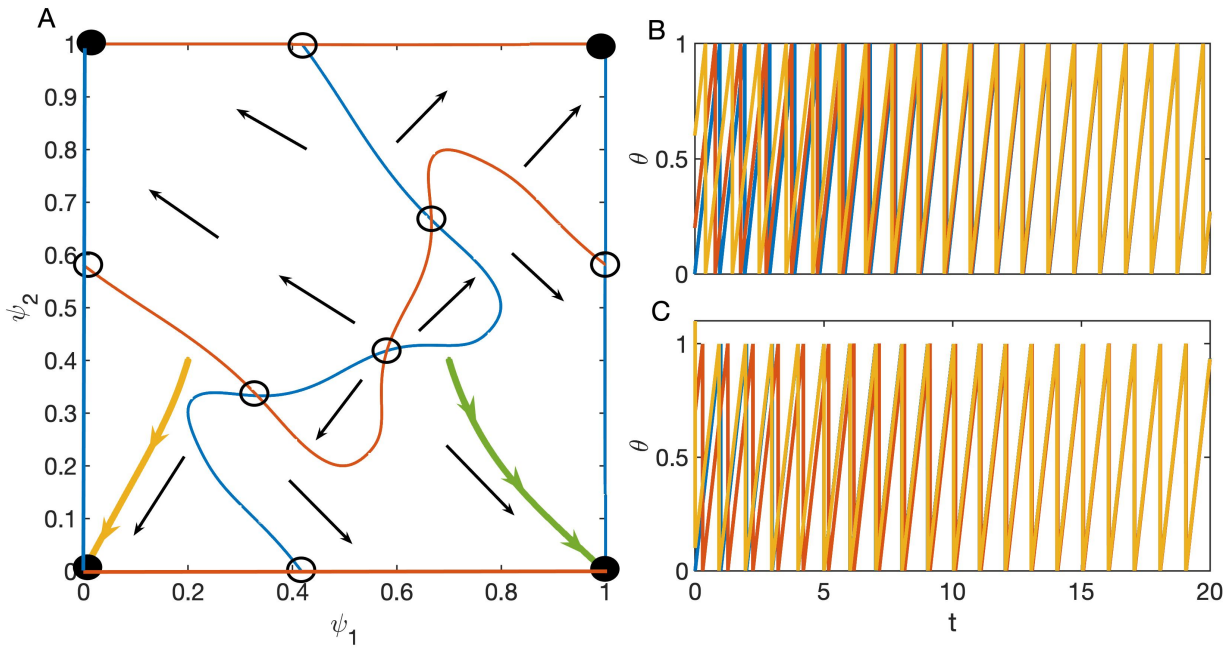

FIGURE 3.9. A: The phase plane for two phase differences $\psi_1 = \theta_2 - \theta_1$ and $\psi_2 = \theta_3 - \theta_2$ for standard parameters $g_{j,min} = 0.2$, $V_{j,0} = 0.5$, $A = 0.2$. Nullclines are shown in blue (ψ_1) and red (ψ_2). Open and filled circles indicate unstable and stable steady states. Trajectories with initial conditions $(0.2, 0.4)$, $(0.4, 0.6)$, and $(0.7, 0.4)$ are shown in yellow and green (A) with arrowheads indicating the direction of flow. B: corresponding time-course for trajectory with initial condition $(0.2, 0.4)$ as shown in yellow and green trajectories in panel A. After several action potentials, all three cells synchronize. C: time-course for trajectory with initial condition $(0.7, 0.4)$, as in green trajectory in A. As in B, the three cells synchronize after a sufficient amount of time.

two identical cells. However, cells 1 and 2 approach synchrony over time, as demonstrated by the fact that the yellow and green trajectories in fig. 3.11A approach vertical lines at $\psi_1 = 0, 1$ over time. The phase of the third cell slowly oscillates around the two phase-locked, identical cells, exhibiting the phenomenon known as phase walkthrough. Rather than reaching a synchronous equilibrium, the trajectories exhibit phase walk-through. The time courses corresponding to yellow and green trajectories are shown in fig. 3.11B and C, respectively. In both panels B and C, the blue and red curves representing time-courses for cells 1 and 2 synchronize after several cycles, but the third cell (yellow) does not phase-lock with the pair. The system of three cells does not approach a phase-locked steady state over time.

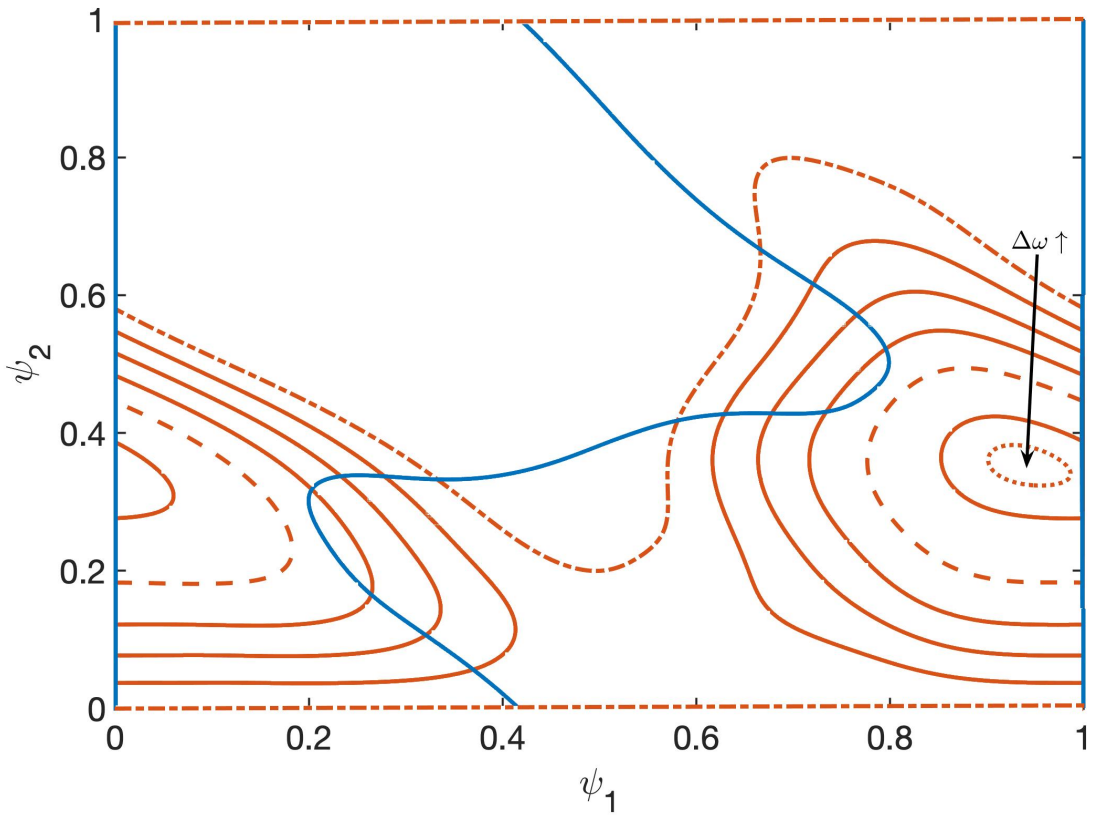

FIGURE 3.10. The phase plane for two phase differences $\psi_1 = \theta_2 - \theta_1$ and $\psi_2 = \theta_3 - \theta_2$ for standard parameters. Intersections of red and blue nullclines indicate stable and unstable phase-locked states. As heterogeneity of the third cell $\Delta\omega$ increases from 0 to 21.2 (red nullclines: $\Delta\omega = 0$ [dash-dot curve], 4, 8, 12, 16, 20, 21.2), the system undergoes a saddle-node bifurcation in which two of the unstable steady states disappear, but a stable phase-locked equilibrium remains (dashed curve, $\Delta\omega = 12$). As $\Delta\omega$ continues to increase, there is a second saddle-node bifurcation at which the third cell ceases to phase-lock with the identical cell pair (dotted curve, $\Delta\omega = 21.2$).

We are interested in the relationship between voltage gating parameters and synchrony. In fig. 3.12 we investigate how the three voltage-gating parameters V_0, $g_{j,min}$ and A affect the threshold $\Delta\omega_{SNB}$ at which the phase-locked steady state is eliminated. As the parameters of voltage gating change they shift the phase plane. As $g_{j,min}$ increases, the curvature of the nullclines increases, but the number of steady states remains unchanged and their locations do not change (fig. 3.12A). Similarly, as $V_{j,0}$ approaches zero (fig. 3.12B) and as A increases

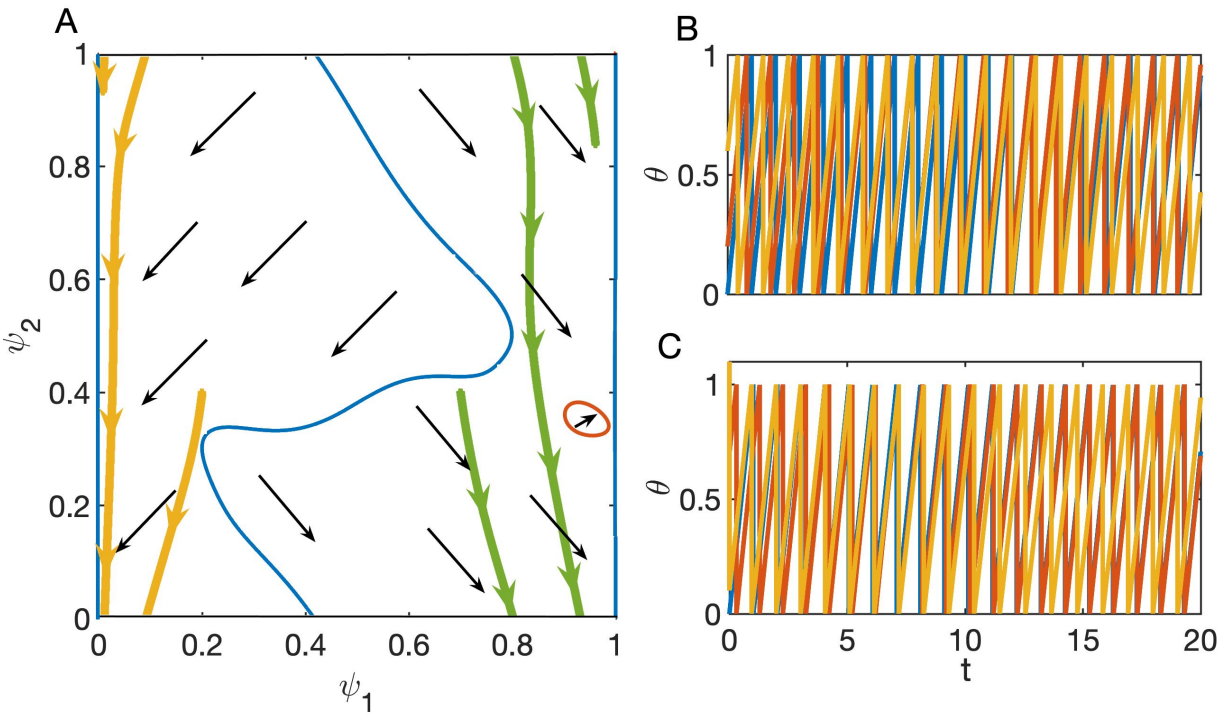

FIGURE 3.11. A: The phase plane for two phase differences $\psi_1 = \theta_2 - \theta_1$ and $\psi_2 = \theta_3 - \theta_2$ for standard parameters $g_{j,min} = 0.2$, $V_{j,0} = 0.5$, $A = 0.2$ and $\Delta\omega = 21.2$. Nullclines are shown in blue (ψ_1) and red (ψ_2). There are no steady states, as indicated by the lack of intersections of red and blue nullclines. Trajectories with initial conditions $(0.2, 0.4)$ and $(0.7, 0.4)$ are shown in yellow and green with arrowheads indicating the direction of flow (A). Due to the heterogeneity of ϕ_3, the cells do not synchronize over time, although the pair of cells 1 and 2 approach synchrony (vertical blue lines at $\psi_1 = 0, 1$). B: corresponding time-course for trajectory with initial condition $(0.2, 0.4)$ as shown in yellow and green trajectories in panel A. Cells 1 and 2 (blue and red) synchronize after several cycles, while cell 3 (yellow) does not phase-lock with the pair. C: time-course for trajectory with initial condition $(0.7, 0.4)$, as in green trajectory in A. As in B, the three cells do not synchronize over time, but the pair of cells 1 and 2 (blue and red) do synchronize.

(fig. 3.12C), the curvature of each nullcline is reduced but the number and location of steady states remain the same.

As heterogeneity $\Delta\omega$ of the third cell increases from zero, the system undergoes a saddle-node bifurcation whereby the stable equilibrium is abolished. Changes to the nullclines influence the threshold for the frequency shift $\Delta\omega$ in the third cell necessary to desynchronize from the homogeneous pair and undergo phase walk-through. The threshold $\Delta\omega_{SNB}$

therefore changes depending on each parameter, and can be considered a measure of robustness of the phase-locked, stable equilibrium state for the three-cell system. As $g_{j,min}$ increases, $\Delta\omega_{SNB}$ increases (fig. 3.12D); this is expected, as increased $g_{j,min}$ increases the coupling between cells at very different voltages, acting to move cells towards synchrony. As $|V_{j,0}|$ increases, $\Delta\omega_{SNB}$ increases (fig. 3.12E), which is also consistent with our expectations, as increased $|V_{j,0}|$ means the window of high conductance widens with respect to transjunctional potential. This broader range of high conductance also moves cells towards synchrony, and therefore increases the size of heterogeneity necessary to desynchronize the network. Finally, as A increases, $\Delta\omega_{SNB}$ decreases slightly (fig. 3.12F), because increased A diminishes the "tails" of the voltage dependent conductance $g_{j,ss}$, reducing the magnitude of coupling for cells at different voltages. Although both nullclines shift slightly as a result of changes to the gating parameters, changing the robustness of phase-locking, there is no qualitative change in behavior to the overall phase plane.

We consider the possibility that one role of specific types of gap junctions in the SAN, where heterogeneous input from the peripheral nervous system modulates individual cells' frequencies, may be to modulate the effects of cells of one freqeuency on cells of a different frequency. The effects of a third cell of a different frequency on the oscillations of a pair of synchronized, identical cells can be assessed by finding the period of time over which the third cell "walks through" the phase of the two-cell pair and the average effects of the third cell's input on the frequencies of the pair over this slow walk-through period (figure 3.13). In fig. 3.13 we examine how the parameters of voltage gating influence (1) the period of a third cell's walk-through with respect to the period of the pair of identical cells and (2) the average effects of the third cell on the frequency of the pair. Each parameter shifts the period and average effect of the third cell monotonically: while increasing $|V_{j,0}|$ and $g_{j,min}$ increase both the period and influence of the third cell, increasing A generally diminishes the period and the impact of the third cell. Overall, a third cell has a greater influence in cells coupled with Cx43 gap junctions than in cells coupled with Cx45 gap junctions. However, there is

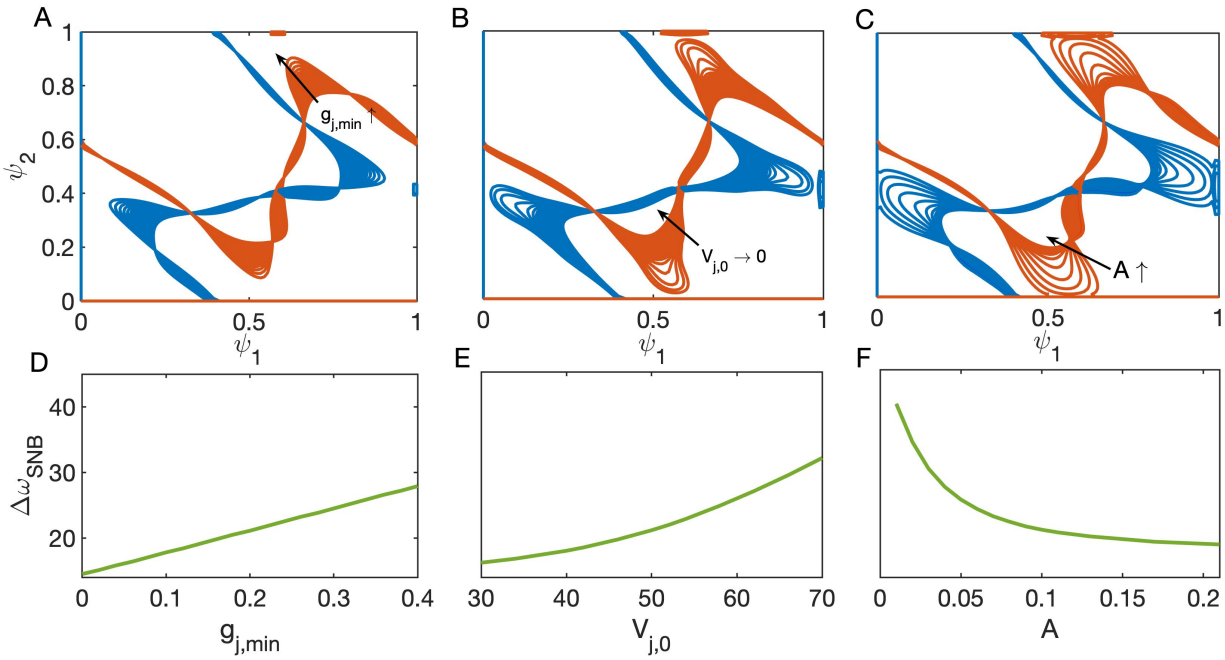

FIGURE 3.12. A-C: effects of each parameter $V_{j,0}$, $g_{j,min}$ and A on the phase plane for phase differences in a three-cell all-to-all coupled system. As $g_{j,min}$ increases, the curvature of the nullclines increases, but the number of steady states remains unchanged and their locations do not change. Similarly, as $V_{j,0}$ approaches zero and as A increases, the curvature of each nullcline is reduced but the number and location of steady states remain the same. D-F: As heterogeneity $\Delta\omega$ of the third cell increases from zero, the system undergoes a saddle-node bifurcation whereby one of the steady states is abolished. The threshold $\Delta\omega_{SNB}$ changes depending on each parameter: as $g_{j,min}$ increases, $\Delta\omega_{SNB}$ increases (D); as $|V_{j,0}|$ increases, $\Delta\omega_{SNB}$ increases (E); as A increases, $\Delta\omega_{SNB}$ decreases (F).

no difference in the qualitative shape of the relationship between heterogeneity, period, and phase effect of a third cell between the two types of gap junctions.

3.4.2.2. *Three SAN Cells with Nearest-neighbor Coupling.* Cells in the SAN are coupled with surrounding cells only, and it is possible that a network of three cells with nearest-neighbor coupling captures the important dynamics of the effects of gap junctions more effectively than does a network with all-to-all coupling.

As with all-all coupling, we use the theory of weakly coupled oscillators to construct differential equations for the three cells coupled in a nearest-neighbor arrangement, with ϕ_2

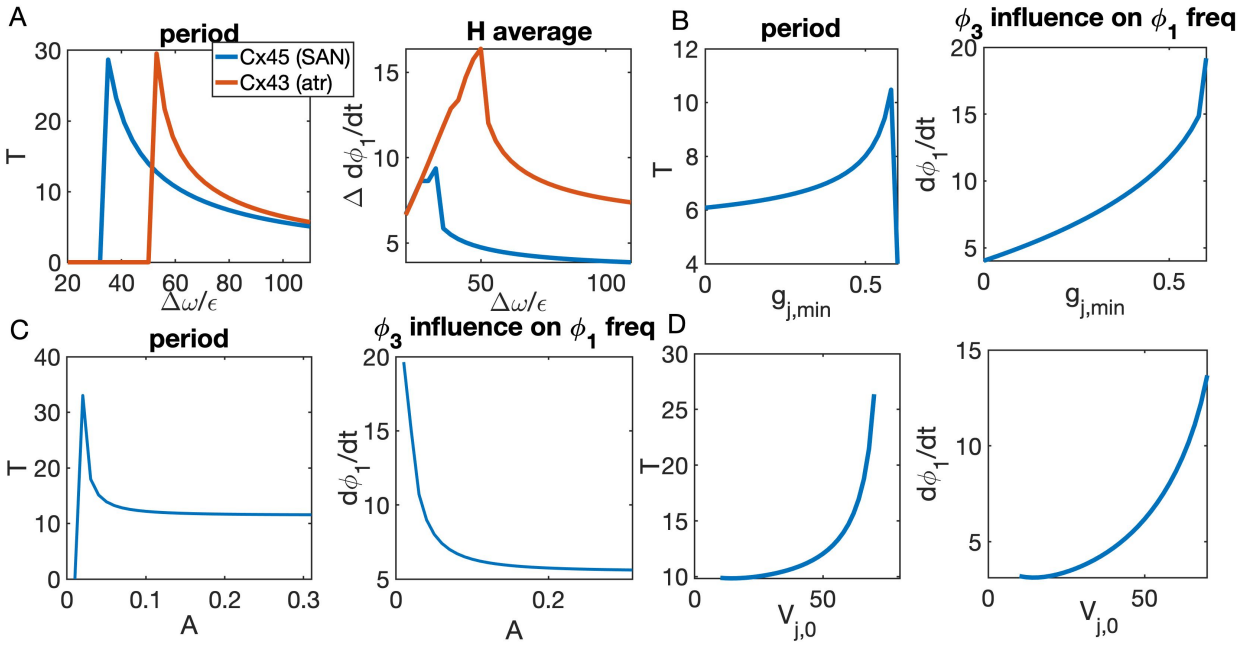

FIGURE 3.13. The frequency difference $\Delta\omega$ between one cell and a pair of identical cells influences the frequencies of the homogeneous pair. Upper left: as the frequency shift increases, the period over which the third cell makes a full orbit relative to the period of the pair decreaes. Upper right, lower left and lower right: for a fixed intermediate frequency shift $\Delta\omega = 60\epsilon$, each of the parameters defining voltage-dependent conductance influences the phase walk-through period.

as the central cell, and where ϕ_3 has the potential for a slight frequency heterogeneity $\Delta\omega$. The equations for each cell are the following:

$$\frac{d\phi_1}{d\tilde{t}} = \frac{1}{T}\int_0^T Z(t+\phi_1)\cdot I_C(V_{LC}(t+\phi_1+(\phi_2-\phi_1)), V_{LC}(t+\phi_1))dt$$

$$\frac{d\phi_2}{d\tilde{t}} = \frac{1}{T}\left(\frac{1}{2}\int_0^T Z(t+\phi_2)\cdot I_C(V_{LC}(t+\phi_2-(\phi_2-\phi_1)), V_{LC}(t+\phi_2))dt + \frac{1}{2}\int_0^T Z(t+\phi_2)\cdot I_C(V_{LC}(t+\phi_2+(\phi_3-\phi_2)), V_{LC}(t+\phi_2))dt\right)$$

$$\frac{d\phi_3}{d\tilde{t}} = \frac{1}{T}\left(\int_0^T Z(t+\phi_3)\cdot I_C(V_{LC}(t+\phi_3-(\phi_3-\phi_2)), V_{LC}(t+\phi_3))dt + \Delta\omega\right)$$

which gives rise to the differential equations for phase differences $\psi_1 = \theta_2 - \theta_1$ and $\psi_2 = \theta_3 - \theta_2$:

$$\frac{d\psi_1}{d\tilde{t}} = -H(\psi_1) + \frac{1}{2}(H(-\psi_1) + H(-\psi_2))$$
$$\frac{d\psi_2}{d\tilde{t}} = H(-\psi_2) - \frac{1}{2}(H(-\psi_2) + H(-\psi_1)) + \Delta\omega$$

As above in the all-to-all coupling scenario, we first examine the phase plane with default parameters ($g_{j,min} = 0.2$, $V_{j,0} = 50$, $A = 0.1$) to identify the steady states of the system and the overall flow of trajectories. The phase plane is shown in fig. 3.14A; nullclines are shown in blue (ψ_1) and red (ψ_2). As with all-all coupling, there is one stable equilibrium, corresponding to synchrony among the three cells. However, the unstable equilibria are slightly different between the two coupling arrangements (compare fig. 3.9A with fig. 3.14A). In fig. 3.14A, we show the phase plane and yellow and green trajectories correpsonding to initial conditions of $(0.2, 0.4)$ and $(0.4, 0.7)$. The time courses for the trajectories labeled in A are shown in fig. 3.14B and C. In the phase plane, both trajectories approach synchrony; the time-courses confirm this, as the three cells synchronize after a sufficient time interval.

As with all-all coupling, the steady states in the nearest-neighbor coupling arrangement are eliminated as the heterogeneity $\Delta\omega$ increases. In fig. 3.15A we show the phase plane with default parameters and $\Delta\omega = 23$, sufficiently large to eliminate the phase-locked steady state. There are no equilibria, evident by the absence of intersections of the red and blue nullclines in fig. 3.15A. In fig. 3.15B and C, we show the time-courses for trajectories shown in yellow (B) and green (C) in panel A. Notably, the three cells do not synchronize over time, although the pair of identical cells (cells 1 and 2) converges toward the ψ_1 nullcline.

Next, we use the phase plane to consider the effects of each voltage-dependent conductance parameter on the relationship between heterogeneity $\Delta\omega$ and the nullclines for phase differences ψ_1 and ψ_2 in a system of three coupled cells with nearest-neighbor coupling (figure 3.16). In the nearest-neighbor coupling arrangement there is one less global steady state than with all-to-all coupling. However, the qualitative results in the nearest-neighbor scenario are

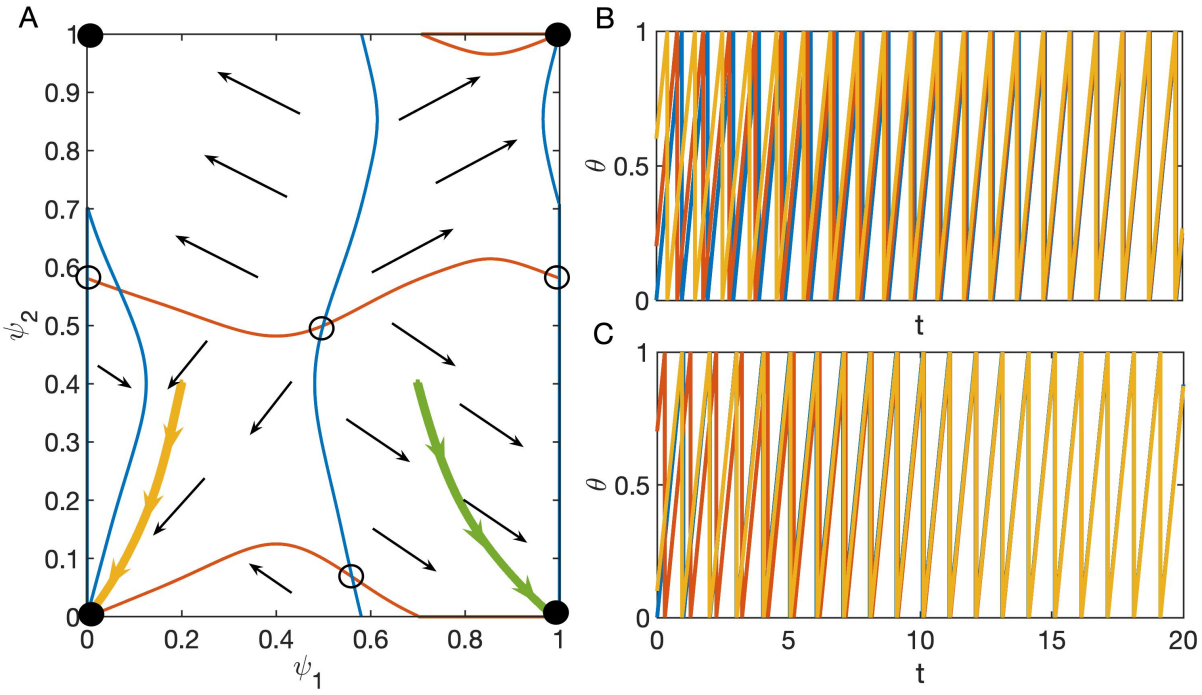

FIGURE 3.14. A: The phase plane for two phase differences $\psi_1 = \theta_2 - \theta_1$ and $\psi_2 = \theta_3 - \theta_2$ for standard parameters $g_{j,min} = 0.2$, $V_{j,0} = 0.5$, $A = 0.2$. Nullclines are shown in blue (ψ_1) and red (ψ_2). Open and filled circles indicate unstable and stable steady states. Trajectories with initial conditions $(0.2, 0.4)$, $(0.4, 0.6)$, and $(0.7, 0.4)$ are shown in yellow and green with arrowheads indicating the direction of flow (A). B: corresponding time-course for trajectory with initial condition $(0.2, 0.4)$ as shown in yellow and green trajectories in panel A. After several action potentials, all three cells synchronize. C: time-course for trajectory with initial condition $(0.7, 0.4)$, as in green trajectory in A. As in B, the three cells synchronize after a sufficient amount of time.

very similar to those in the all-to-all coupling condition. As each parameter is varied the steepness of nullclines changes slightly (fig. 3.16A-C) but the number and location of steady states remain unchanged.

Furthermore, as the parameters change, the threshold for heterogeneity $\Delta\omega_{SNB}$ at which steady states disappear via a saddle-node bifurcation changes. As in the all-all coupling case, when $g_{j,min}$ increases in the nearest-neighbor coupling network, $\Delta\omega_{SNB}$ increases (fig. 3.16D); this is expected, as increased $g_{j,min}$ increases the coupling between cells at very different voltages, acting to move cells towards synchrony. As $|V_{j,0}|$ increases, $\Delta\omega_{SNB}$ increases (fig.

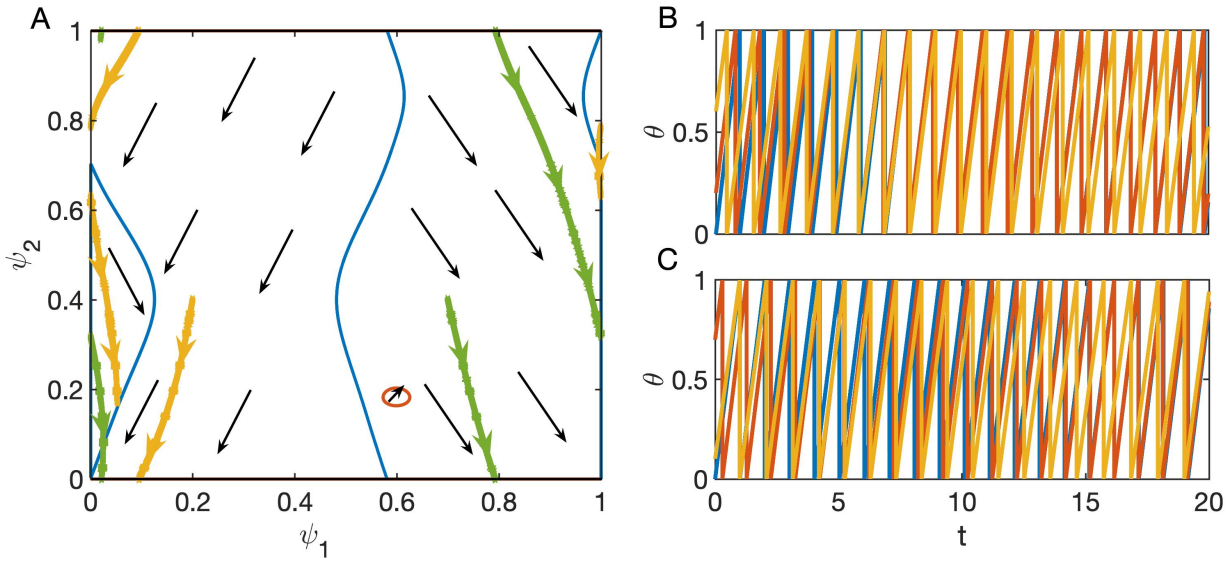

FIGURE 3.15. A: The phase plane for two phase differences $\psi_1 = \theta_2 - \theta_1$ and $\psi_2 = \theta_3 - \theta_2$ for standard parameters $g_{j,min} = 0.2$, $V_{j,0} = 0.5$, $A = 0.2$ and $\Delta\omega = 23$. Nullclines are shown in blue (ψ_1) and red (ψ_2). There are no global equilibria. Trajectories with initial conditions $(0.2, 0.4)$, $(0.4, 0.6)$, and $(0.7, 0.4)$ are shown in yellow and green with arrowheads indicating the direction of flow (A). B: corresponding time-course for trajectory with initial condition $(0.2, 0.4)$ as shown in yellow and green trajectories in panel A. After several action potentials, the cells do not synchronize. C: time-course for trajectory with initial condition $(0.7, 0.4)$, as in green trajectory in A. As in B, the three cells do not synchronize over time.

3.16E), which is also consistent with our expectations, as increased $|V_{j,0}|$ means the window of high conductance widens with respect to transjunctional potential. This broader range of high conductance also moves cells towards synchrony, and therefore increases the size of heterogeneity necessary to decouple the network. Finally, as A increases, $\Delta\omega_{SNB}$ decreases slightly (fig. 3.16F), because increased A diminishes the "tails" of the voltage dependent conductance $g_{j,ss}$, reducing the magnitude of coupling for cells at different voltages. As with all-all coupling, the robustness of phase-locking changes as the nullclines shift slightly due to changes to the gating parameters, but there is no qualitative change in behavior to the overall phase plane.

We explore the effects of gating parameters on the period of phase-walkthrough when the third "rogue" cell uncouples, and on the average effect of the third cell on the frequency

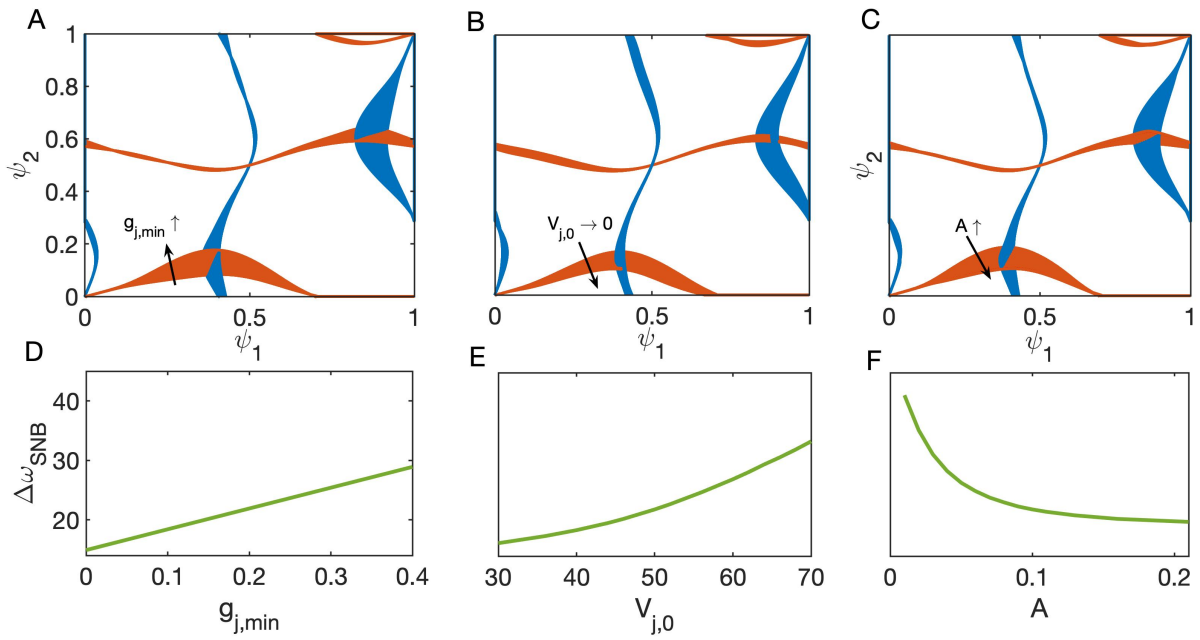

FIGURE 3.16. A-C: effects of each parameter $V_{j,0}$, $g_{j,min}$ and A on the phase plane for phase differences in a three-cell nearest-neighbor coupled system. As $g_{j,min}$ increases, the curvature of the nullclines increases, but the number of steady states remains unchanged and their locations do not change. Similarly, as $V_{j,0}$ approaches zero and as A increases, the curvature of each nullcline is reduced but the number and location of steady states remain the same. D-F: As heterogeneity $\Delta\omega$ of the third cell increases from zero, the system undergoes a saddle-node bifurcation whereby one of the steady states is abolished. The threshold $\Delta\omega_{SNB}$ changes depending on each parameter: as $g_{j,min}$ increases, $\Delta\omega_{SNB}$ increases (D); as $|V_{j,0}|$ increases, $\Delta\omega_{SNB}$ increases (E); as A increases, $\Delta\omega_{SNB}$ decreases (F).

of the two phase-locked cells, as in the all-all coupling case above, in figure 3.17. As in all-all coupling, the difference between Cx45 and Cx43 gap junctions primarily has the effect of modifying the overall strength of coupling between pairs of cells. The shapes of the relationships between each parameter and the phase walk-through period are very similar in the two different coupling arrangements. As in the all-all coupling case, there is no difference in the qualitative shape of the relationship between heterogeneity, period, and phase effect of a third cell between the two types of gap junctions.

Taken together, the results of our phase plane analysis and phase-walkthrough experiments suggest that the differences between voltage gating parameters across different types

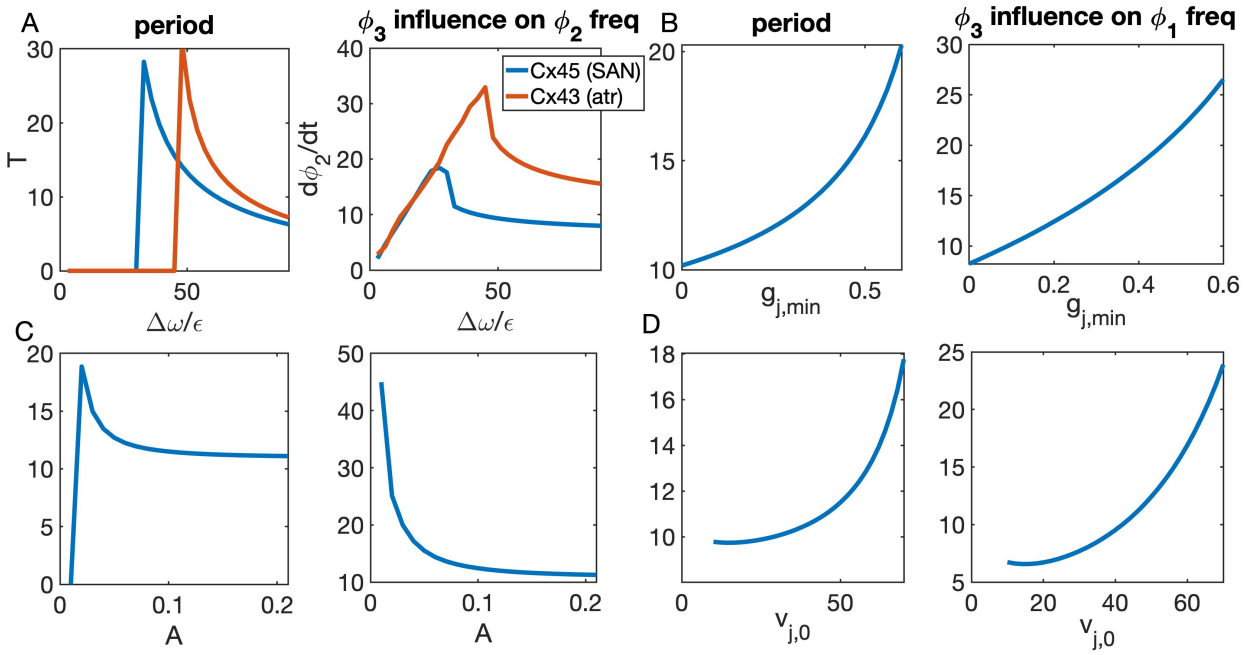

FIGURE 3.17. The frequency difference $\Delta\omega$ between one cell and a pair of identical cells influences the frequencies of the homogeneous pair. Upper left: as the frequency shift increases, the period over which the third cell makes a full orbit relative to the period of the pair decreaes. Upper right, lower left and lower right: for a fixed intermediate frequency shift $\Delta\omega = 60\epsilon$, each of the parameters defining voltage-dependent conductance influences the phase walk-through period.

of gap junction times primarily only alter the overall magnitude of conductance between the two cells, but do not fundamentally alter the dynamics of phase-locking between pairs or networks of cells.

3.4.2.3. *Three-Cell Simulations: lead site shift or synchrony shift.* The results of our phase plane analysis do not indicate a significant role of voltage dependence of gap junctional conductance on synchrony aside from reducing the overall robustness of phase-locking between cells. The sinoatrial node primarily contains Cx45 gap junctions, which have steeper voltage-dependence and lower overall conductance as compared with Cx43 gap junctions, which are present in higher concentrations in the atrium and myocardium. We explore the effects of voltage dependence by simulating systems of two and three oscillators coupled by

Cx43 and Cx45 gap junctions, under varying conditions that induce a shift in lead site or a shift in the frequency of synchronized cells.

In figure 3.18, we simulate two cells – each reduced to a phase model – coupled by Cx43 and Cx45 gap junctions. We change the intrinsic frequency of cell 2 linearly over an interval of $t = 100$ from $\approx 10\%$ faster than cell 1 to $\approx 10\%$ slower than cell 1, mimicking an experiment reducing sympathetic tone or increasing parasympathetic tone to cell 2 (fig. 3.18A). Cells 1 and 2 begin in synchrony at $t = 0$, but diverge as the higher frequency of cell 2 drives the stable phase-locked state away from synchrony (fig. 3.18B). At $t = 50$, the frequency of cell 2 is lower than that of cell 1; however, the phase shift remains positive, i.e., cell 2 stays the lead pacing cell, until $t = 54$. In both cases, the lead site shifts from cell 2 to cell 1 at $t \approx 54$, at which cell 1 becomes the leading pacemaker (fig. 3.18B). After $t \approx 80$, the cells desynchronize again, and phase shift oscillates for both Cx45 and Cx43 gap junctions. In Cx45 gap junctions, the two cells are phase-locked for a shorter range of time (from $t \approx 25$ to $t \approx 75$) than for Cx43 gap junctions ((from $t \approx 5$ to $t \approx 75$). Most importantly, however, fig. 3.18 demonstrates that the voltage-dependence parameters that distinguish Cx43 from Cx45 gap junctions do not affect the qualitative process of lead pacemaker shift in a pair of two coupled cells.

In figure 3.19, we expand the system to three cells coupled in a nearest-neighbor arrangement by Cx43 and Cx45 gap junctions. We simulate the process of a gradual reduction in sympathetic tone or an increase in parasympathetic tone, wherein cells 1 and 2 remain identical and at constant frequency throughout the simulation but the intrinsic frequency of cell 3 changes over a period of $t = 100$ from $\approx 5\%$ faster than the cell 1-cell 2 pair to $\approx 5\%$ slower than the pair (fig. 3.19A). In fig. 3.19B, red curves depict the phase difference between cells 3 and 2, while blue curves depict the phase difference between cells 2 and 1. Solid lines represent cells coupled with Cx45 gap junctions, whereas dashed lines represent cells coupled with Cx43 gap junctions. Cells begin in synchrony at $t = 0$, but quickly shift to a 1:1 phase-locked state. From $t = 0$ until $t \approx 54$, in both cases, $\Delta\phi_{32} > \Delta\phi_{21} > 0$,

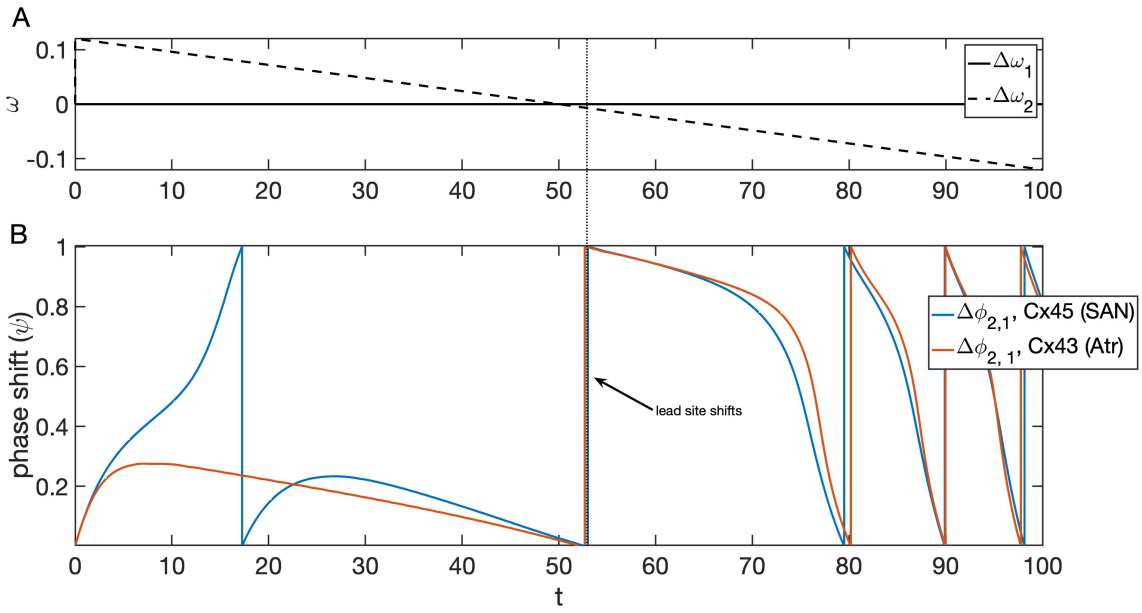

FIGURE 3.18. Two cells coupled by Cx43 and Cx45 gap junctions. A: frequency of cell 1 remains constant over the simulation; the intrinsic frequency of cell 2 changes over a period of $t = 100$ from slightly faster than cell 1 to slightly slower than cell 1. B: red curve depicts the phase difference between two cells coupled by Cx43 gap junctions, while the blue curve depicts the phase difference between two cells coupled by Cx45 gap junctions. In both cases, lead site shift occurs at $t \approx 54$, but this change occurs more abruptly in the Cx45-coupled system than in the Cx43-coupled system.

indicating that cell 3 is the "leader" and that cell 2 leads cell 1. Lead site shifts from cell 3 to cell 2 at $t \approx 54$, when $\Delta\phi_{32}$ crosses zero but $\Delta\phi_{2,1}$ remains positive. Lead site then shifts again from cell 2 to cell 1 at $t \approx 60$, as $\Delta\phi_{2,1}$ crosses zero. Almost no difference can be detected between the overall behavior of the three-cell system in the two different coupling schemes, indicating that the differences in voltage-dependent gating between Cx43 and Cx45 gap junctions do not impact the qualitative process of lead site shift in a network of three cells.

Finally, in fig. 3.20, we simulate the case in which one intermediate cell or region receives input from the sympathetic nervous system that increases the frequency of firing in that region over a period of time, such that the intermediate region switches from phase-locking with a slower region to phase-locking with a faster region. Cells 1 and 3 maintain constant

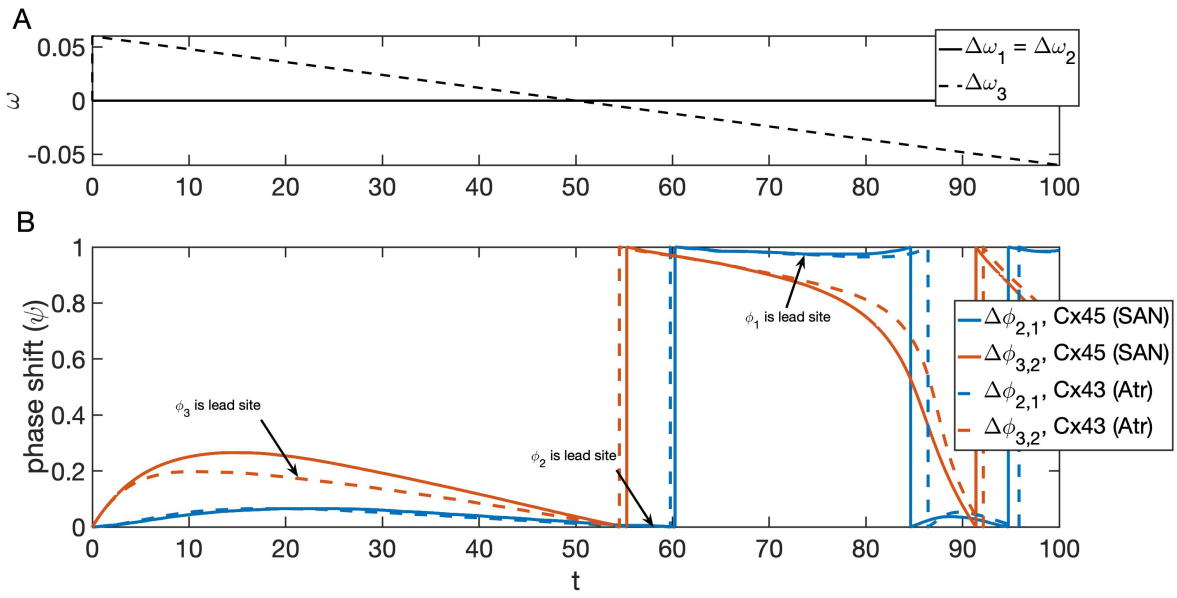

FIGURE 3.19. As in figure 3.18, but here we expand the system to three cells coupled in a nearest-neighbor arrangement by Cx43 and Cx45 gap junctions. A: cells 1 and 2 remain identical and at constant frequency throughout the simulation; the intrinsic frequency of cell 3 changes over a period of $t = 100$ from slightly faster than the cell 1-cell 2 pair to slightly slower than the pair. B red curves depict the phase difference between cells 3 and 2, while blue curves depict the phase difference between cells 2 and 1. Solid lines represent cells coupled with Cx45 gap junctions, whereas dashed lines represent cells coupled with Cx43 gap junctions. In both cases, lead site shifts from cell 3 to cell 2 at $t \approx 54$ and then shifts from cell 2 to cell 1 at $t \approx 60$, and subsequently vacillates between cells 1 and 2.

frequencies, where cell 3 oscillates $\approx 10\%$ faster than cell 1. We transition cell 2 from the frequency of cell 1 to the frequency of cell 3 over an interval of $t = 100$ (fig. 3.20A). With both Cx43 and Cx45 gap junctions, cells 1 and 2 are phase-locked at first (until $t \approx 50$ for Cx45 gap junctions and $t \approx 70$ for Cx43 gap junctions), but the phase difference between cells 1 and 2 gradually increases as the frequency of cell 2 increases. After desynchronizing from cell 1, cell 2 ultimately phase-locks with cell 3, which occurs earlier with Cx 43 gap junctions ($t \approx 30$) than in Cx45 gap junctions ($t \approx 70$). The difference in transition times is such that with Cx43 coupling there is a time interval over which all three cells are phase-locked (fig. 3.20B, from $t \approx 30$ to $t \approx 70$). This suggests that Cx45 gap junctional coupling in the SAN may force separate regions of the SAN oscillating at distinct frequencies to

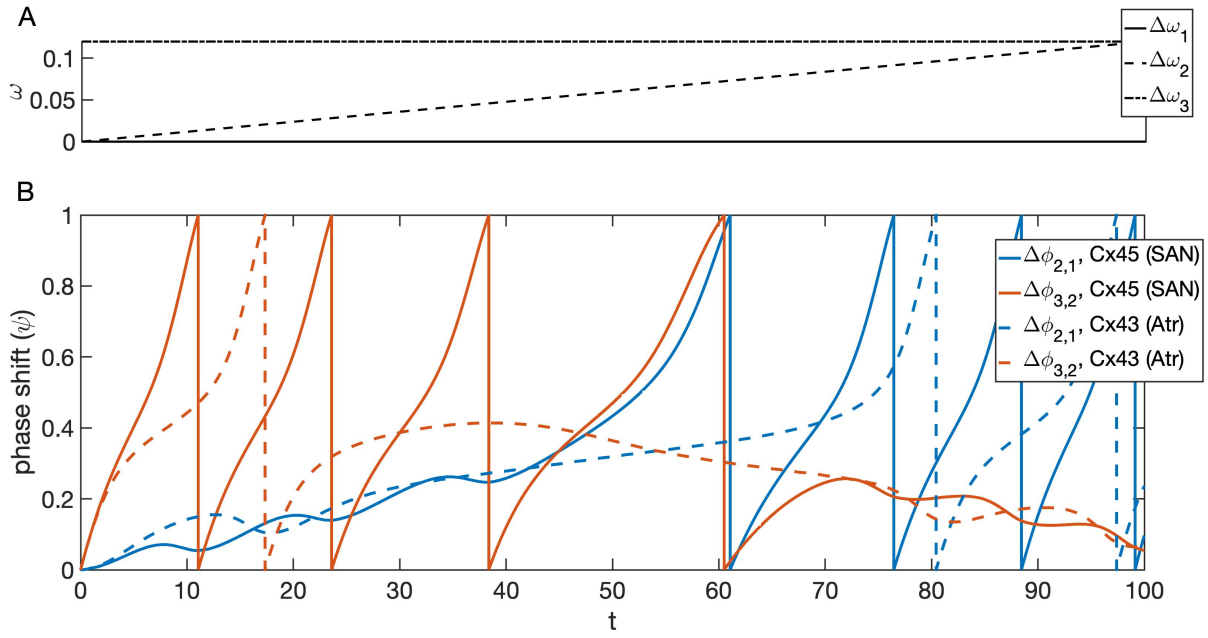

FIGURE 3.20. Three cells coupled in a nearest-neighbor arrangement by Cx43 and Cx45 gap junctions. A: cells 1 and 3 remain at constant frequency throughout the simulation, with cell 3 oscillating faster than cell 1. The intrinsic frequency of cell 2 changes over a period of $t = 100$ from identical to cell 1 to identical to cell 3. B: red curves depict the phase difference between cells 3 and 2, while blue curves depict the phase difference between cells 2 and 1. Solid lines represent cells coupled with Cx45 gap junctions, whereas dashed lines represent cells coupled with Cx43 gap junctions. In both cases, cell 2 switches from synchronized with cell 1 to synchronized with cell 3. However, this shift occurs more rapidly in Cx45-coupled cells than in Cx43-coupled cells, reducing the time interval over which all three cells are phase-locked. In Cx45-coupled cells, the three cells exhibit phase-locking between $t \approx 40$ and $t \approx 61$, while in Cx43-coupled cells, the three cells exhibit phase-locking between $t \approx 20$ and $t \approx 70$.

avoid phase-locking, whereas Cx43 gap junctions allow for cells at disparate frequencies to phase-lock.

3.4.3. Two Cells with Time-Dependent Voltage Gating. As suggested by Desplantez [**19**], the dependence of gap junction conductance on junctional potential is in fact not instantaneous but develops over time. Fig. 3.1 suggests that voltage dependence develops on a time scale comparable to or slower than the cells' intrinsic action potential; this suggests that the combined voltage dependence and time dependence of coupling may give rise to more

complex dynamics than can be observed by studying the instantaneous voltage-dependent system. Therefore, in order to find any potential effects of time-dependent coupling, we extend the theory of weakly coupled oscillators to allow for conductance to develop on a slow time-scale commensurate with changes to phase shift due to coupling. We augment the system, as derived in section 3.2.1 to include a differential equation for gap junctional conductance g_c. The assumption that g_c develops over a slower time-scale than the period of intrinsic cellular implies that g_c can be approximated by the average conductance over a phase of oscillations. This generates the following system of differential equations for ψ, the phase difference between two cells, and g_c, the conductance across gap junctions coupling the two cells:

$$\frac{d\psi}{dt} = \frac{1}{T}\int_0^T z(\tau)[g_c(V_j) * (V_{LC}(\tau+\psi) - V_{LC}(\tau)]d\tau$$
$$\frac{dg_c}{dt} = \frac{1}{\tau_c}\left[\frac{1}{T}\int_0^T g_{j,\infty}(V(\tau))d\tau - g_c\right]$$

We consider the two parameter sets for $g_{j,ss}(\Delta V)$ corresponding to Cx43 and Cx45 gap junctions as reported in [**19**] (Table 3.1), and vary the magnitude of frequency difference between the two cells. Plotting the nullcline for g_c, also referred to as $g_{c,\infty}$ and the nullclines for ψ generates the phase plane in figure 3.21. The $g_{c,\infty}$ curves for Cx43 and Cx45 gap junctions are qualitatively similar: both steady-state conductances are at 1 for synchronous cells, and dip symmetrically as the phase difference increases. The Cx45 $g_{c,\infty}$ nullcline dips lower than does the Cx43 $g_{c,\infty}$ nullcline around antiphase. When $\Delta\omega = 0$, the ψ nullcline consists of two vertical lines at zero (synchrony) and 0.5 (antiphase), resulting in a stable steady state at synchrony and an unstable steady state at antiphase for both Cx43 and Cx45 gap junctions. The steady-state conductance at the unstable equilibrium at antiphase is slightly higher for Cx43 gap junctions than for Cx45 gap junctions. As heterogeneity $\Delta\omega$ increases, the ψ nullcline shifts upward, moving the two steady states. The stable steady state at synchrony shifts in the positive direction, while the unstable steady state at antiphase

shifts in the negative direction. As the steady states shift, the steady-state conductance at the stable equilibrium point decreases, following the $g_{c,\infty}$ nullclines for either Cx43 or Cx45. As heterogeneity is further increased, both steady states come together and disappear in a saddle-node bifurcation (SNB). The SNB occurs at higher heterogeneity for Cx43 gap junctions ($\Delta\omega$ between 30 and 40) than for Cx45 gap junctions ($\Delta\omega$ between 20 and 30) due to the higher g_c nullcline. Note that in the constant-conductance case, the SNB occurs at $\Delta\omega$ between 40 and 50. Notably, because the stable and unstable steady states remain close to synchrony and antiphase respectively for the time- and voltage-dependent systems, the time-dependence of voltage-dependent conductance does not qualitatively change the properties of the 1:1 phase-locking in the system. Moreover, considering time-dependent voltage gating does not illuminate any underlying qualitative differences between Cx45 and Cx43 gap junctions.

The time-dependence of gap junctional voltage gating does not provide additional evidence for the specific role of different gap junctions in different regions of the heart. As in our studies of instantaneous voltage-dependent gating, we do not see any evidence that the voltage-gated conductance differences between Cx43 and Cx45 gap junctions contribute to qualitative differences in synchrony and phase-locking properties in small networks of cells in the heart.

3.5. Discussion

In our analysis of symmetrically coupled pairs of cells, the parameters that define voltage-dependent gap junctional conductance affect the average conductance across gap junctions over the cardiac cycle, but do not qualitatively change the phase-locking properties of a coupled system. Since cell-to-cell coupling always acts as a synchronizing force, we expect that gap junctions with lower conductance between cells will destabilize synchrony, and our results are consistent with this expectation. In all simulations with homogeneous cells, there is one stable steady state at synchrony and one unstable steady state at antiphase. As heterogeneity increases, the two steady states approach each other and annihilate in a

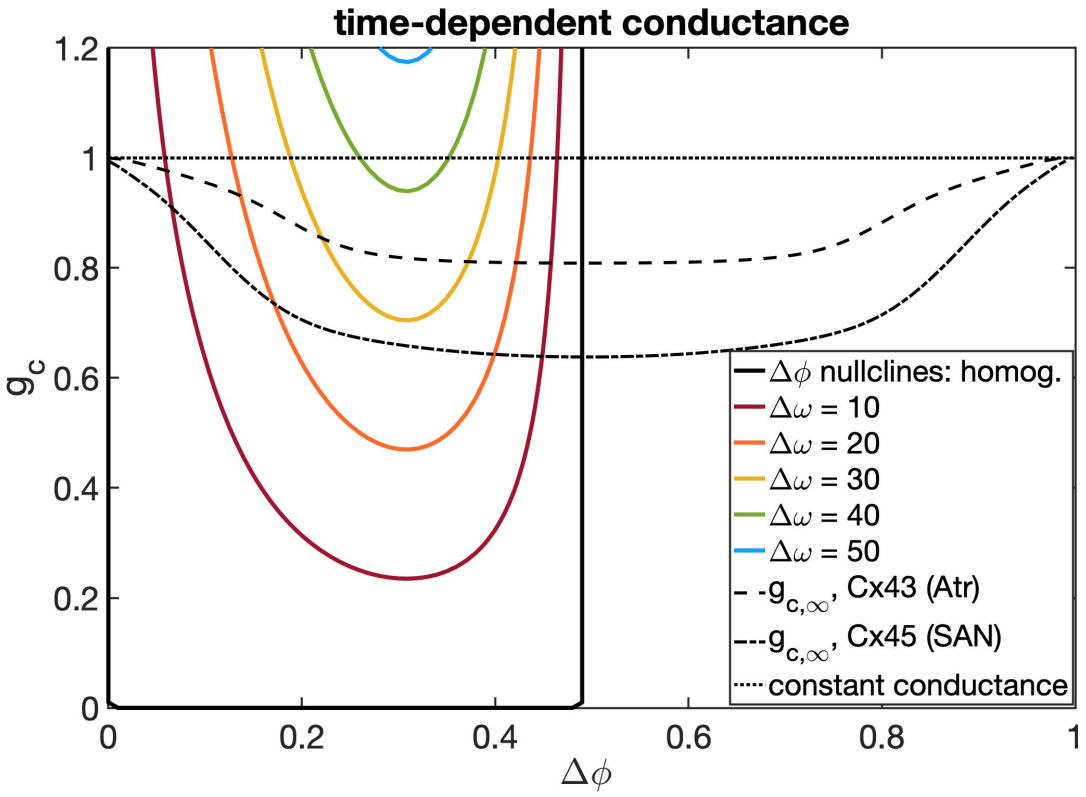

FIGURE 3.21. Phase plane for a system of two cells coupled by Cx43 and Cx45 gap junctions, with slowly developing voltage dependence of conductance. We plot the nullclines of conductance g_c corresponding to each gap junction type, and of phase difference ψ for various magnitudes of frequency difference $\Delta\omega$ between the two cells.

saddle-node bifurcation. Each of the measures of robustness of synchrony to heterogeneity in a two-cell pair depends monotonically on each of the three parameters $g_{j,min}$, $V_{j,0}$, and A, with one small exception for very low A. Over the majority of parameter space, robustness increases with increased $g_{j,min}$, increased $|V_{j,0}|$, and decreased A. For very low A, the stability of synchrony measured by $|G'(0)|$ decreases with increased A; however, this non-monotonicity has a minimal effect on overall behavior. Based on the monotonic dependence of robustness on each parameter and the fact that Cx45 gap junctions have lower $g_{j,min}$, lower $|V_{j,0}|$, and similar values of A compared to Cx43 gap junctions, we expect two-cell pairs coupled with parameters corresponding to Cx45 gap junctions to display lower robustness to heterogeneity than pairs coupled by parameters corresponding to Cx43 gap junctions with similar coupling

strength at $\Delta V = 0$. However, the existence and stability of 1:1 phase-locked steady states do not change qualitatively with changes in voltage-gating parameters.

Similarly, in our analysis of the effects of each gating parameter on the cross-correlogram $\rho(\psi)$, the stability of synchrony and instability of antiphase both increase with increased $g_{j,min}$, increased $|V_{j,0}|$, and decreased A. Therefore, we expect synchrony in cell pairs coupled by Cx45 gap junctions to exhibit less robustness to random noise than does synchrony in pairs coupled by Cx43 gap junctions.

Our analysis of systems of three cells – both in all-all and nearest-neighbor coupling arrangements – provides similar predictions regarding the robustness of phase-locking to heterogeneity as in pairs of cells. The existence, number, and stability of 1:1 phase-locked steady states in the symmetrically coupled, homogeneous system do not change depending on voltage-gating parameters. However, the robustness to heterogeneity of the single stable steady state, as measured by $\Delta\omega_{SNB}$, the magnitude of heterogeneity required to desynchronize a single cell from an identical pair, depends monotonically on each gating parameter. As in the two-cell system, robustness increases with increased $g_{j,min}$, increased $|V_{j,0}|$, and decreased A. Thus, we expect systems of three cells coupled by Cx43 gap junctions to exhibit lower overall robustness to heterogeneity than those coupled with Cx45 gap junctions, but we do not expect fundamental differences in phase-locking dynamics. Moreover, we expect the results of the three-cell system to extend to larger networks of cells; we predict that the differences in voltage-dependent gating between different gap junctions impact the robustness of a network of cells to heterogeneity, but do not qualitatively alter the phase-locking properties.

Results from the extension of the theory of weakly coupled oscillators to slow, time-dependent voltage-dependent gating align with the findings of our instantaneous voltage-gating analysis. In pairs of cells coupled with time-dependent gap junctions, slow gating reduces the conductance when the phase difference is not close to zero. However, there remains one stable steady state at synchrony and one unstable steady state at antiphase;

as heterogeneity increases, the two steady states approach each other and annihilate in a saddle-node bifurcation, as in the instantaneous voltage-gated coupling system. A pair of cells coupled by Cx45 gap junctions exhibits lower coupling conductance than the same pair coupled by Cx43 gap junctions at every phase difference except synchrony, which is also predicted by the instantaneous voltage-gating analysis. The extention to time-dependent gating does not seem to give rise to any further complexity in the properties of synchrony and phase-locking in a pair of cells.

It has been argued that coupling in the SAN must be weaker overall than in the surrounding atrium in order to maintain electrical insulation of the SAN [**9**, **18**]. This is consistent with the lower conduction velocity in the SAN than in the atria and ventricles [**18**]. Based on the differences in single-channel conductance between Cx45 and Cx43 gap junctions, the sinoatrial node is expected to have less cell-to-cell current coupling per gap junction channel than the atrium. The fact that there are also fewer total gap junctions in the SAN than in the working myocardium further reduces the conductance in the SAN relative to the atria and ventricles [**18**]. Voltage-dependence of gap junctions may provide a more effective measure to insulate the SAN, by reducing the electronic influence of atrial cells on SAN cells. However, given the reduced overall number of gap junctions throughout the SAN and lower single-channel conductance of Cx45 gap junctions, the argument for reduced overall electrical coupling in the SAN compared with the atria and ventricles does not necessarily provide further justification for the importance of the voltage-dependent coupling of Cx45 gap junctions.

It may be that the arrangement of Cx43 and Cx45 in the SAN and surrounding tissue affects cardiac conduction via mechanisms more complex than can be accounted for in a small network of cells with symmetric coupling. Some evidence indicates that the presence of an "intermediate" region immediately surrounding the SAN, possibly containing both Cx45 and Cx43 gap junctions and/or heterotypic Cx45-Cx43 gap junctions, is important to achieving the balance between electrical source strength and insulation necessary for the SAN to pace

the myocardium [**34**]. Indeed, such a "peripheral" region has been identified in which both Cx43 and Cx45 are expressed [**9**,**18**]. Heterotypic gap junctions composed of both Cx43 and Cx45 have been shown to exhibit asymmetric voltage dependence [**55**]. Future modeling work should extend the present efforts by considering the role of asymmetric coupling on phase locking in SAN cells.

It is also possible that there are functionally distinctive characteristics of Cx43 and Cx45 gap junctions that make each more suitable for different regions of the heart, but which are beyond the scope of our modeling approach. For instance, Cx43 and Cx45 may be differentially modulated by biochemical and physiological factors. While both Cx43 and Cx45 gap junctions exhibit reduced coupling in the presence of low intracellular pH [**39**,**67**], the two may respond in opposite directions to the presence of cyclic AMP (cAMP) and subsequent phosphorylation by protein kinase A (PKA). Experiments have suggested that Cx43 gap junctions increase their coupling in the presence of PKA, while Cx45 gap junctions decrease their coupling [**39**, **67**]. Given that the sympathetic nervous system modulates heart rate via intracellular cAMP-PKA signaling in the sinoatrial node, the response of gap junctions to PKA could be highly relevant to the distinguishing features of the SAN.

Finally, the distribution and relative abundance of Cx40, Cx43 and Cx45 gap junctions changes in end-stage congestive heart failure [**18**]. In particular, the proportion of Cx43 relative to Cx45 decreases. The mechanisms and consequences of these adaptations in pathology may provide insight into the general distribution and function of different types of gap junctions in the healthy system. It is therefore of interest to further examine the changes that occur in chronic heart failure and to consider how the shifting proportions of connexin isoforms might have either cardioprotective or harmful consequences.

3.6. Appendix: Guevara SAN cell model

The three-variable ionic model for sinoatrial node cells by Guevara [**26**] includes variables for membrane potential (V), inactivation gate for the slow inward current I_s (f), and potassium channel activation (p):

$$\frac{dV}{dt} = -d_\infty f(V)\bar{i}_S(V) - p(V)\bar{i}_K(V) - I_L(V) + I_{app}$$
$$\frac{df}{dt} = \alpha_f(V)(1-f) - \beta_f(V)f$$
$$\frac{dp}{dt} = \alpha_p(V)(1-p) - \beta_p(V)p$$

with currents, parameters, α_x and β_x functions defined as follows:

- Slow inward current I_S is given by

$$I_S = d_\infty \cdot f(V)\bar{i}_S(V)$$

with activation current d_∞ defined as

$$d_\infty = \frac{\alpha_d}{\alpha_d + \beta_d}$$

where

$$\alpha_d(V) = \frac{1.2}{1+\exp(-V/12)}$$
$$\beta_d(V) = \frac{0.25}{1+\exp((V+30)/8)}.$$

The inactivation gate $f(V)$ is governed by the differential equation

$$f(V) = -\frac{1}{\tau_f}(f - f_\infty)$$

where

$$f_\infty = \frac{\alpha_f}{\alpha_f + \beta_f}$$
$$\tau_f = \frac{1}{\alpha_f + \beta_f}$$

and $\alpha_f(V)$, $\beta_f(V)$ are given by

$$\alpha_f(V) = 7 \times 10^{-4} \frac{V + 45}{\exp((V + 45)/9.5) - 1}$$
$$\beta_f(V) = \frac{0.036}{1 + \exp(-(V + 21)/9.5)}.$$

Maximal current $\bar{i}_S$ is given by

$$\bar{i}_S = 15(\exp((V - 40)/25) - 1).$$

- Potassium current I_K is given by

$$I_K = p(V)\bar{i}_K(V)$$

with activation current $p(V)$ defined by

$$p(V) = -\frac{1}{\tau_p}(p - p_\infty)$$

and τ_p, p_∞ given by

$$p_\infty = \frac{\alpha_p}{\alpha_p + \beta_p}$$
$$\tau_p = \frac{1}{\alpha_p + \beta_p}$$

with α_p, β_p given by

$$\alpha_p(V) = \frac{8 \times 10^{-3}}{1 + \exp(-(V + 4)/13)}$$
$$\beta_p(V) = 1.7 \times 10^{-4} \frac{V + 40}{\exp((V + 40)/13.3) - 1}.$$

Maximal current $\bar{i}_K$ is defined as

$$\bar{i}_K = 0.91 \frac{\exp(0.0277(V+90)) - 1}{\exp(0.0277(V+40))}.$$

- Leak current I_l is defined by

$$I_l = 1.2(1 - \exp(-(V+60)/25)) + \frac{0.15(V-2)}{1 - \exp(-(V-2)/5)}.$$

CHAPTER 4

Relationships between geometry, excitability, and pacemaking properties in an oscillatory or ischemic region of excitable tissue

4.1. Introduction

The sinoatrial node (SAN) fires periodic action potentials that spread into the atrium and signal muscle cells to contract, thereby initiating the beating of the heart. The interplay between competing demands of robustness of pacemaking and flexibility of frequency requires the SAN to balance electrical conductivity with insulation from the surrounding atrium, so that action potential signals can propagate outward without decaying.

The crescent-like shape of the sinoatrial node may play a role in balancing the demands for conductivity and insulation. While action potentials consistently originate in and around the central area of the SAN, the precise location of first activation shifts along the superior-inferior axis of the node as the frequency of oscillations changes [**3**,**8**]. These action potentials propagate outward in electrical waves that travel in a particular direction. There appear to be a small number of discrete "exit sites" through which action potential waves travel from the SAN into the surrounding atrial tissue [**21**, **44**, **58**]. Nodal cells are contained within a matrix of connective tissue, and it is unclear the degree to which the nodal cells are coupled to atrial cells [**46**]. Moreover, the node contains extensions that interdigitate with the surrounding atrial tissue, and in humans the presence of such extensions varies by individual [**58**]. Therefore, it is plausible that the limited number of exit pathways from the SAN may be due to emergent properties of the physiology and geometry of the SAN [**46**,**68**]. Given that the function of the SAN is critical in controlling cardiac rhythmicity and therefore is essential to the survival and health of the organism, it is important to understand how the

electrophysiological properties of the node interact with its complex geometry to influence cardiac conduction.

Beyond the setting of the SA node, ischemia or infarction can cause a region of tissue in the myocardium to become spontaneously active and to produce electrical waves [**27**, **61**]. The resulting ectopic beats constitute dangerous and often fatal arrhythmias. In recent years, significant mathematical and computational effort has been made to model the behavior and particularly the direction of propagation of such arrhythmias [**1**, **50**, **71**]. These models have enormous potential for patient-specific medicine, as they enable clinicians to ablate localized regions of the heart in a targeted manner in order to stop the ectopic waves [**11**, **54**]. The models used in such studies are highly complex and can reproduce the behavior of ectopic beats with a high degree of accuracy. In the present work, by using a much simpler model and exploring a wide range of parameters, we focus instead on the fundamental theoretical underpinnings that determine the relationship between the size and shape of an ischemic or spontaneously active region and its propensity to generate rhythmic action potential waves.

There is reason to expect that the geometry and curvature of an ischemic or oscillating region of cardiac tissue should influence its pacing properties. Throughout the heart, a number of mechanisms exist –including the geometry and tissue structure of the SA node – that are thought to maintain a precise balance between areas of electrical "source" and "sink", i.e., regions that generate electrical current and regions to which current diffuses [**48**, **72**]. Conventional understanding suggests that electrical waves propagate more rapidly from stronger "source" regions, which includes regions of higher negative curvature, due to their higher area and therefore greater quantity of current as compared with regions of positive curvature, which are effectively smaller in comparison with surrounding excitable media [**66**]. Recent work, however, using both *in vitro* experiments on neonatal rat ventricular myocyte monolayers and a combination of mathematical analysis and computational simulation, contradicts this argument, suggesting that positive curvature may *increase* the propensity for a source to produce periodic waves [**69**]. This extends the work in [**35**], which established a

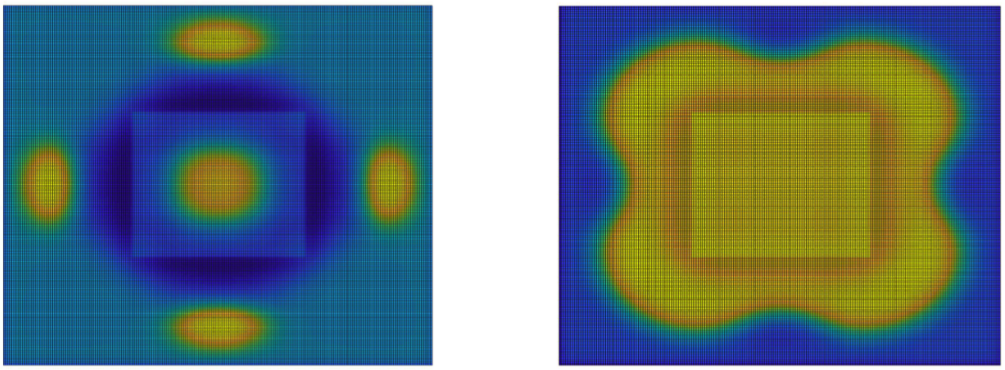

FIGURE 4.1. For $\alpha_{exc} = 0.25$, waves alternate between arising from the edges (left) and the corners (right). Waves initiating at the edges decay as they propagate away from the oscillatory region. Waves initiated at the corners propagate successfully from the oscillatory region throughout the tissue.

theoretical mechanism for the onset of oscillations from a pacemaking region through a cable of excitable tissue. In particular, [**69**] takes into account curvature in the domain, arguing that an ischemic region with sharp corners may be more likely to generate propagating electrical waves from the corners than from the edges. While the result in [**69**] is surprising, it generates important questions regarding the factors that modulate the relationship between geometry, current density, and coupling strength between the SAN – or any spontaneously active region – and surrounding myocardial tissue, and the frequency and robustness of propagating action potentials. Here, we use a combination of analysis and simulation of ordinary and partial differential equation models in an effort to explain and contextualize the result from [**69**], and to provide further insight to the role that the geometry of the SAN, or of an ischemic region, plays in governing current conduction in cardiac pacemaking.

Preliminary simulations of a square, oscillatory region surrounded by an excitable domain suggest that in some cases, waves may propagate from the corners of an oscillatory region (figure 4.1. However, we observe more complex behavior: between the threshold for global oscillations and the threshold for global 1:1 action potentials we observe a corner-edge alternating phenomenon wherein a wave propagating from the edges of the oscillatory region

that decays rapidly is followed by a wave propagating from the corners of the oscillatory region that does not decay (figure 4.1). The majority of the atrial tissue therefore fires action potentials in a 1:2 pattern with the SAN, that is, every other time the SAN fires.

We are interested in understanding the mathematical principles behind this spatially heterogeneous period-doubling behavior, which holds not only for square SAN but also for a triangular and a round SAN (data not shown). However, a rigorous analysis of the PDE in two spatial dimensions is not feasible; thus, we use numerical simulations of a 1-D, two-domain system to gain intuition, and then study the analogous system in zero dimensions (two coupled cells, representing atrial and SAN or ischemic tissue) and in one spatial dimension for more rigorous insight into these simplified systems.

4.2. General Approach: FitzHugh-Nagumo model

We use the FitzHugh-Nagumo (FHN) model, an idealized mathematical model for excitable dynamics, to simulate and analyze the threshold behavior of an oscillatory or bistable region pacing an excitable region of tissue. We aim to examine the relationship between size and curvature, electrophysiological properties of an ischemic region, and the propensity for ectopic pacing, as well as to place the counterintuitive results in [**69**] in a broader theoretical context. We address these objectives by augmenting the FHN model, as described below, as a partial differential equation in one spatial dimension and as a system of ordinary differential equations with two coupled cells, one of which is excitable and the other is oscillatory or bistable.

4.2.1. Single-Cell FHN System. The single-cell FHN ordinary differential equation contains two differential equations for variables which we define as v and w, where v represents a voltage variable whose derivative is defined by a coarse-grained sum of ionic membrane currents and w represents a refractory gating variable, akin to a potassium current:

$$\frac{dv}{dt} = f(v) - w$$
$$\frac{dw}{dt} = \epsilon(v - \gamma w - \alpha)$$

where $f(v) = -v(v-1)(v-a)$, with $a < 0.5$. We fix $a = 0.13$ throughout. Generally, the function f can be replaced by any appropriately shaped "cubic-like" function, i.e., decreasing for small and large v and increasing for intermediate v, with roots at $v = 0, 1$ and an intermediate value. The parameters α and γ are analogous to combined parameters resulting from conductances and equilibrium potentials for ionic currents in an electrophysiological model; in the general FHN model changes to α and γ can model changes in cellular excitability due to different cell types, ischemia, or input from the autonomic nervous system.

The single-cell, two-dimensional ODE allows for several possible scenarios (see fig. 4.2), depending on parameters α and γ, whose values determine the location of the steady state(s) relative to the v nullcline, and hence determine the behavior of the system. See fig. 4.2 for the bifurcation structure and intrinsic frequency of the single-cell system. When α and γ are both small, the v and w nullclines have one intersection where v is less than its value at the local minimum of $f(v)$ (blue line in fig. 4.2A); in this case the system is "excitable," meaning that a stimulus higher than a certain threshold results in an action potential after which the system returns to its steady state. As γ increases, the w nullcline becomes flatter. When γ is sufficiently large that the w nullcline intersects the v nullcline three times, the system is bistable (red line in fig. 4.2A). The parameter α adds a negative vertical shift to the w nullcline. When α is sufficiently large and γ is small, there is one intersection between the two nullclines in the portion of the v nullcline $f(v)$ where f is increasing (yellow line in fig. 4.2A); this results in an oscillatory system with an unstable steady state and a stable limit cycle. However, when α and/or γ are sufficiently high, there is only one depolarized steady state which occurs for $v \approx 1$ (green line in fig. 4.2A). These scenarios can be visualized in the phase plane (fig. 4.2A) and are summarized over a range of parameters in fig. 4.2D.

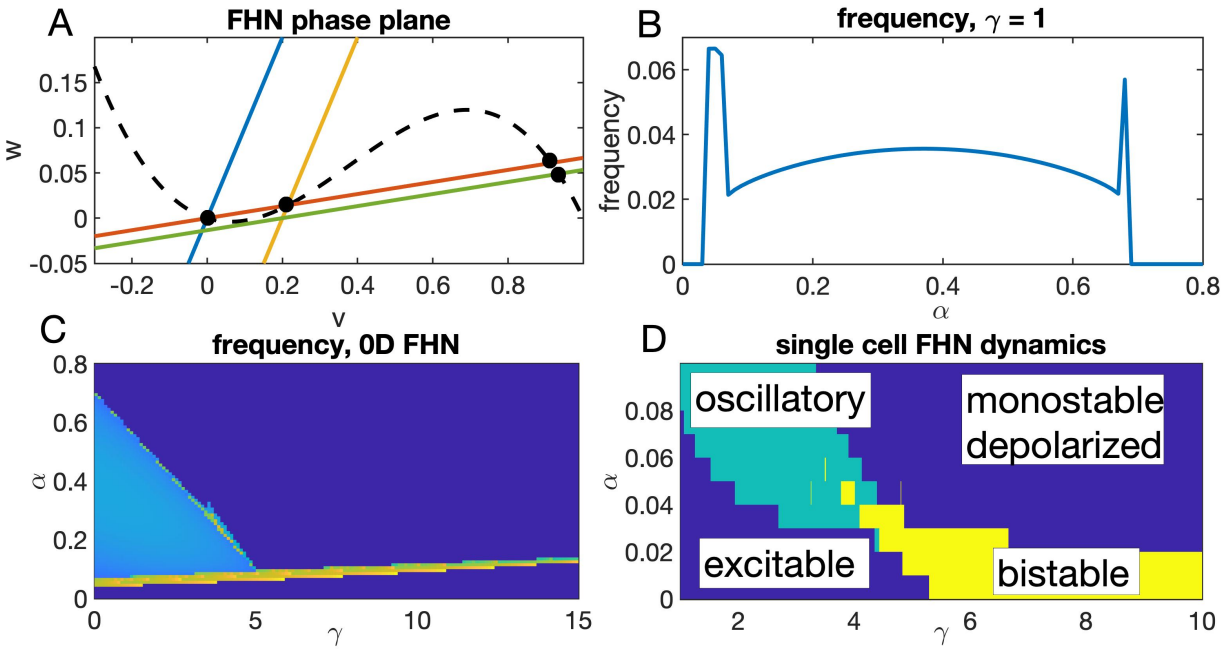

FIGURE 4.2. Behavior of the single-cell FHN system. A: for fixed $\gamma = 1$, as α changes, the rest state loses stability as the system undergoes a Hopf-like bifurcation to become oscillatory. At the onset of oscillations ($\alpha \approx 0.06$), the oscillations are subthreshold, but as α increases the oscillations become large enough to trigger action potentials, and the frequency immediately decreases. B: the frequency of the intrinsic oscillations starts at 0.06 at the onset of oscillations where $\alpha \approx 0.04$, immediately decreases to $\sim$0.03, and peaks again around $\alpha \approx 0.68$ before oscillations cease. C dependence of intrinsic frequency on γ and α in the single cell model. D: two-parameter diagram showing regions of excitable, bistable, oscillatory, and monostable depolarized behavior in the single-cell system depending on γ and α.

4.2.2. Spatially extended FHN system. The FHN partial differential equation contains the same variables v and w and the same parameters as the ODE, with an additional diffusion term in the voltage variable:

$$\begin{aligned} \frac{\partial v}{\partial t} &= D\Delta v + f(v) - w \\ \frac{\partial w}{\partial t} &= \epsilon(v - \gamma(x)w - \alpha(x)) \end{aligned} \tag{4.1}$$

The diffusion of voltage in eq. (4.1) represents current traveling through gap junctions in cardiac tissue. Since the conduction of current through gap junctions occurs in a manner proportional to the difference in membrane potential between adjacent cells, current travels down its electrical gradient, analogous to the process of chemical diffusion. The spatial term in (4.1) allows for the domain size, shape, and boundary conditions to exert additional effects on the behavior of the system. In the present work, we analyze the impacts of γ, α, boundary conditions, and domain constraints on action potential propagation.

4.3. Simulations of a 1D, 2-domain model with planar and radial diffusion

4.3.1. Approach. In order to understand the pacemaking properties of an ischemic or oscillatory area of tissue, we construct a one-dimensional domain consisting of two distinct subregions. Both subregions obey the FitzHugh-Nagumo (FHN) PDE (4.1), but the parameters differ: one region, representing the atrial tissue, has a standard set of excitable parameters ($\alpha = 0, \gamma = 1.5$); the second region, representing the SAN or an ischemic region, has excitability parameters α_{isch} and γ_{isch} that vary within the oscillatory, bistable, and monostable depolarized parameter regimes for the space-clamped FHN system (see fig. 4.2D).

Our goal is to analyze the relationship between the excitability parameters of the oscillatory or ischemic region, the curvature or relative size of the oscillatory/ischemic region, and the existence and stability of periodic waves propagating from the ischemic/oscillatory region through the excitable region. Following the approach in [**69**], we account for the effects of size and curvature at the interface by comparing results between systems using the radial diffusion operator $\frac{\partial^2}{\partial^2 r} + \frac{1}{r}\frac{\partial}{\partial r}$ versus the standard planar diffusion operator $\frac{\partial^2}{\partial^2 x}$. While the planar diffusion case represents planar waves in two dimensions, the radial diffusion case represents a slice of an annulus, and therefore generates predictions for a radially symmetric two-dimensional domain. Since the radial diffusion operator accounts for the curvature at the interface between the two regions, comparison between results with planar and with radial diffusion higlights the importance of the size and curvature of the ischemic region.

In the planar diffusion case we consider the interval $x \in [0, L]$, with an interface at $r_0 \in (0, L)$ such that for $x \leq r_0$, parameters are within the bistable, oscillatory, or monostable depolarized regime (representing ischemic tissue), while for $x > r_0$ parameters are set to standard values for excitable media. In the radial diffusion case, we take an annulus $r \in [l, L]$ with $l > 0$ small and $L = l + 256$, and similarly choose a point $r_0 \in (l, L)$ to denote the interface between the two regions. For $r \leq r_0$, parameters are within the bistable, oscillatory, or monostable depolarized regime, while for $r > r_0$ parameters are set to standard values for excitable media. We compare the results between planar and radial diffusion by choosing $r_0 = 15$, sufficiently small that the effect of the radial diffusion operator on solutions is noticeable. Between the planar and radial diffusion cases, we compare the regions of $(\alpha_{isch}, \gamma_{isch}, r_0)$ parameter space in which we observe 1:1 pacing, wave block, and any other behaviors. In particular, we analyze the effects of the parameter r_0 on the threshold for the onset of oscillations and the frequency and amplitude of these oscillations, as well as on the region of parameter space over which traveling waves occur.

4.3.2. Results. The planar diffusion case consists of the FHN PDE on the interval $x \in [0, L]$:

$$\frac{\partial v}{\partial t} = D\frac{\partial^2 v}{\partial x^2} + f(v) - w$$
$$\frac{\partial w}{\partial t} = \epsilon(v - \gamma(x)w - \alpha(x))$$

where $f(v) = -v(v-1)(v-a)$, with $a = 0.13$. The parameters $\gamma(x)$ and $\alpha(x)$ vary spatially:

$$\gamma = \begin{cases} \gamma_{isch} & x \leq r_0 \\ 1.5 & x > r_0 \end{cases}$$

$$\alpha = \begin{cases} \alpha_{isch} & x \leq r_0 \\ 0 & x > r_0 \end{cases}$$

In the radial diffusion case, we take an annulus $r \in [l, L]$ with $l > 0$ small, and simulate the system

$$\frac{\partial v}{\partial t} = D\left(\frac{\partial^2 v}{\partial r^2} + \frac{1}{r}\frac{\partial v}{\partial r}\right) + f(v) - w$$
$$\frac{\partial w}{\partial t} = \epsilon(v - \gamma(r)w - \alpha(r))$$

where $f(v) = -v(v-1)(v-a)$, with $a = 0.13$. The parameters $\gamma(r)$ and $\alpha(r)$ vary spatially, as above.

As in [**69**], we set L to 256. We compare the results between planar and radial diffusion by choosing $r_0 = 15$, sufficiently small that the effect of the radial diffusion operator on solutions is noticeable. We compare the regions of parameter space in which we observe 1:1 pacing, wave block, and any other behaviors.

4.3.2.1. *Dirichlet boundary conditions.* In order to contextualize the results in [**69**], we first apply Dirichlet boundary conditions at the inner boundary l. Thus, we set $v(l) = V_0$ where V_0 is determined as

$$V_0 = \begin{cases} 0.75 & \text{oscillatory system} \\ v^* & \text{bistable system} \end{cases}$$

where v^* is the upper (depolarized) stable steady state for the bistable ODE system. The Dirichlet boundary condition (BC) represents the assumption that the ischemic region is

large enough or insulated enough to remain at a depolarized resting voltage despite the electrotonic load from the surrounding excitable tissue. In contrast, a Neumann BC, which we explore below, represents the assumption of radial symmetry but allows for the ischemic region to fluctuate in membrane potential.

In the planar system with planar diffusion, there is a two-dimensional region of $(\gamma_{isch}, \alpha_{isch})$ space in which the ischemic region successfully paces the excitable region (fig. 4.3A). As α_{isch} increases, the range of γ_{isch} over which pacing occurs shifts toward lower values of γ_{isch} and widens slightly. For instance, when $\alpha_{isch} = 0$, 1:1 pacing occurs for approximately $4 < \gamma_{isch} < 9$, while for $\alpha_{isch} = 0.1$, 1:1 pacing occurs for approximately $1 < \gamma_{isch} < 8$. Wave block occurs for γ_{isch} too low or too high: when $\alpha_{isch} = 0$, wave block occurs for $\gamma_{isch} < 4$ and $\gamma_{isch} > 13$, while for $\alpha_{isch} = 0.1$, wave block occurs for $\gamma_{isch} > 11.5$. Between the regions of 1:1 pacing, there is an area of parameter space over which pacing appears to transition smoothly from 1:1 to 1:0 over a range of γ_{isch} values of width ~ 4 (4.3A, light blue region).

In the radial-diffusion system with $r_0 = 15$, there is again a region of $(\gamma_{isch}, \alpha_{isch})$ space over which 1:1 pacing occurs (4.3B, yellow area), and in which as α_{isch}, increases, the range of γ_{isch} over which oscillations occur shifts towards lower γ_{isch}. The 1:1 pacing region occurs over a higher range of γ_{isch} values in the radial diffusion than in the planar diffusion system. When $\alpha_{isch} = 0$, for example, 1:1 pacing is observed only for $\gamma_{isch} > 11.5$. In the radial diffusion case, we observe an additional region of parameter space, absent from the planar diffusion results, in which the ischemic region paces the excitable region in a 1:2 pattern (fig. 4.3B, green region). Although the region of 1:1 pacing is narrower for high α_{isch} in the radial than in the planar diffusion case, the region of wave block is also narrower in the radial diffusion case due to the additional, large parameter region of 1:2 pacing. The radial diffusion simulations also show a much narrower region of period-decrease than do the planar diffusion simulations as γ_{isch} increases from pacing to wave block. In the radial diffusion case, the system appears to instead transition abruptly from 1:1 or 1:2 pacing to wave block.

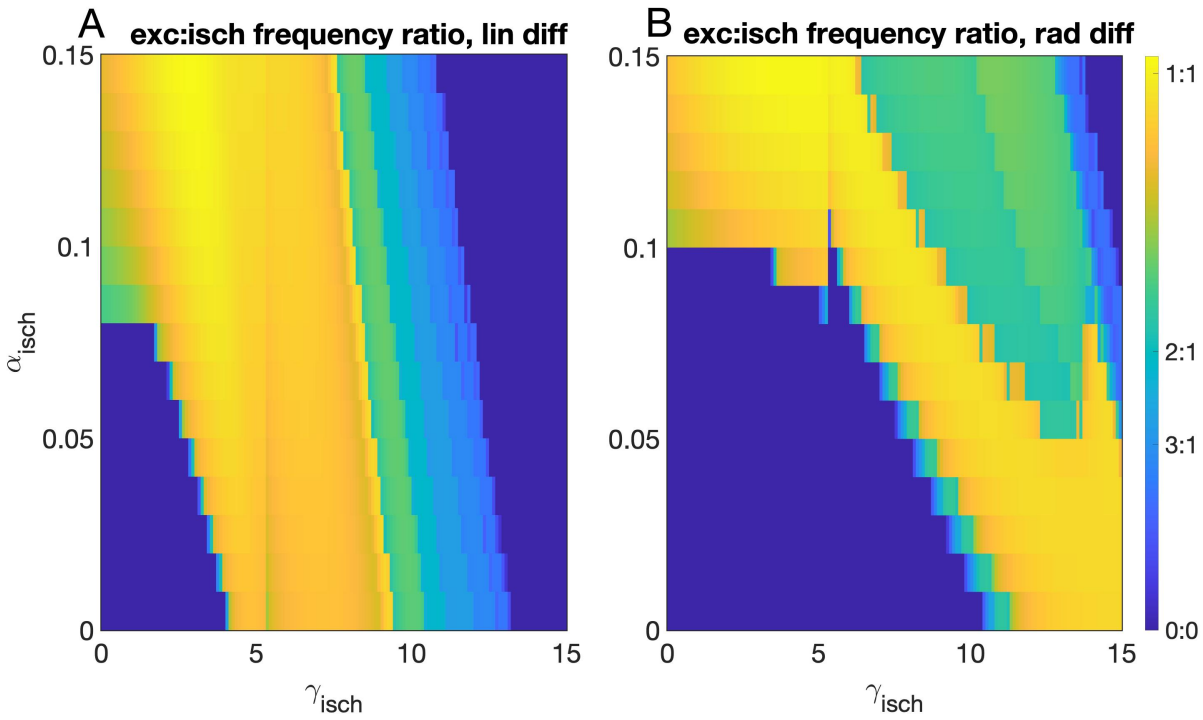

FIGURE 4.3. Frequency ratio between the excitable and ischemic regions, with a Dirichlet internal boundary condition, across a range of $(\gamma_{isch}, \alpha_{isch})$ values. In the planar system (A), with $\gamma_{exc} = 1.5$, there is a two-dimensional region of $(\gamma_{isch}, \alpha_{isch})$ space in which the ischemic region successfully paces the excitable region. In the radial diffusion system (B), when the radius is sufficiently small that the shape affects the pacemaking properties of the ischemic region ($r_0 = 15$), a region of $(\gamma_{isch}, \alpha_{isch})$ space arises in which 2:1 pacing occurs. In both planar and radial diffusion cases, the range of γ_{isch} over which 1:1 oscillatios occur shifts toward lower γ_{isch} as α_{isch} increases.

Comparison between fig. 4.3 panels A and B suggests that higher curvature (or smaller size) in an ischemic or oscillatory region widens the range of parameter space over which waves can propagate. Curvature also shifts the parameter regime over which beats can propagate toward higher γ_{isch} values, so that ischemic regions deeper in the bistable parameter regime are better able to propagate ectopic waves. Moreover, increased curvature increases the propensity for 1:2 pacing.

We can observe how these properties change as r_0 is varied over a range by fixing α_{isch} and varying γ_{isch} and r_0. In fig. 4.4, we plot the ratio of frequency between the ischemic and atrial region over a range of (γ_{isch}, r_0) with $\alpha_{isch} = 0$. For an ischemic region with r_0

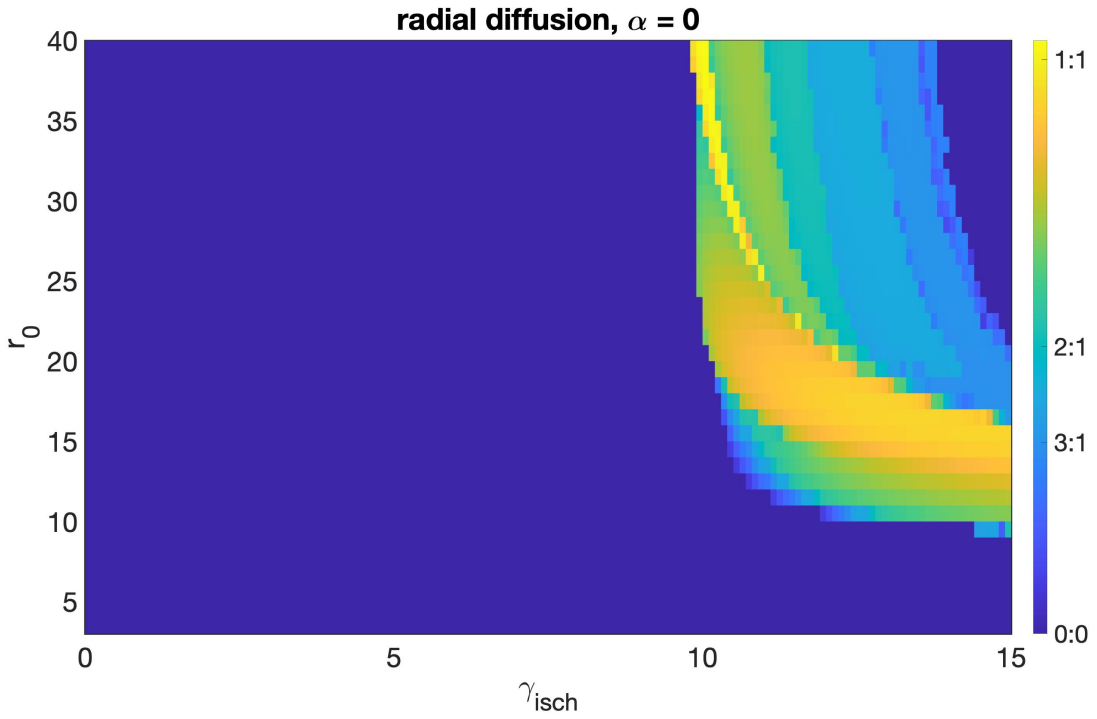

FIGURE 4.4. Frequency ratio (exc:isch) in the radial diffusion system with Dirichlet BCs, for fixed $\alpha_{isch} = 0$. There is a small region of 1:1 pacing, in which the range of γ_{isch} shifts toward lower γ_{isch} as size of the ischemic region r_0 increases. As r_0 decreases, i.e., for higher curvature, the minimum threshold γ^* at which oscillations arise increases, but the range of γ over which oscillations occur widens.

too small, i.e. less than ~ 9, waves do not propagate. However, above this minimal size, the frequency of spontaneous beats depends nonmonotonically on γ_{isch} and r_0. Notably, as r_0 decreases toward the minimal size for pacing, the threshold γ^* at which oscillations arise increases. Further, as r_0 decreases, the range of γ values over which oscillations occur also widens. When $r_0 = 15$, we observe pacing for $9.8 < \gamma_{isch} < 13.8$, while when $r_0 = 15$, pacing occurs from $\gamma \approx 10.6$ to $\gamma > 15$ (fig. 4.4). This suggests that for smaller ischemic regions, more bistable-like excitability makes ectopic waves more likely; for larger ischemic regions, only a finely-tuned range of parameters can produce ectopic waves.

4.3.2.2. *Neumann boundary conditions.* We next compare the planar and radial diffusion cases in the two-domain model with Neumann boundary conditions, where $\frac{dv}{dr}(l) = 0$. While the Dirichlet boundary condition represents a depolarized ischemic region with sufficient

current density and electrical insulation that it cannot hyperpolarize, the Neumann boundary better represents radial symmetry of the domain. We expect that the Neumann BC more appropriately represents an ischemic region, particularly of small size, as the electrotonic load from the surrounding excitable tissue plays an important role in mediating the ability of a spontaneously active region to generate waves.

In the planar diffusion case with Neumann boundary condition, unlike with Dirichlet boundary conditions, for α_{isch} too low (below ~ 0.07, waves do not propagate. This means that with Neumann boundaries, an ischemic region that is purely bistable rather than oscillatory cannot pace the excitable region. When α_{isch} is above this threshold, there is a wing-shaped region of (γ, α)-space over which 1:1 pacing occurs (fig. 4.5A). Within the 1:1 region, as α_{isch} increases, the range of γ_{isch} over which pacing occurs becomes narrower. For example, when $\alpha = 0.12$, 1:1 pacing occurs for $\gamma_{isch} < 8$, while for $\alpha = 0.36$, 1:1 pacing occurs only for $\gamma_{isch} < 5$. For α_{isch} above 0.43, only 1:2 pacing is observed. As with Dirichlet boundary conditions, for fixed γ_{isch}, as α_{isch} increases from the 1:1 pacing parameter region to the wave-block parameter region, there is an interval of γ_{isch} over which a transition occurs in which the pacing appears to transition smoothly in a period-decrease phenomenon from 1:1 through 2:1 and gradually to 1:0 pacing.

With radial diffusion, when the size of the SAN or ischemic region is sufficiently small ($r_0 = 15$), the region of parameter space over which 1:1 pacing occurs becomes narrower in α_{isch} and wider in γ_{isch} (fig. 4.5B, yellow region) as compared with the planar-diffusion results. In the radial diffusion simulations, the region of 1:1 pacing shifts toward higher γ_{isch}; pacing takes place for γ_{isch} as high as ~ 11.3 in the radial case, as compared with ~ 7.9 in the planar case. As with planar diffusion, in the radial-diffusion case there is a minimum α_{isch} below which no waves propagate; in the radial-diffusion case this minimum occurs slightly higher, at $\alpha_{isch} \approx 0.09$. The region of 1:1 pacing again has a winged shape, such that pacing occurs over the widest range of γ_{isch} when $\alpha_{isch} = 0.2$. As α_{isch} increases, the region of parameter space in which pacing occurs narrows with respect to γ_{isch}. In the radial case,

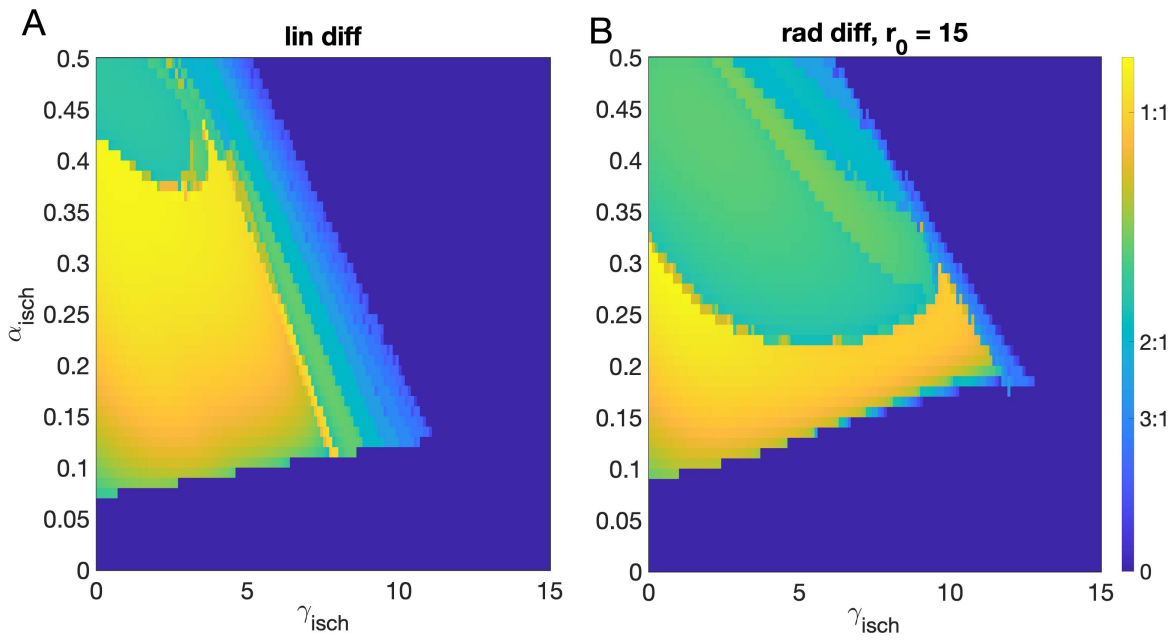

FIGURE 4.5. Atrial:SAN frequency ratio with homogeneous Neumann boundary condition in planar diffusion (A) and radial diffusion (B) over a range of $(\gamma_{isch}, \alpha_{isch})$ values. In the planar diffusion system with homogeneous Neumann boundary condition, a region of $(\gamma_{isch}, \alpha_{isch})$ space arises in which 1:1 pacing occurs for sufficiently high α and low γ. In the areas of parameter space just outside of the 1:1 pacing region, there are period-increase transitional regions where slower oscillations occur. Outside of these parameter regimes, the internal ischemic/oscillatory region is not able to drive traveling waves in the excitable region. In the radial diffusion system with homogeneous Neumann boundary condition, when the radius is sufficiently small that the shape affects the pacemaking properties of the ischemic region ($r_0 = 15$), a region of $(\gamma_{isch}, \alpha_{isch})$ space arises in which 2:1 pacing occurs for sufficiently high α and low γ.

there is a larger parameter region of 1:2 pacing: when $\alpha_{isch} > 0.33$, only 1:2 pacing occurs (fig. 4.5B). As in the simulations with Dirichlet boundaries, the radial diffusion simulations also show a much narrower region of period-decrease than do the planar diffusion simulations as γ_{isch} increases from pacing to wave block. In the radial diffusion case, the system appears to instead transition abruptly from 1:1 or 1:2 pacing to wave block.

In order to compare the effects of parameters over a range of sizes of an oscillatory or ischemic region, we consider the frequency of oscillations as a function of γ_{isch} and r_0 for fixed α_{isch}. When $\alpha_{isch} = 0$, no pacing occurs. This is consistent with intuition: for a

monostable or bistable ischemic region, with no current source at the center, the ischemic region does not produce a stimulus to pace the excitable region. When $\alpha_{isch} = 0.25$, as the size of the SAN changes there are several distinct regions of parameter space with respect to the frequency of traveling waves driven through the excitable region (fig. 4.6). There is a large region of 1:1 pacing, where the oscillatory or ischemic region drives the excitable region (fig. 4.6, region 1). When r_0 is too small or γ_{isch} is too large, no pacing occurs (fig. 4.6, regions 2 and 3). Notably, there appears to be a gradual period-decrease transition as γ_{isch} increases (fig. 4.6, region 4). However, we also see an isolated region of (α, γ)-space over which a distinct period doubling phenomenon occurs (4.6, region 4), which is entirely surrounded by the region of 1:1 pacing. Notably, there is a range of small ischemic area (r_0 below ~ 15) over which as r_0 increases, the width of γ_{isch}-space over which 1:1 pacing occurs widens and pacing occurs at higher γ_{isch} values. For r_0 above this interval, as r_0 continues to increase, the region of 1:1 pacing shifts toward lower γ_{isch}.

In order to characterize the behavior in each of the five regions labeled in fig. 4.6, we use space-time plots from representative points in regions 1-5. The behavior in each of the five different regions in fig. 4.6 is summarized by the space-time plots in fig. 4.7. In region 1, there is 1:1 pacing, in which every action potential in the oscillatory/ischemic region generates a propagating wave through the excitable region. In region 2, the oscillatory/ischemic region produces one action potential that propagates, but after this initial wave the excitable region remains hyperpolarized, although the ischemic region stays at a depolarized potential. In region 3, the ischemic region does not produce an initial wave, and instead approximately half of the ischemic region becomes hyperpolarized due to the electrotonic load from the excitable region. In region 4, the ischemic region stays hyperpolarized over time with small spatial oscillations that periodically propagate through the atrium at a lower frequency than the intrinsic frequency of the ischemic tissue. In region 5, the ischemic region fires distinct action potentials, and every other of these action potentials produces a wave that propagates through the excitable region. Notably, although the far-field exhibits steady

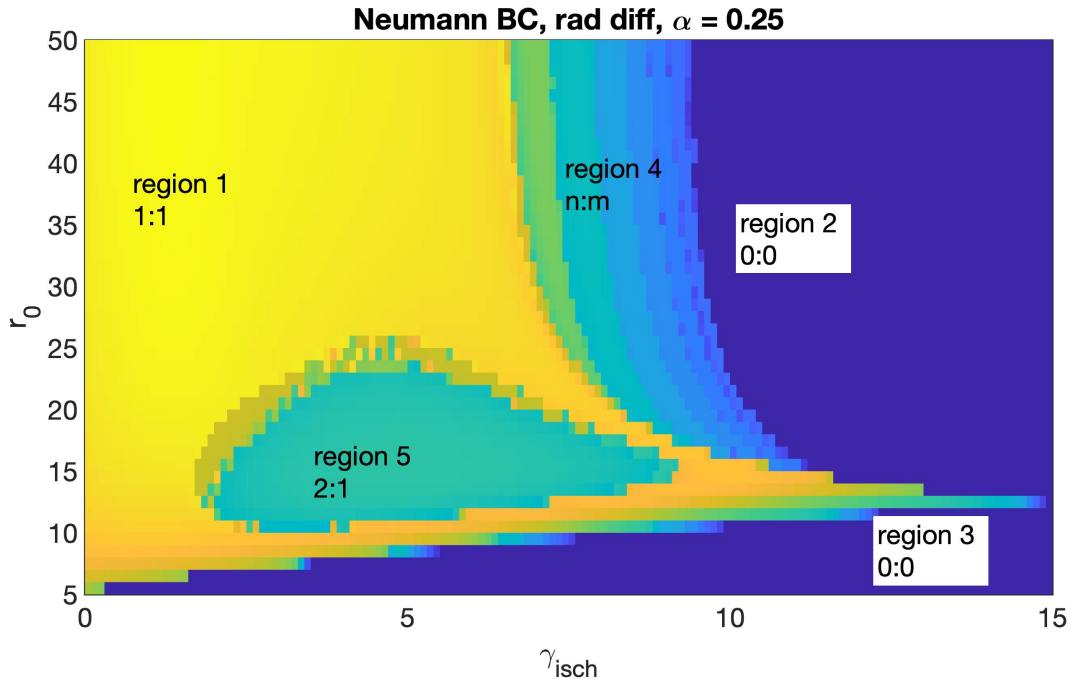

FIGURE 4.6. With homogeneous Neumann boundary condition and an oscillatory central region ($\alpha = 0.25$), as the radius of the SAN changes several different regions of different frequency traveling waves through the atrium are produced.

firing in both regions 4 and 5 at a frequency lower than that in the ischemic region, the behavior in the ischemic region differs markedly: in region 4, the ischemic region fluctuates slightly but remains depolarized between ectopic beats, while in region 5 the ischemic region hyperpolarizes between beats.

The results of our two-domain simulations, as summarized by heatmaps showing how the frequency of oscillations in the excitable region depends on γ_{isch}, α_{isch} and r_0 (figs. 4.3, 4.5, 4.9, 4.4, 4.6) and further detailed in space-time plots showing the time-course of the system in various parameter regimes, are highly complex in their dependence on both excitability parameters and curvature. Moreover, there are notable differences between results in the Neumann and Dirichlet BC studies; most notably, with Neumann BCs, the threshold representing the onset of oscillations is non-monotonic in slope (fig. 4.6), while with Dirichlet BCs the threshold has a monotonic, negative slope (fig. 4.4). We expect that the Neumann BC reflects a more physiologically realistic ischemic region because it allows

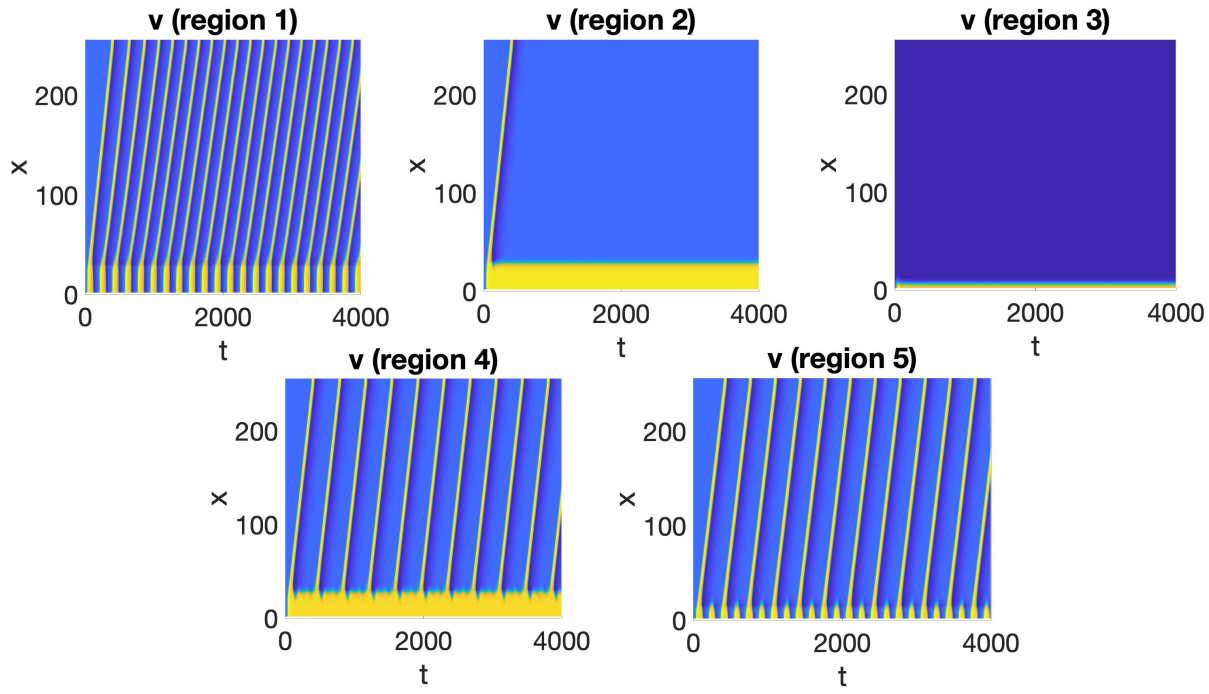

FIGURE 4.7. Space-time plots depicting the behavior of the FHN system with two domains and Neumann boundary condition $\frac{\partial v}{\partial r}(l) = 0$ representing radial symmetry.

for the electrotonic load from the surrounding tissue to influence the membrane potential of the ischemic region. Given that we are interested in the effects of small size and high curvature of an ischemic region on pacing, the Dirichlet BC, which assumes a sufficiently large ischemic region to prevent hyperpolarization, does not allow us to fully address these questions.

The complexity of results observed here led us to investigate subsequent reduced models: first we study 1D, one-domain models with Neumann boundary conditions and Dirichlet boundary conditions, where the activity of the ischemic or SAN region is reduced to a boundary condition. We investigate the relationship between the boundary condition, relative size of the SAN/ischemic region, and oscillations. Finally we consider a bulk system of two cells where an "atrial" or excitable cell is coupled to an "SAN/ischemic" (oscillatory/bistable) cell, and investigate the relationships between parameters and oscillations. In the two-cell case,

we use the phase planes to understand in greater depth the bifurcation structure underlying the patterns observed in the one- and two-domain PDE models.

4.4. Simulations and analysis of a 1D, 1-domain model with planar and radial diffusion

4.4.1. Approach. In order to reduce the full two-domain PDE study to an analytically tractable problem, we reduce the ischemic domain to a boundary condition and treat the excitable domain as a homogeneous one-dimensional cable. As in the two-domain model, we compare the behavior of the system with planar and radial diffusion in order to assess the impact of the radius of curvature at the interface on pacing properties. We first validate the reduction to a cable by examining the threshold behavior for waves propagating from the ischemic boundary through the excitable cable, and comparing the parametric dependence with the analogous results from the two-domain simulations.

In the single-domain tissue model, we use the boundary condition at the ischemic end of the cable as the bifurcation parameter, considering this analogous to a conglomerate measure of the excitability parameters α_{isch} and γ_{isch} from the full model. If the reduced single-domain replicates the complexity of behavior seen in the two-domain model, we can use spectral analysis to explain the mechanisms behind the bifurcations observed in the two-domain simulations. If the single-domain cable model does *not* replicate the complex behavior observed in the full model, we will instead speculate on how the distinguishing properties of the full two-domain system may give rise to fundamentally different results from those observed in a single-domain cable.

For the single-domain model, we simulate the FHN PDE on an interval $[r_0, R]$ representing an interval (planar diffusion) or an annulus (radial diffusion). The parameters in the domain correspond to an "excitable" medium in the FitzHugh-Nagumo system ($\alpha = 0, \gamma = 1.5$). We explore both Neumann and Dirichlet boundary conditions to attempt to explain the behavior in the two-domain system. In the single-domain model, Neumann nonhomogeneous

boundary conditions represent constant flux I_{SAN} through the point r_0 from the ischemic region. Dirichlet boundaries represent a pinned point $V(r_0) = V_0$ at the interface between the ischemic and excitable region. As in the 2-domain study, Neumann BCs more appropriately reflect radial symmetry, while Dirichlet BCs assume that the ischemic region is sufficiently large that the interface remains at an approximately constant membrane potential. In the 1-domain study, however, neither boundary condition allows for fluctuations in both the membrane potential and flux in the ischemic region.

First, we use the Neumann boundary condition $\frac{\partial V}{\partial r}_{r=r_0}\Big| = I_{SAN}$ to represent current traveling from the SAN or ischemic region into the excitable region. The curvature and size of the internal ischemic or pacemaking region are captured by the boundary value r_0, the radius at the interface between the two regions. We assess the overall dependence of frequency of action potentials propagating through the tissue on I_{SAN} and r_0. The parameter I_{SAN} is used as a bifurcation parameter. We compare planar with radial diffusion to investigate how, with radial diffusion, a small r_0 (high curvature or small ischemic region) affects the threshold I^*_{SAN} at which a Hopf bifurcation occurs, leading to the onset of periodic propagating waves. We also investigate how curvature influences the size of the region of parameter space over which periodic propagating waves occur. We verify the results of these simulations by analyzing the eigenvalues and eigenfunctions associated with the Hopf bifurcation at which the stationary solution to the PDE destabilizes into oscillations.

Next, we use the Dirichlet boundary condition $V(r_0) = V_0$ to represent a depolarized ischemic region functioning as a current source. As in the Neumann case, we use the parameter V_0 as a bifurcation parameter. We investigate how both V_0 and r_0 affect the frequency of periodic oscillations throughout the tissue. Simulations are verified by the spectral properties of the system at the Hopf bifurcation.

Comparison between the one- and two-domain PDE studies indicates that, while the Dirichlet boundary is insufficient to produce propagating waves through an excitable region, the case with Neumann boundary condition exhibits some (but not all) of the pacing schemes

present in the full two-dimensional model. In the regions of parameter space in which the single-domain cable model does provide analogous results to those seen in the two-domain model, we use the spectral properties of the PDE to attempt to explain the bifurcations observed in simulations.

4.4.2. Mathematical Setting: 1D model. We are interested in the threshold behavior for waves that propagate through the excitable region, and in particular, how the threshold for periodic waves depends on the curvature or relative size of the ischemic region at the ischemic-excitable interface (in this case, at the innermost boundary). First we reduce the ischemic region as a Dirichlet boundary, i.e., fixed at a depolarized membrane potential, which represents an ischemic region with sufficiently robust source current or insulation to prevent hyperpolarization despite the electrotonic load of the excitable region. Second, we model the ischemic region as a nonzero Neumann boundary, i.e., a constant current input.

We analyze the relationship between the boundary condition representing excitability in the ischemic/oscillatory region, the curvature or relative size r_0 at the oscillatory/ischemic region at the interface between the two regions, and the existence and stability of periodic waves propagating from the ischemic/oscillatory boundary through the excitable region. As in the two-domain model, we account for the effects of size and curvature at the interface by comparing results between identical systems using the radial diffusion operator versus the standard planar diffusion operator.

The planar diffusion case consists of the FHN PDE on the interval $x \in [r_0, L]$:

$$\begin{aligned} \frac{\partial v}{\partial t} &= D\Delta v + f(v) - w \\ \frac{\partial w}{\partial t} &= \epsilon(v - \gamma(x)w - \alpha(x)) \end{aligned} \tag{4.2}$$

where $f(v) = -v(v-1)(v-a)$, with $a = 0.13$; $\gamma = 1.5$, and $\alpha = 0$.

In the radial diffusion case, we take an annulus $r \in [r_0, L]$ with $l > 0$ small, and simulate the system

$$\frac{\partial v}{\partial t} = D\left(\frac{\partial^2 v}{\partial r^2} + \frac{1}{r}\frac{\partial v}{\partial r}\right) + f(v) - w \tag{4.3}$$
$$\frac{\partial w}{\partial t} = \epsilon(v - \gamma(r)w - \alpha(r))$$

where again $f(v) = -v(v-1)(v-a)$, with $a = 0.13$; $\gamma = 1.5$, and $\alpha = 0$. For the Dirichlet BC study, we define $V_0 = v(r_0)$ and allow V_0 to vary over a wide range of values. Similarly, in the Neumann BC study, we take $\frac{\partial r}{\partial r}\big|_{r=r_0} = I_{SAN}$ and allow I_{SAN} to vary. As in [**69**], we set L to 256; the planar diffusion case corresponds to an interval of length $L - r_0$, while the radial diffusion case corresponds to an annular slice of a radially symmetric domain with inner radius r_0 and outer radius L. We compare the results between planar and radial diffusion by choosing $r_0 = 15$, sufficiently small that the effect of the radial diffusion operator on solutions is noticeable. We are interested in periodic traveling waves, the threshold of their onset, and how the curvature or size r_0 affects threshold behavior and wave propagation.

In each scenario, we attempt to answer the question of which behaviors of the two-domain model (i.e., fig. 4.6) can be explained by each reduced 1D model. We then analyze the spectral properties of the system, by computing the stationary steady state and linearizing around it as described below (taken from [**56**] and [**69**]), and use the behavior of the eigenvalues and eigenfunctions to help explain the results seen in the simulations.

There is a stationary solution $(\phi(x), \eta(x))$ to the planar diffusion system in which $\phi(x)$ solves the 2nd order ODE

$$D\Delta\phi - \left(f(\phi) + \frac{\phi - \alpha}{\gamma}\right) = 0$$

and, $\frac{\partial w}{\partial t} = 0$ implies that $\eta(x) = \frac{\phi - \alpha}{\gamma}$. We seek to identify the stationary solution and its stability, as well as how its stability depends on parameters and boundary conditions. It was established in [**35**] and [**56**] that the stationary solution destabilizes via a Hopf bifurcatiion for certain values of α; [**69**] expanded this work to account for radial diffusion in a domain

with curvature. Therefore, we expect that the oscillations that produce periodic propagating waves arise from the destabilization of the stationary solution in a Hopf bifurcation.

In order to characterize the stability of the stationary solution, we first use MATLAB's `fsolve` function to identify the constant-in-time solution $(\phi(x), \eta(x))$ to (4.2). We then linearize around $(\phi(x), \eta(x))$ by assuming $v = \phi + e^{\lambda t}\psi(x)$ and $w = \eta + e^{\lambda t}\xi(x)$, and obtain the following ODE for $\psi(x)$:

$$-D\frac{\partial^2\psi}{\partial x^2} + f'(\phi(x))\psi + \left[\lambda + \frac{\epsilon}{\lambda + \epsilon\gamma}\right]\psi = 0 \tag{4.4}$$

We solve for λ and $\psi(x)$ by evaluating the Jacobian of (4.2) at $(\phi(x), \eta(x))$ and then using MATLAB's `eig` function to identify the eigenvalues and eigenvectors of the Jacobian.

In the radial diffusion case, the stationary solution $\varphi(r)$ solves the modified ODE

$$D\Delta\varphi + \frac{1}{r}\frac{\partial\varphi}{\partial r} - \left(f(\varphi) + \frac{\varphi - \alpha}{\gamma}\right) = 0$$

which results in a modified linearization for which the eigenfunction $\chi(r)$ solves the equation

$$-D\left(\frac{\partial^2\chi}{\partial r^2} + \frac{\partial\chi}{\partial r}\right) + f'(\varphi(x))\chi + \left[\lambda + \frac{\epsilon}{\lambda + \epsilon\gamma}\right]\chi = 0 \tag{4.5}$$

As with planar diffusion, we use `fsolve` to identify the stationary solution, evaluate the Jacobian of (4.3) at the stationary solution, and use `eig` to find the eigenvalues and eigenvectors of the Jacobian. We analyze the eigenvalues λ of this system with greatest real parts, and how they depend on parameters. We examine both Neumann and Dirichlet boundary conditions: in the Dirichlet case, the boundary condition is $V_0 = V(r_0)$ and in the Neumann case $I_{SAN} = \frac{\partial v}{\partial r}\big|_{r_0}$ in the Neumann case. In both scenarios, the boundary condition is considered as the main bifurcation parameter.

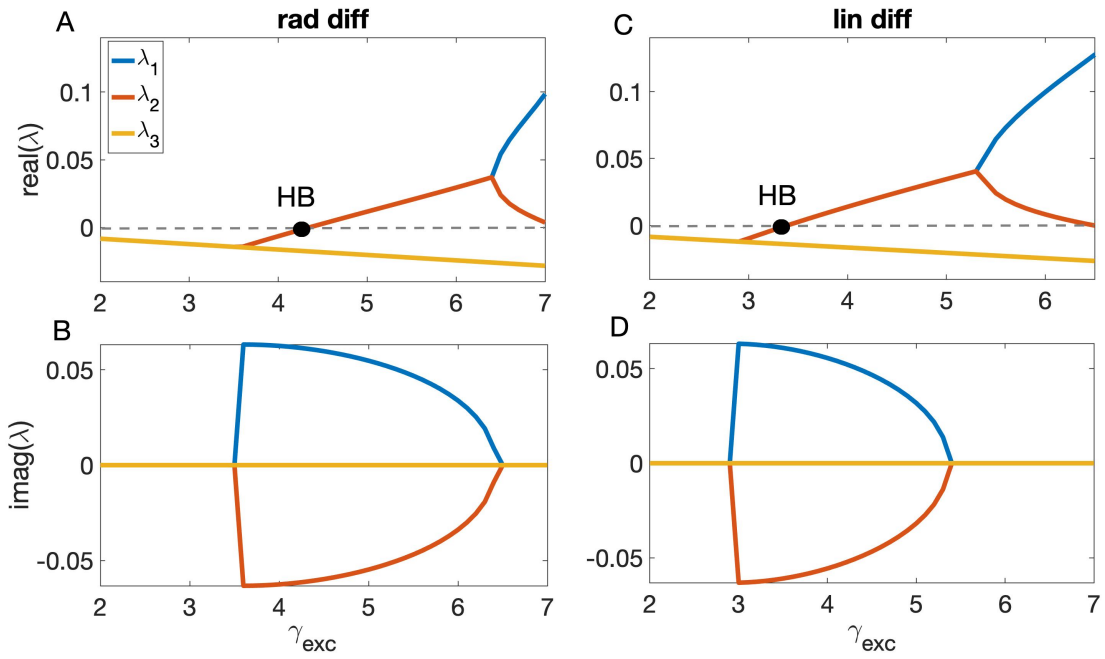

FIGURE 4.8. The three eigenvalues with largest real part γ_1, γ_2 and γ_3 of the Jacobian at the stationary solution to (4.2) (A,B) and (4.3) (C, D) with Dirichlet boundary condition $V_0 = 0.9$. The eigenvalues depend on the parameter γ_{exc}, which determines whether or not oscillations arise in the excitable region. Periodic traveling waves are observed when the real part of one eigenvalue becomes positive, i.e., for $\gamma \geq\sim 4.5$ in the radial diffusion case and $\gamma \geq\sim 3.5$ in the planar diffusion case.

4.4.3. Results.

4.4.3.1. *Dirichlet BCs.* In the Dirichlet boundary case, under the parameters described in [**69**] with $\gamma_{exc} = 1.5, \alpha_{exc} = 0$, the ischemic region is unable to pace the excitable region for any boundary condition V_0 (data not shown). This is confirmed by the eigenvalues for the system, all of which have negative real part. On the other hand, if we fix $V_0 = 0.9$ and vary γ_{exc}, we observe that there is a Hopf bifurcation as γ_{exc} is varied closer to the threshold of bistability; at $\gamma_{exc} \approx 4.2$ in the radial diffusion system and $\gamma_{exc} \approx 3.3$ in the planar diffusion system, the eigenvalue with highest real part crosses the imaginary axis so that its real part is positive (fig. 4.8 A, C). Beyond this threshold the ischemic region is able to pace the excitable region.

Because the Dirichlet boundary condition is unable to excite an atrial region with $\gamma = 1.5$, $\alpha = 0$ for any fixed voltage V_0, we conclude that the Dirichlet system does not capture the dynamics of the full two-domain model. This suggests that the existence of traveling waves, and the complexity of parameter dependence captured in fig. 4.6, requires flexibility at the interface between the SAN (or ischemic region) and the atrium (or excitable region).

4.4.3.2. *Neumann BCs.* With a Neumann boundary condition $I_{SAN} = \frac{\partial v}{\partial r}\big|_{r_0}$, I_{SAN} represents current flowing into the excitable region from an ischemic or oscillating region.

In a one-dimensional domain $x \in [r_0, L]$ with Neumann boundary conditions $\frac{\partial u}{\partial x}\big|_{x=r_0} = I_{SAN}$ at one end and $\frac{\partial u}{\partial x}\big|_{x=L} = 0$ at the opposite end, the injected current I_{SAN} paces the tissue under some parameter conditions dependent on I_{SAN}. We capture the overall behavior over a range of parameters in figure 4.9A. When I_{SAN} is too small (below ~ 0.15), the ischemic boundary is unable to pace the excitable cable. As I_{SAN} passes this threshold and continues to increase, frequency abruptly jumps to a high value (≈ 0.025), continues to increase slightly, and then abruptly drops to approximately half its value around $I_{SAN} = 035$. Finally, for $I_{SAN} > 0.55$, no pacing occurs.

In the one-dimensional effectively annular domain $r \in [r_0, L]$ with Neumann boundary conditions $\frac{\partial u}{\partial r}\big|_{r=r_0} = I_{SAN}$ at the inner radius and $\frac{\partial u}{\partial x}\big|_{x=L} = 0$ at the outer radius, pacing depends on both I_{SAN} and r_0 (fig. 4.9B). For r_0 too small (below ~ 5), no pacing occurs. As with planar diffusion, for I_{SAN} either too small or too large (below ~ 0.15 or above ~ 0.55), the boundary is unable to pace the excitable tissue. Between these parameter regimes, there is a region over which pacing occurs. Within the area of parameter space in which the ischemic boundary can produce propagating periodic waves, there are distinct regions of different frequencies. For fixed r_0, as I_{SAN} increases, the onset of waves occurs with a frequency ≈ 0.03, followed by a period-halving transition to a frequency ≈ 0.015 at $I_{SAN} \approx 0.35$, and finally a transition back to wave block. As r_0 increases beyond ~ 35, the sizes of parameter regions in which 1:1 and 1:2 pacing occur remain fixed.

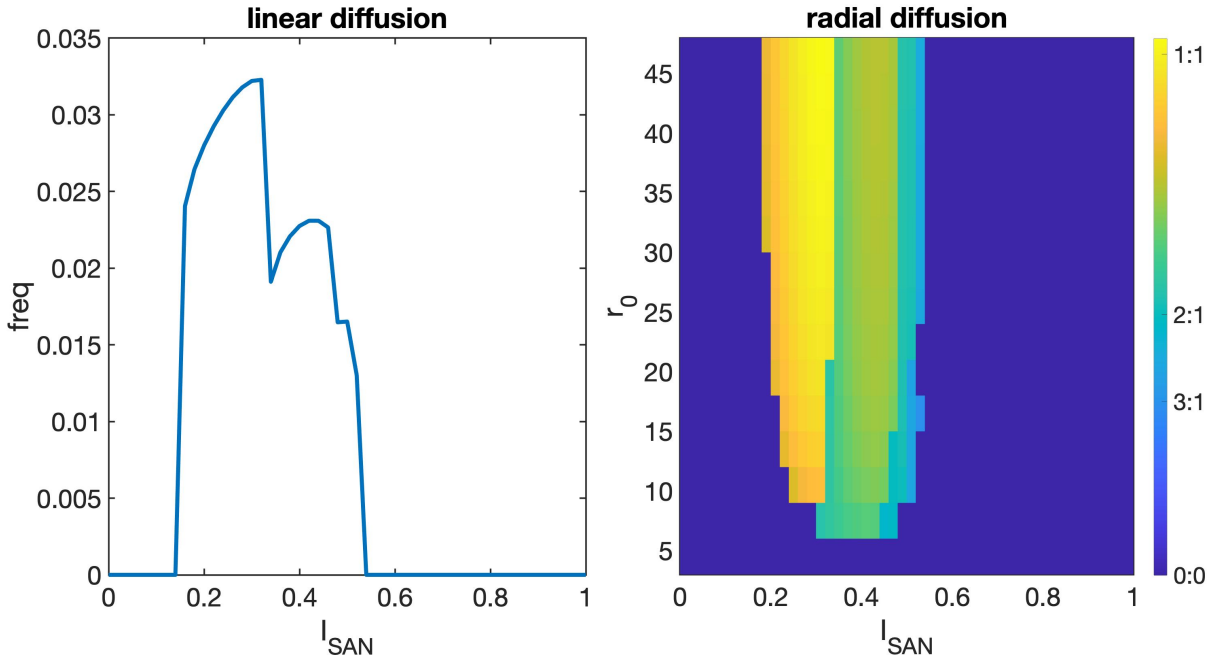

FIGURE 4.9. A Neumann oundary condition representing injected current from the SAN or an ischemic region can successfully pace a length of excitable tissue in some parameter conditions. Notably, with planar diffusion (A) as I_{SAN} increases from 0, the system undergoes a Hopf bifurcation at the onset of oscillations, followed by a period doubling behavior, before the oscillations cease. With radial diffusion (B), the system also undergoes the onset, period-doubling, and cessation of oscillation as I_{SAN} increases; however, for sufficiently small r_0, only half-frequency pacing occurs, and for r_0 too small there is no pacing.

The behavior in each of the four regions in fig. 4.9 is summarized by space-time plots in fig. 4.10. In region 1 (fig. 4.10A), 1:1 pacing occurs, wherein oscillations arise at the inner boundary and propagate through the tissue. In regions 2 and 3 (fig. 4.10B and C), a single wave propagates from the inner radius through the domain, followed by wave block. In region 4 (fig. 4.10) we observe behavior analogous to 2:1 pacing, in which a small area near the inner boundary exhibits oscillations in membrane potential, and every other one of these oscillations results in an action potential wave propagating throughout the medium.

The results of fig. 4.10 are to some extent comparable with those in the two-domain analogue fig. 4.7, although the comparison is incomplete. While region 1 (1:1 pacing) in

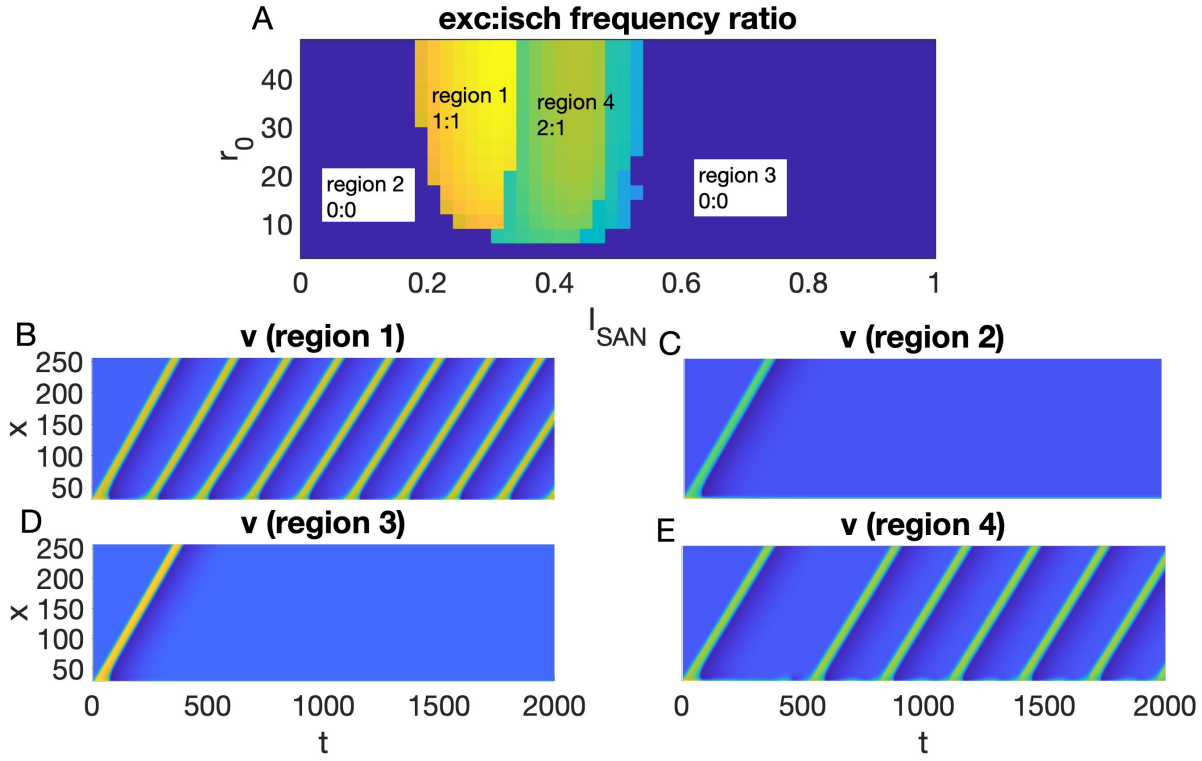

FIGURE 4.10. Space-time plots for the 1D, 1-domain model where the Neumann boundary condition $I_{SAN} = \frac{\partial v}{\partial r}(r_0)$ is used to represent input from the SAN into the excitable region. Panels correspond to the four regions of parameter space defined in fig. 4.9. In region 1, 1:1 pacing occurs, while in regions 2 and 3 there is block. In region 4 there is 2:1 pacing.

the single-domain model corresponds well to region 1 in the two-domain model, comparison between the other regions is less obvious. In both regions 2 and 3 of the single-domain model, the ischemic boundary is able to propagate one initial wave throughout the domain, whereas in region 3 of the two-domain model even this initial wave is blocked. Thus, both regions 2 and 3 of fig. 4.10 correspond more appropriately to region 2 of fig. 4.7. Moreover, region 4 of fig. 4.10 may correspond to either region 4 or region 5 of fig. 4.7, given that the fluctuations within the oscillatory/ischemic region in the two-domain model cannot be observed in the single-domain setup.

We further analyze the behavior of the 1D system by examining the spectrum of the linearization 4.4.2 in the planar domain with Neumann boundary conditions (fig. 4.11). At the onset of oscillations ($I_{SAN} \approx 0.15$), the system undergoes a Hopf bifurcation at which a

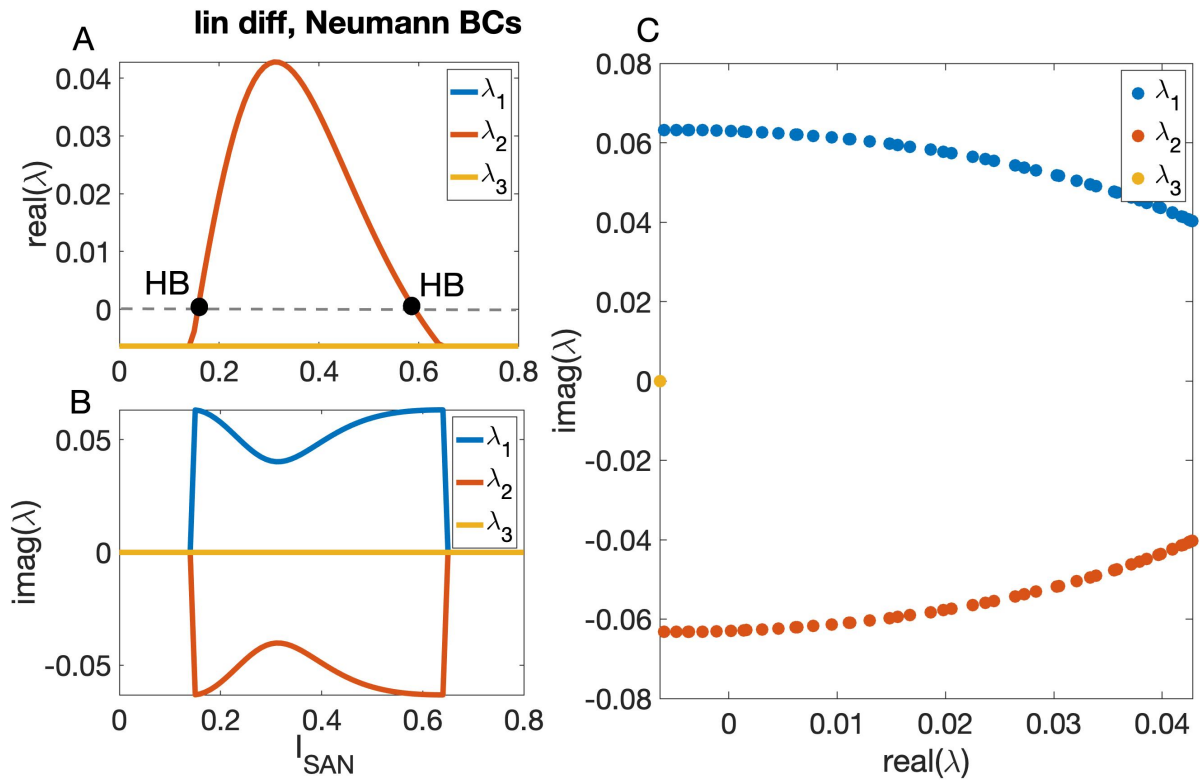

FIGURE 4.11. Eigenvalues corresponding to the stationary solution in a 1D domain of length 256 with $r_0 = 5$ and Neumann boundary condition I_{SAN} at r_0. A: as I_{SAN} varies, the real part of one eigenvalue crosses the imaginary axis. B: the real part of one eigenvalue is positive when I_{SAN} is between approximately 0.17 and 0.6, corresponding to the parameter regime in which oscillations occur. C: The imaginary part of the eigenvalue whose real part is positive is approximately 0.6 at the Hopf bifurcation, indicating a frequency of oscillations ≈ 0.6.

copmlex conjugate pair of eigenvalues crosses the imaginary axis, destabilizing the stationary solution. Oscillations occur in the system while the greatest real part of a complex eigenvalue is positive, which occurs when I_{SAN} is between approximately 0.17 and 0.6. The frequency of the oscillations at the onset is equal to the imaginary part of the corresponding eigenvalue whose real part is positive, and therefore is approximately 0.06 for the parameters given (fig. 4.11C).

In order to assess the effects of curvature on wave propagation, we compare the spectrum for the linearization in the planar diffusion case to that in the radial diffusion case (4.4.2) with $r_0 = 5$, sufficiently small to observe effects on systemic behavior due to curvature. With

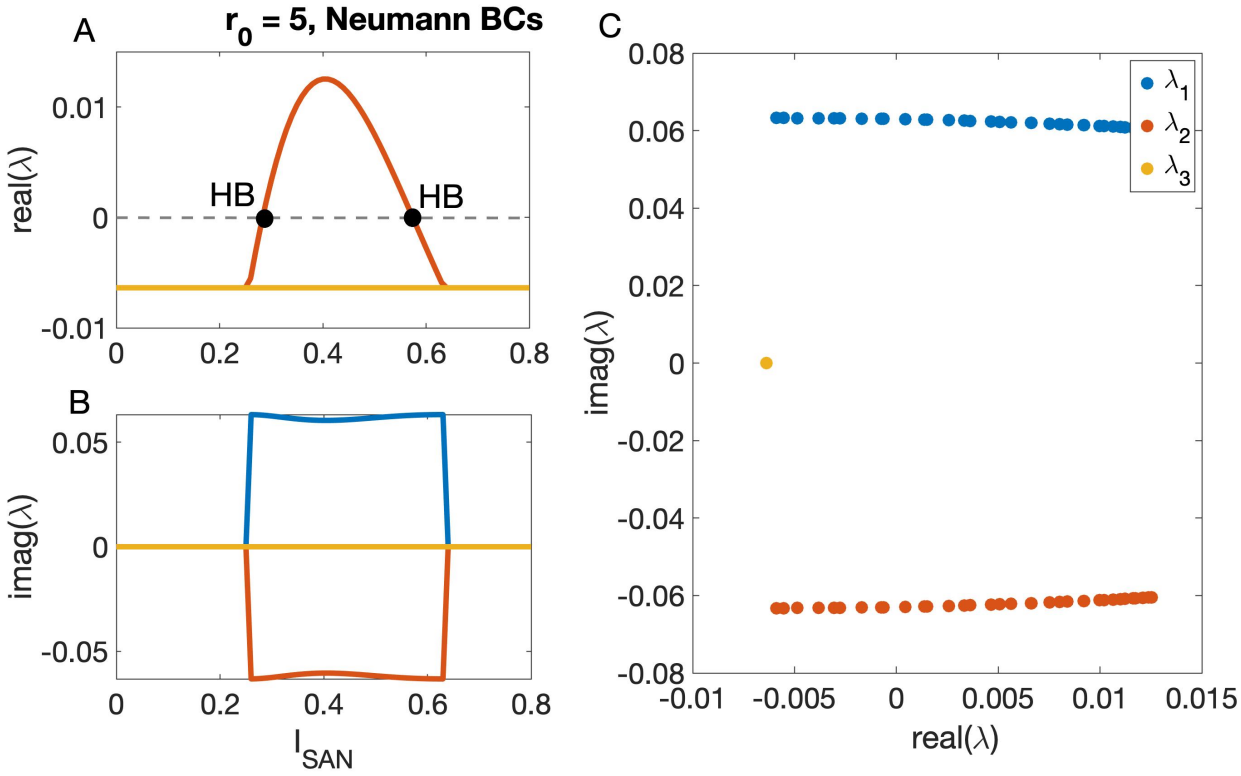

FIGURE 4.12. Eigenvalues corresponding to the stationary solution in an annular domain $[r_0, R]$ of width 256 with Neumann boundary condition I_{SAN} at the smaller-radius end $r = r_0$. A: as I_{SAN} varies, the real part of one eigenvalue crosses the imaginary axis. B: the real part of one eigenvalue is positive when I_{SAN} is between approximately 0.28 and 0.58, corresponding to the parameter regime in which oscillations occur. C: The imaginary part of the eigenvalue whose real part is positive is approximately 0.6 at the Hopf bifurcation, indicating a frequency of oscillations ≈ 0.6.

Neumann boundary condition $\frac{\partial u}{\partial r}\big|_{r=r_0} = I_{SAN}$ at the inner radius r_0, the system undergoes a Hopf bifurcation at which one eigenvalue crosses the imaginary axis, destabilizing the stationary solution, as the boundary condition I_{SAN} increases (fig. 4.12). Oscillations occur in the system when the greatest real part of an eigenvalue is positive, which occurs when I_{SAN} is between approximately 0.28 and 0.58. The frequency of the oscillations at the onset is equal to the imaginary part of the corresponding eigenvalue whose real part is positive, and therefore is approximately 0.6 for the parameters given (fig. 4.12C).

Comparison between figures 4.11 and 4.12 suggests that radial diffusion with small r_0, representing an ischemic or oscillatory region that is small or has high curvature at the

boundary, shifts the range of parameters in which pacing occurs toward higher I_{SAN}. That is, for a smaller ischemic region, higher current is required at the inner radius in order to generate periodic waves that propagate through the excitable region. Moreover, the range of I_{SAN} over which propagating periodic waves occur is narrower in the radial diffusion case than in the planar diffusion case, suggesting that the strength of source current must be more finely-tuned for a smaller icshemic/oscillatory region to produce periodic waves than a larger ischemic/oscillatory region.

Interestingly, the results in a 1D cable where the excitable region is stimulated by only a Neumann or Dirichlet boundary condition exhibit qualitatively different behavior from the 2-domain case. The ischemic region reduced to a Dirichlet boundary fails to pace the excitable region over all values of V_0. Reduction of the ischemic region to a Neumann boundary results in pacing, but the qualitative relationships between parameters and frequency are markedly different from the full 2-domain case. The discrepancy of results between the 2-domain system and the 1-domain cable highlights the necessity of the independent, but coupled behavior of the two domains, and hints at the importance of the interface between the ischemic and the excitable regions: if the voltage or the flux at this point must be dynamic rather than fixed in order to capture accurate results, then a fixed boundary condition will change the qualitative behavior of the system.

4.5. Simulations and analysis in a two-cell ODE model

4.5.1. Approach. We use a reduced ODE model to gain insight regarding the size and relative excitability of the SAN and atrium and the net coupling strength between them. The space-clamped model allows us to examine these factors separately from the complexity of the geometry of the SAN.

Here, we consider a model in which one oscillatory, bistable or monostable depolarized cell is coupled to one excitable (atrial) cell. This setup can be thought of as a course-grained or "bulk" model of a region of SAN tissue, or ischemic tissue, coupled to a region of atrial tissue; if a region of oscillatory tissue can drive a region of excitable tissue to oscillate,

then this driving must also be theoretically possible in a two-cell model under appropriate parameter conditions. Similar work has been done before with various configurations and approaches: see [**34**] for an exploration of the qualitative types of behavior that can arise depending on the resistivity parameter, and [**52**] for an in-depth bifurcation analysis of a coupled system of an atrial cell with an ischemic cell.

We use the FitzHugh-Nagumo model, with two cells coupled by diffusive conduction:

$$\begin{aligned}
\frac{\partial v_{isch}}{\partial t} &= f(v_{isch}) - w_{isch} + g_j \left(\frac{r_{exc}}{r_{isch}}\right)^2 (v_{exc} - v_{isch}) \\
\frac{\partial w_{isch}}{\partial t} &= \epsilon(v_{isch} - \gamma_{isch} w_{isch} - \alpha_{isch}) \\
\frac{\partial v_{exc}}{\partial t} &= f(v_{exc}) - w_{exc} + g_j \left(\frac{r_{isch}}{r_{exc}}\right)^2 (v_{isch} - v_{exc}) \\
\frac{\partial w_{exc}}{\partial t} &= \epsilon(v_{exc} - \gamma_{exc} w_{exc} - \alpha_{exc})
\end{aligned}$$

The parameter g_j represents the conductance between the sinoatrial node and the atrium; ϵ is a time constant for the relatively slow refractory variable w(sometimes corresponding to potassium currents); γ defines the steepness of the potassium activation curve; and α can be interpreted equivalently as a change in potassium equilibrium potential or an injected current. The parameters r_{exc} and r_{isch} denote the effective radii of the atrial/excitable cell and the ischemic/oscillatory cell, respectively. We will consider $r_{exc} \geq r_{isch}$ in order to consider the effects of current from a relatively smaller ischemic or oscillatory region diffusing into a larger excitable region, which can also be interpreted as mimicking the presence of positive curvature in the boundary at the interface between the two regions. The cubic function $f(v)$ is defined, as above, by

$$f(v) = -v(v-1)(v-a)$$

where $a = 0.13$. The two-cell model uses the size ratio $r = r_{isch}/r_{exc}$ as a coarse representation of the relative curvature of the boundary between the ischemic and excitable regions. Positive curvature at the interface in a two-dimensional system results in an excitable region that is locally larger than the ischemic region; therefore, $r_{isch}/r_{exc} = 1$ corresponds to a system with planar diffusion, whereas $r_{isch}/r_{exc} > 1$ represents a 2D system with radial diffusion.

4.5.2. Results. We use a reduced ODE model of two coupled cells with distinct electrical properties to gain insight regarding the relationship between the relative sizes of the two cells, excitability of the SAN cell, and the ability of the SAN or ischemic cell to pace the excitable cell. The space-clamped model allows us to examine these factors separately from the complexity of the geometry of the SAN.

4.5.2.1. *Simulations.* In the reduced system of two coupled cells, we investigate the role of the relationship between the relative sizes and the electrical properties of two coupled cells on the ability of the ischemic cell to pace the atrial cell. We constrain one cell to a monostable, excitable parameter regime ("atrial" cell), fix the net conductance between the two cells to $g_j = 0.05$, and vary the parameters α_{isch} and γ_{isch} in the second cell ("ischemic" cell) across the oscillatory and bistable regions of parameter space (see fig. 4.2C).

In our simulations across a range of $(\alpha_{isch}, \gamma_{isch})$ parameter space, we observe several regions characterized by distinct behavior in the four-dimensional system (fig. 4.13). For sufficiently low γ_{isch} and moderate α_{isch}, the spontaneously active cell paces the excitable cell in a 1:1 rhythm (fig. 4.13A and B, yellow regions). When α_{isch} is increased further, there is a region of period doubling where every other oscillation in the ischemic cell drives an action potential in the atrial cell (fig. 4.13A and B, green regions). Outside of these regions, as in blue regions in fig. 4.13, there are no action potentials – this includes some areas of subthreshold oscillations. The occurrence of 1:1 and 2:1 pacing depend on both the size ratio between the two regions and on the parameters in the ischemic cell. For two cells of equal size (fig. 4.13A), when $\alpha = 0$ corresponding to a monostable or bistable ischemic

cell, there are no oscillations over a range of γ_{isch} values. However, as α_{isch} is increased, there is a region of $(\alpha_{isch}, \gamma_{isch})$-space where 1:1 pacing occurs. That is, each action potential in the ischemic cell drives an action potential in the excitable cell, and these action potentials occur periodically. As α_{isch} increases further, there is a region of 2:1 pacing, followed by the cessation of pacing. For a fixed size ratio of $r_{isch}/r_{exc} = 0.833$, representing positive curvature at the interface between the ischemic and excitable regions (fig. 4.13B), the qualitative behavior is similar: when $\alpha_{isch} = 0$ there are no oscillations. As α_{isch} is increased, there is a region of $(\alpha_{isch}, \gamma_{isch})$-space where 1:1 pacing occurs, and as α_{isch} increases further, there is a region of 2:1 pacing, followed by the cessation of pacing. In the positive-curvature case, the range of α_{isch} producing 1:1 pacing narrows, and the range of α_{isch} producing 2:1 pacing grows toward lower α_{isch}, as compared with the case of equally-sized cells. Moreover, in the positive-curvature case, the region of 1:1 pacing broadens toward higher γ_{isch} values relative to the same region in the equally-sized cells case.

We next evaluate more precisely how the onset of oscillations depends on the size ratio r_{isch}/r_{exc} between the two cells. We fix α_{isch} at an intermediate value of 0.25 and vary both γ_{isch} and the size ratio between the two cells. The overall dependence of pacing on γ_{isch} and size ratio is complex (fig. 4.14): there is a region of 1:1 pacing and a region of 2:1 pacing, as well as an isolated region of wave block, and the atr:SAN frequency ratio does not change monotonically as the relative size of the atrial cell increases in comparison to the size of the oscillatory/ischemic cell. For sufficiently high γ_{isch}, no pacing occurs. Similarly, for sufficiently small ischemic cell, no pacing occurs. When γ_{isch} is sufficiently small (below ≈ 8), the oscillatory cell successfully paces a small excitable cell, but increasing the size of the excitable cell gives rise to period doubling (fig. 4.14, green region). For intermediate values of γ_{isch} (between ≈ 5 and 8), the region of 2:1 pacing disappears and an isolated region of wave block occurs as the excitable cell's size grows (fig. 4.14, blue region surrounded by yellow area). For γ_{isch} between ≈ 8 and 10, as size ratio increases from 0.5 to 1 the system goes from no pacing to 1:1 pacing to no pacing. Thus, toward the higher end of γ_{isch} for

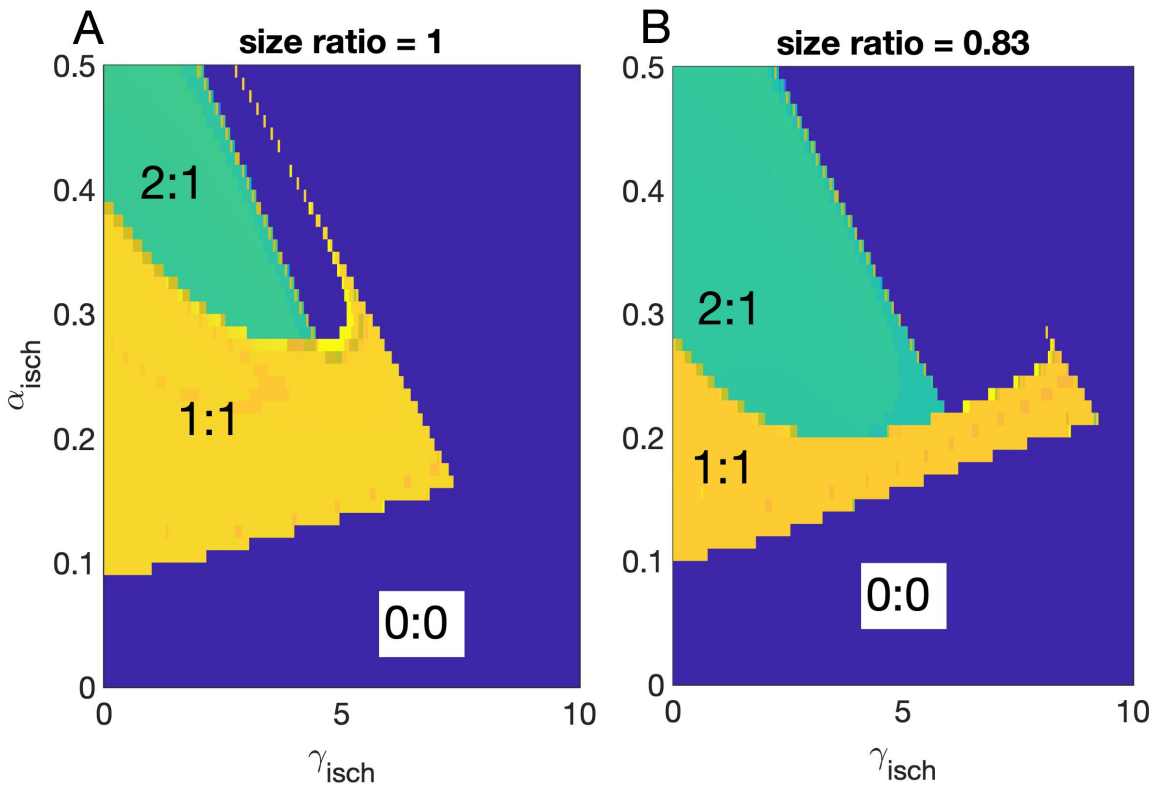

FIGURE 4.13. Ratio of frequency in ischemic/oscillatory cell to frequency in excitable cell, with a size ratio of 1 (A) and 0.83 (B), over a range of γ_{isch} and α_{isch} parameter values. Phase-locked pacing and period-doubling behavior both occur in a two-cell system depending on the relationship between α and γ in the ischemic cell. When the relative size of the excitable region increases, the regions of parameter space over which 1:1 and 2:1 pacing occur shift.

which pacing occurs, the γ_{isch} threshold for oscillations depends non-monotonically on size ratio. When size ratio is below ≈ 0.75, oscillation threshold in γ_{isch} increases with increased size ratio; however, for size ratio above ≈ 0.75 oscillation threshold *decreases* as size ratio increases.

Notably, the overall behavior of the two-cell model bears a strong resemblance to the behavior of the two-domain, spatially extended model. In particular, the dependence of the atrial cell's frequency on γ_{isch} and α_{isch} in the two-cell case (fig. 4.13) follows a similar qualitative pattern to the dependence of the frequency of the atrial region on the parameters γ_{isch} and α_{isch} in the two-domain model (particularly figs. 4.3 and 4.5). In both the two-cell and two-domain models, there is a region of $(\gamma_{isch}, \alpha_{isch})$-space over which 1:1 pacing occurs;

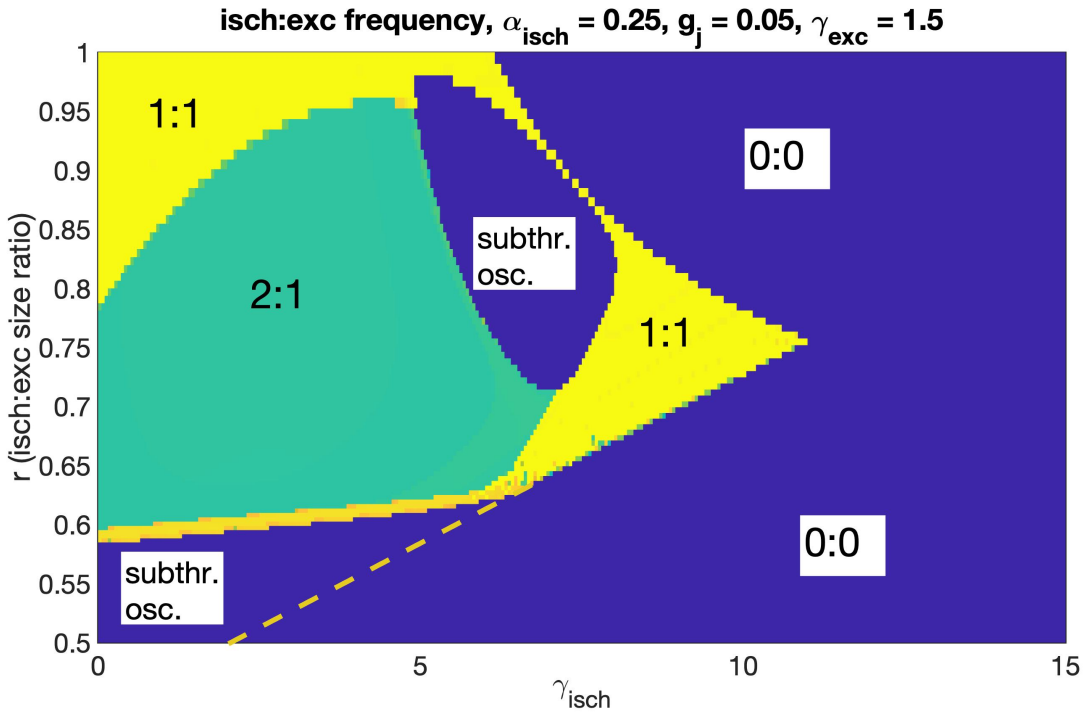

FIGURE 4.14. Ratio of frequency in ischemic/oscillatory cell to frequency in excitable cell for fixed $\alpha_{isch} = 0.25$, over a range of γ_{isch} and cell size ratio. For sufficiently high γ_{isch}, no pacing occurs. When γ_{isch} is sufficiently small, a large oscillatory cell paces an excitable cell, but reducing the size of the oscillatory/ischemic cell gives rise to period doubling. Further reduction of the ischemic cell size, for small γ_{isch}, leads to subthreshold oscillations. For intermediate values of γ_{isch}, a region of wave block occurs between $r \approx 0.72$ and $r \approx 0.98$.

increasing α_{isch} slightly with sufficiently small γ_{isch} results in 2:1 pacing; outside of these regions there is wave block. Most importantly, in both the full PDE and the two-cell model there is non-monotonic dependence of the threshold in γ_{isch} on curvature of the ischemic region. The similarity of these qualitative phenomena suggest that the atrial frequency, and the occurrence of 1:1 vs. 2:1, 1:0 or 0:0 pacing, are primarily determined by the bulk properties of current conduction between an oscillatory or bistable cell and an excitable cell.

4.5.2.2. *Analysis.*

Phase Plane Analysis

In order to analyze the mechanisms that drive the distinctions between different behaviors observed in our simulations, we study the phase plane for examples of the system in each

region of fig. 4.14. In figures 4.15 and 4.16, we visualize the time course for the voltage of each cell as well as the (v, w) phase plane for each cell when the size ratio $r_{isch}/r_{exc} = 0.74$.

When $\gamma_{isch} = 11$, in simulations, we observe two steady states for the system: (1) depolarization block, in which the SAN or ischemic cell rests at a depolarized potential while the excitable cell remains at its hyperpolarized resting state, and (2) wave block, in which both cells remain fixed at a hyperpolarized value. In fig. 4.15, we simulate the system with two different initial conditions. Panels A-C use an initial condition close to the depolarization block steady state, while D-F use an initial condition farther away from depolarization block. Panel A shows the (v_{isch}, w_{isch}) phase plane for the ischemic cell, with nullclines corresponding to no coupling (solid lines), v_{isch} nullcline with coupling current at the maximal voltage difference attained between the two cells in simulations (dashed line), and v nullcline at the final time-point of the simulation (dotted line). Panel B shows the (v_{exc}, w_{exc}) phase plane for the excitable cell. Panel C shows the time course for the membrane potentials of the ischemic cell (blue) and excitable cell (red). As shown in fig. 4.15A, the depolarization block steady state is characterized by the fact that the ischemic cell remains at an elevated (depolarized) membrane potential over time; the excitable cell never exerts enough hyperpolarizing "sink" current to destabilize this depolarized steady state. In contrast, when the initial difference between membrane potentials for the two cells is greater – as in fig. 4.15 D-F – the excitable cell exerts a stronger hyperpolarizing force on the ischemic cell, thereby pulling the v_{isch} nullcline down farther (compare dashed curves in fig. 4.15 panel A and panel D). This destabilizes the depolarized steady state for the ischemic cell, allowing the ischemic cell to hyperpolarize. With both cells hyperpolarized, the coupled v_{isch} nullcline shifts back up toward the solid curve in fig. 4.15D, and the coupled v_{exc} nullcline shifts toward the solid curve in panel E. Both cells reach an intermediate level close to hyperpolarization at the dotted nullclines in fig. 4.15 panels D and E. At this point, neither cell exerts a strong enough influence to elicit an action potential, and so both cells remain hyperpolarized, in the "wave suppression" steady state.

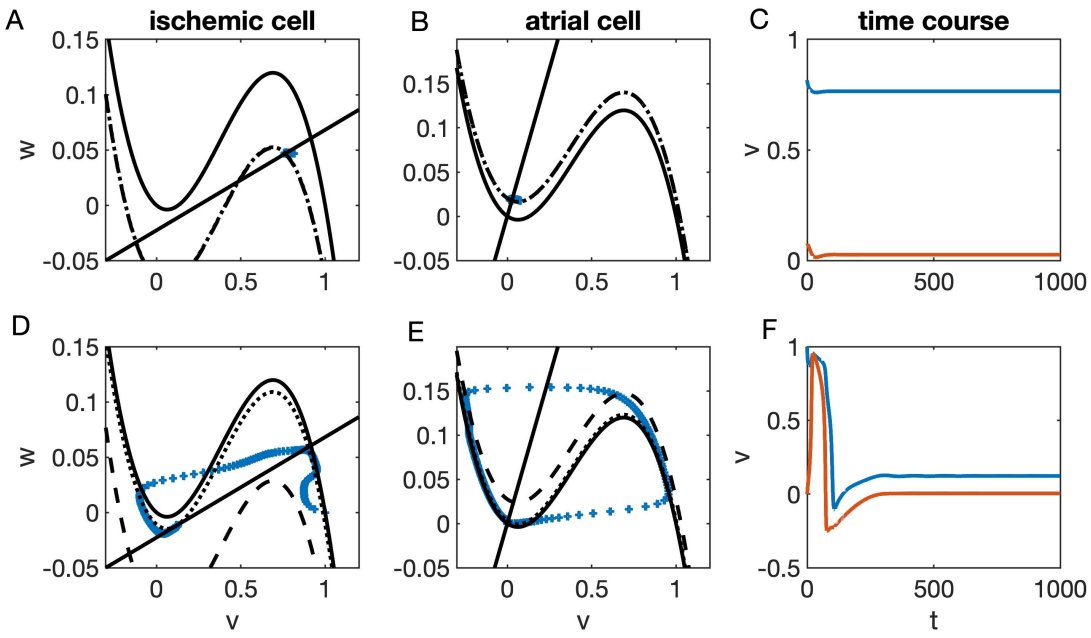

FIGURE 4.15. When $\gamma_{isch} = 11$ and $r_{isch}/r_{exc} = 0.74$, there is bistability between depolarization block and wave block. A-C use an initial condition close to depolarization block, while D-F use an initial condition with more depolarized v_{isch} and more hyperpolarized v_{exc}. A, D: phase plane for (v_{isch}, w_{isch}) uncoupled (solid lines), coupled with maximal current in simulation (dashed curve), and coupled with current from the final time-point in simulations (dotted curve). B, E: as in A and D for (v_{exc}, w_{exc}). C, F: time-course of v_{isch} (blue) and v_{exc} (red) for the two initial conditions. In C, v_{isch} remains depolarized, while in F, both cells hyperpolarize.

When $\gamma_{isch} = 9$, we again observe two distinct qualitative behaviors depending on the initial condition. When the initial condition is close to depolarization block, the ischemic cell becomes fixed at a depolarized membrane potential; the excitable cell remains at its hyperpolarized resting potential, but does not exert sufficient hyperpolarizing coupling current to pull the ischemic cell away from the depolarized steady state. In contrast, when the initial difference between membrane potentials for the two cells is greater, as in fig. 4.16 D-F, the excitable cell exerts a stronger hyperpolarizing force on the ischemic cell. The hyperpolarized excitable cell in its "recovery" phase pulls the v_{isch} nullcline down farther (compare dashed curves in fig. 4.16 panel A and panel D), destabilizing the depolarized steady state for the ischemic cell. This allows the ischemic cell to hyperpolarize, at which point both

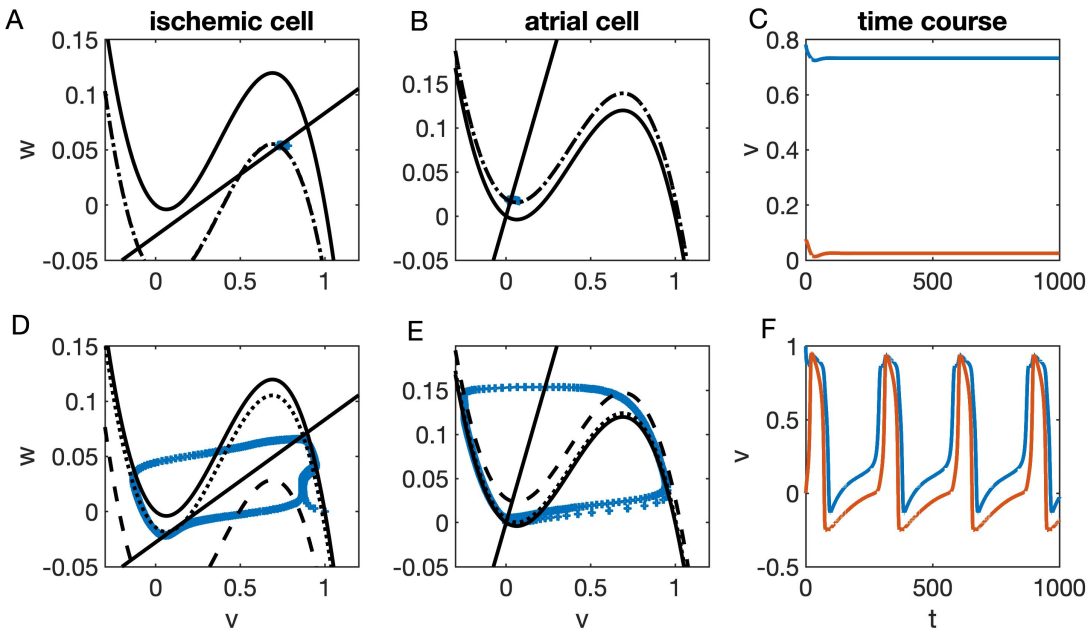

FIGURE 4.16. When $\gamma_{isch} = 9$ and $r_{isch}/r_{exc} = 0.74$, there is bistability between depolarization block and 1:1 pacing. A-C use an initial condition close to depolarization block, while D-F use an initial condition with more depolarized v_{isch} and more hyperpolarized v_{exc}. A, D: phase plane for (v_{isch}, w_{isch}) uncoupled (solid lines), coupled with maximal current in simulation (dashed curve), and coupled with current from the final time-point in simulations (dotted curve). B, E: as in A and D for (v_{exc}, w_{exc}). C, F: time-course of v_{isch} (blue) and v_{exc} (red) for the two initial conditions. In C, v_{isch} remains depolarized, while in F, both cells exhibit periodic action potentials in a 1:1 pattern.

cells are at similar membrane potentials and the coupling current therefore becomes very small. With a smaller coupling current, the coupled v_{isch} nullcline shifts back up toward the solid curve in fig. 4.16D, such that the ischemic cell is past its excitation threshold and immediately fires an action potential. This triggers an action potential in the excitable cell, which subsequently undergoes its own recovery and hyperpolarization process. The sequence then repeats, leading to oscillations (fig. 4.16F).

Bifurcation Analysis

We linearize around each steady state – wave suppression and depolarization block – and use the eigenvalues of the system at each point to assess the stability of the steady state over a range of r values, as well as to examine how the bifurcations in r shift as γ_{isch} changes (fig. 4.17). We define the parameter V_{ss} as the value of the membrane potential of the ischemic cell (v_{isch}) at the steady state. For $\gamma_{isch} = 4$ (blue curve), there is one steady state, which is stable for low r, or a small ischemic cell, undergoes a subcritical Hopf bifurcation (HB) at $r \approx 0.56$, and is unstable for higher r. The single steady state for $\gamma_{isch} = 4$ occurs at hyperpolarized membrane potential for low r, corresponding to wave suppression, but V_{ss} increases with r toward "depolarization block" ($V_{ss} > 0.5$) for r closer to 1. As γ_{isch} increases to 7, the two steady states separate from each other in v (red curve in fig. 4.17). The wave block steady state approaches $V_{ss} \approx 0$ as the depolarization block steady state approaches $V_{ss} \approx 1$. The depolarization block steady state is stable at high r, but undergoes a subcritical Hopf bifurcation and destabilizes as r decreases. As γ_{isch} increases, the range of size ratios r over which each steady state is stable widens; the HB for wave suppression shifts toward higher r while the HB for depolarization block shifts toward lower r (compare red curve with yellow and purple curves in fig. 4.17). As γ_{isch} increases further, the two HBs continue to shift independently of each other as the range of r values over which each steady state is stable widens (fig. 4.17 thick segments of each curve), and the unstable steady-state curve in the intermediate range of r folds (fig. 4.17 thin segments of each curve). For γ_{isch} above ≈ 8, there is a region of bistability between the two steady states.

We similarly use the eigenvalues of the system to assess the stability of each steady state over a range of γ_{isch} values for a fixed size ratio r, and to assess how the bifurcations in γ_{isch} shift as r changes (fig. 4.18). When $r = 1$ (purple), there is one steady state at depolarization block, which is stable for high γ_{isch} and destabilizes in a Hof bifurcation as γ_{isch} decreases to ≈ 5. For $r = 0.83$ (yellow curves), the HB for depolarization block shifts to slightly higher γ_{isch}, and a second branch steady states appears at lower V_{isch}. The lowest steady state is

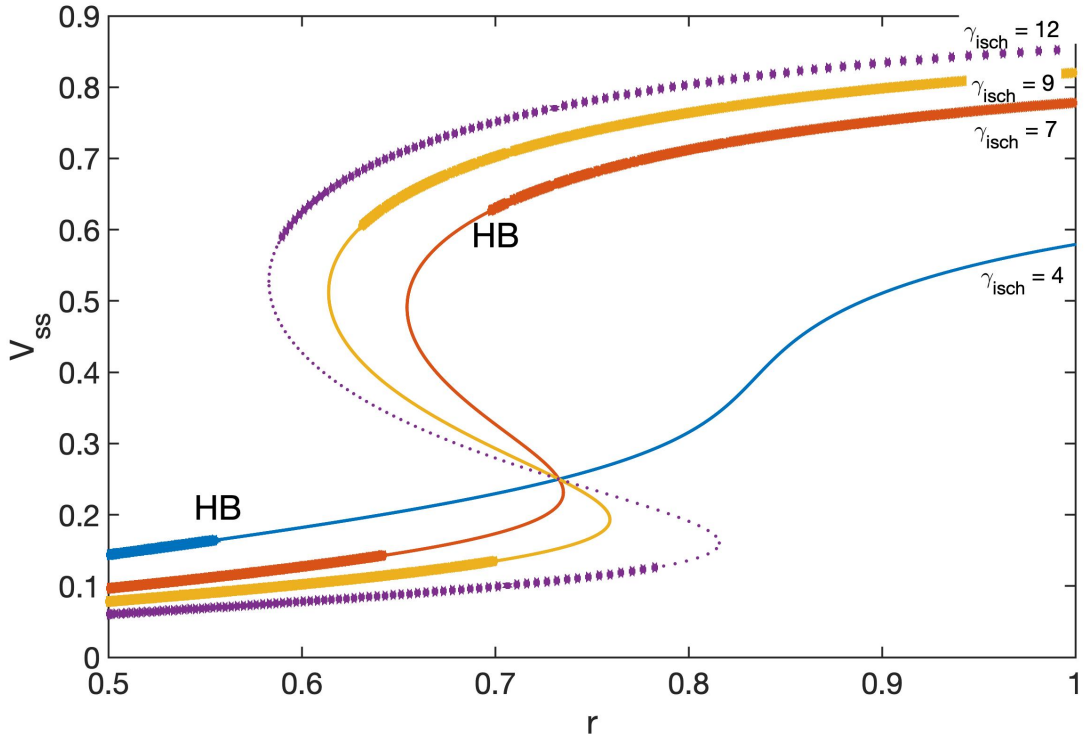

FIGURE 4.17. Bifurcation diagram in r for steady state values of V_{isch} in the two-cell FHN ODE, for four different values of γ_{isch}. Thick and thin segments of each curve denote stable and unstable steady states, respectively. For $\gamma_{isch} = 4$ (blue), there is one steady state, which is stable for low r and undergoes a subcritical Hopf bifurcation at $r \approx 0.56$ (HB). As γ_{isch} increases, the two steady states corresponding to wave suppression and depolarization block separate from each other in v (red). As γ_{isch} increases further, the range of r values over which each steady state is stable widens as the two HBs shift toward each other and then cross, and the intermediate range of r folds (yellow and purple curves). For γ_{isch} above ≈ 8, there is a region of bistability between the two steady states.

stable for high γ_{isch} between $\approx$ 14 and 15, destabilizing in a HB at $\gamma_{isch} \approx 14$. of As r decreases further to 0.67 (red curves), the intermediate branch of steady states breaks from the lower curve of steady states and joins the upper curve, while the two HBs both shift closer together, toward more intermediate γ_{isch}. Finally, when $r = 0.5$ (blue), the upper branch of steady states disappears, leaving only the "wave block" steady state, which is unstable for low γ_{isch} and undergoes an HB at $\gamma_{isch} \approx 2$.

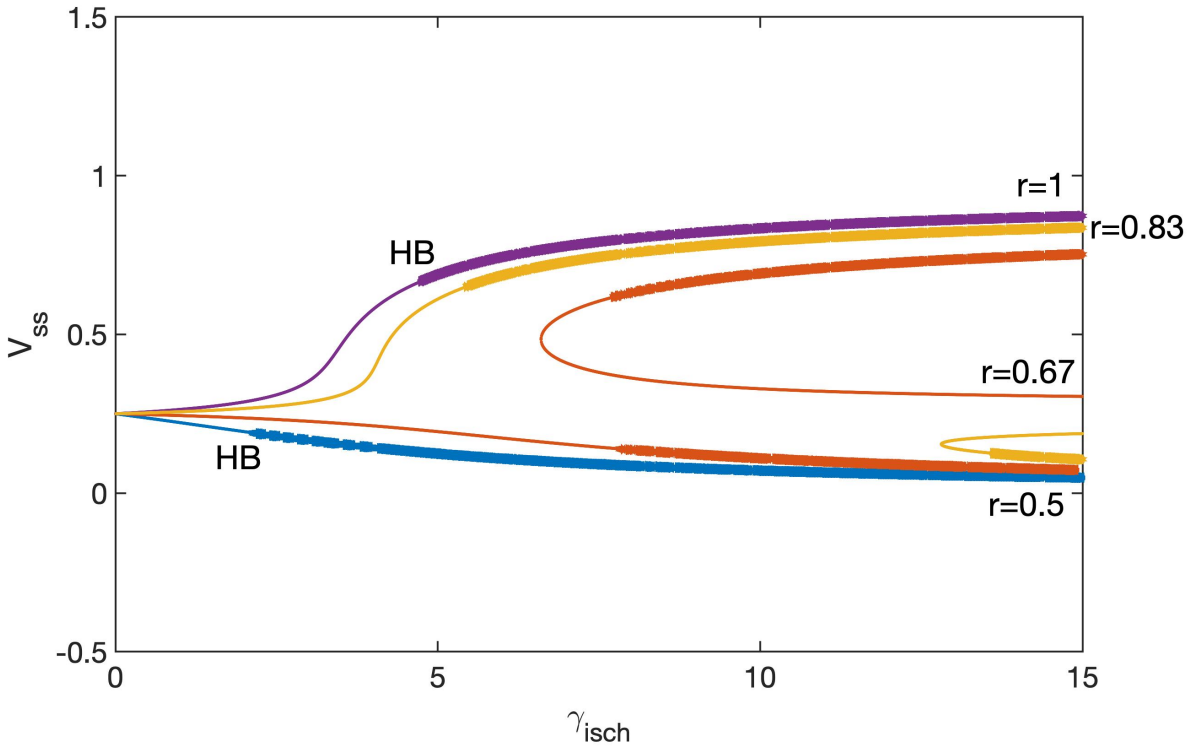

FIGURE 4.18. Bifurcation diagram in γ_{isch} for for steady state values of V_{isch} in the two-cell FHN ODE, for four different values of r. Thick and thin segments of each curve denote stable and unstable steady states, respectively. When $r = 1$ (purple), there is one steady state at depolarization block, which is stable for high γ_{isch} and destabilizes in a subcritical Hof bifurcation as γ_{isch} decreases to ≈ 5. For $r = 0.83$ (yellow curves), the HB for depolarization block shifts to slightly higher γ_{isch}, and a second branch steady states appears at lower V_{isch}. The lowest steady state is stable for high γ_{isch} between ≈ 14 and 15, destabilizing in a HB at $\gamma_{isch} \approx 14$. of As r decreases further to 0.67 (red curves), the intermediate branch of steady states breaks from the lower curve of steady states and joins the upper curve, while the two HBs both shift closer together, toward more intermediate γ_{isch}. When $r = 0.5$ (blue), the upper branch of steady states disappears, leaving only the "wave block" steady state, which is unstable for low γ_{isch} and undergoes an HB at $\gamma_{isch} \approx 2$

The result in fig. 4.18 suggests an explanation for the surprising result in [**69**]: as curvature increases, the subcritical Hopf bifurcation associated with depolarization block shifts toward higher γ_{isch}. This leads to the existence of a limit cycle in the portion of (γ_{isch}, r) space in which depolarization block is stable. Farther from the HB, the limit cycle becomes stable, generating stable oscillations in the system. These oscillations terminate in

a separate bifurcation, which occurs at higher γ_{isch} when curvature is higher. Based on the parameter conditions and boundary values used in [**69**], we expect that their system was restricted in a way that emphasizes the behavior associated with depolarization block, while omitting the threshold properties associated with the instability of the wave block steady state. Our results therefore generalize and contextualize theirs.

We compile and synthesize the results from our two-cell model and analysis in fig. 4.19. Results of our simulations are shown in the heatmap as in fig. 4.14, with yellow regions denoting 1:1 periodic action potentials, green region denoting 2:1 action potentials, and blue regions denoting no action potentials (or subthreshold oscillations). The curves denoting the locations of the Hopf bifurcations (HBs) for each of the two steady states – wave suppression and depolarization block – are shown in gray. Pink curves delineate the boundaries of regions of 1:1 periodic behavior of the system identified by XPPAUTO [**20**], which are bounded by different bifurcations in different regions of parameter space. Dotted pink lines denote estimated locations of bifurcations that the solver was unable to resolve. The simulated behavior of the system aligns well with the underlying bifurcations. Notably, the two Hopf bifurcations occur independently; while the HB curve for wave suppression slopes up, as is consistent with sink-source balance intuition, the HB curve for depolarization block slopes down, as in Teplenin [**69**]. The locations of each curve and their intersection justify the existence of bistability between the two steady states for high γ_{isch} and moderate r. We also observe bistability between depolarization block and oscillations for a small region of moderate r and moderate γ_{isch} (yellow wedge shape bounded by pink and gray curves, for $7 \leq \gamma \leq 11$ and $0.67 \leq r \leq 0.85$), as explained by the phase plane in fig. 4.16. While the lower boundary of this region is defined by the curve corresponding to the wave block Hopf bifurcation, the upper boundary of the region at which the oscillations terminate (pink curve at upper right boundary of yellow wedge) is defined by a second, unidentified bifurcation. We expect that this portion of the pink curve is defined by a saddle-node of periodics (SNP) bifurcation, because simulations in this section show that the oscillations arise with both a

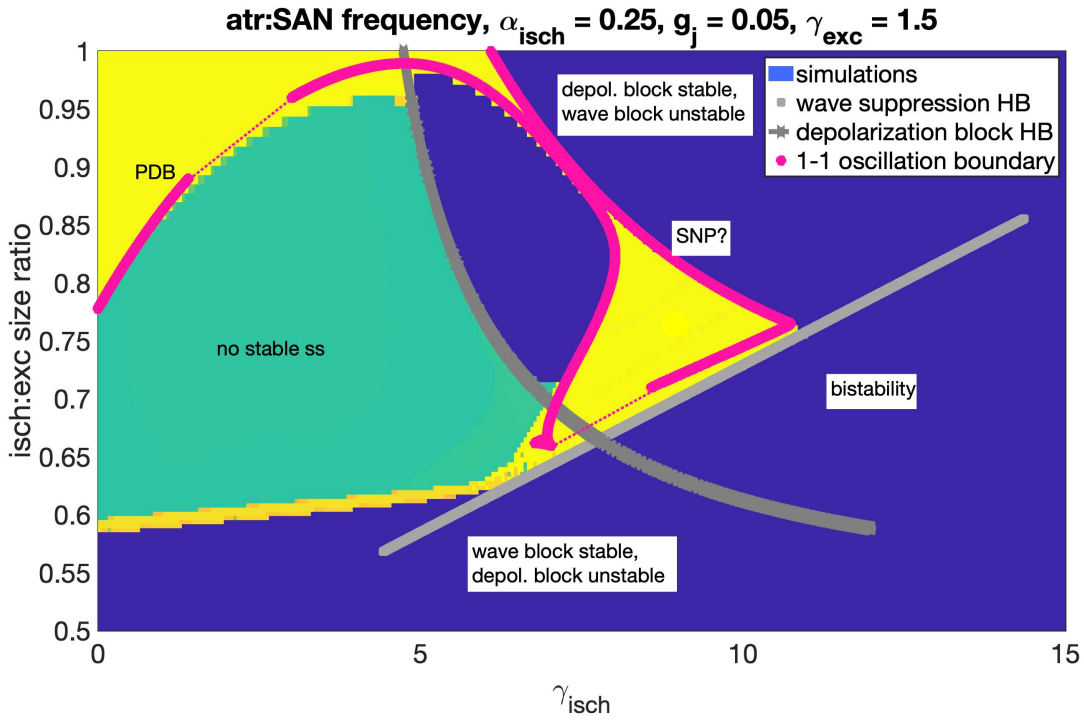

FIGURE 4.19. Two-parameter bifurcation diagram in γ_{isch} and r superimposed on simulated results. Background: simulated results with regions of 1:1, 2:1, 1:0, and 0:0 pacing as in fig. 4.14. Gray curves are locations of the subcritical Hopf bifurcation for each of the two steady states. Pink curves outline the regions of 1:1 periodic oscillations as predicted by bifurcations in the system.

characteristic amplitude and frequency, and the limit cycles arising from both HBs may exist in this region of parameter space. The negative slope of the pink SNP curve is therefore related to the negative slope of the dark gray curve corresonding to the subcritical HB for depolarization block, as the limit cycle arising from the HB gives rise to the oscillations that terminate at the SNP bifurcation. Thus, the negative slope of the threshold for the onset of oscillations for sufficiently high r is dependent on the existence of the "depolarization block" steady state. Finally, for lower γ_{isch}, the pink curve denoting the boundary of the region of 1-1 oscillations at relatively high r is defined by a period-doubling bifurcation (fig. 4.19 label "PDB"), which should be analyzed further.

4.6. Discussion

Results from the two-dimensional, two-domain PDE show a complex array of pacing outcomes depending on both the curvature and the excitability of the ischemic/oscillatory region. It is clear that under some parameter regimes, the geometry of a spontaneously active region has a nontrivial impact on its pacing properties. This impact is not monotonic: in some excitability regimes, increased curvature increases the threshold for the onset of oscillations, while in other parameter regimes, increased curvature decreases the threshold for the onset of oscillations. The former result is consistent with source-sink balance intuition [**66**], while the latter is in line with the counterintuitive result in [**69**] in which waves propagate from corners of a bistable region. Moreover, we observe both period-doubling and gradual period-increase transitions in distinct regions of parameter space. Our systematic PDE study is limited to radially symmetric domains, and therefore cannot fully explain the alternating edge-corner wave phenomenon observed in our simulations of square and triangular oscillatory regions. Rather, the complex dependence of pacemaking on both curvature and excitability suggests that the alternation phenomenon may arise as a result of the interplay of multiple mechanisms.

The results of our two-domain PDE simulations also help to explain and provide broader context for the counterintuitive finding in [**69**]. We demonstrate that indeed, in some parameter regimes, waves are expected to propagate from corners. In particular, we find that curvature destabilizes the stationary solution especially when the size of the ischemic region is moderate – not too small – and the excitability parameters are closer to the "bistable" regime of the FitzHugh-Nagumo system, characterized by high γ_{isch}. Given that Teplenin et al. use a moderate inner annular radius and a highly bistable ischemic region for their simulations and analysis, their result is consistent with our more general findings.

The results of our spatially extended single-domain model do not fully capture the dynamics of the two-domain model with either the Neumann or the Dirichlet boundary condition. In the single-domain model, simulations with the Dirichlet boundary condition only allow

the ischemic region to pace the excitable region when the excitable region is sufficiently close to exhibiting bistability, suggesting that in order for pacing to occur, the interface between the two regions must be able to oscillate. With a Neumann boundary condition, the 1D model describes regions of wave block and both 1:1 and 1:2 pacing. However, the Neumann 1D model does not capture the non-monotonicity of the changes to the γ_{isch} threshold for oscillations with respect to r_0, as we observed the two-domain PDE simulations. The single-domain model also only exhibits one stable stationary solution, and therefore fails to capture the difference between "depolarization block," the steady state in which the ischemic region remains at a depolarized potential, and "wave suppression," the steady state in which both the ischemic and excitable regions remain hyperpolarized. The fact that the reduction of the ischemic/oscillatory region to a boundary condition renders the model incapable of reproducing the results seen in the two-domain results suggests that the dynamic properties of the ischemic region are key to the complexity of behavior observed in the full model.

The qualitative behavior of the full two-domain PDE system, particularly with homogeneous Neumann boundary condition at l, is captured remarkably well by the two-cell model. In particular, we focus on the relationship between parameters $(\gamma_{isch}, \alpha_{isch})$ and the ability of the ischemic cell or region to drive periodic action potentials through the excitable cell or region. The comparison between planar and radial diffusion cases in the two-cell model (fig. 4.13A and B) analogous to the same comparison in the two-domain Neumann boundary condition model (fig. 4.5A and B). Moreover, the relationship between γ_{isch}, r, and the onset of oscillations in the two-cell model (fig. 4.14) is analogous to the same relationship in the two-domain PDE with Neumann BCs (fig. 4.6). In both models, reducing the relative size of the ischemic region – analogously, increasing the curvature of the ischemic region – results in an increase in the maximum value of γ_{isch} at which oscillations occur, as well as a widening of the range of γ_{isch} over which pacing occurs, for a moderately large ischemic region. This can be compared to the findings in [**69**], where it is noted that increased curvature results in a higher value of γ_{isch} at which oscillations arise as γ_{isch} is decreased from

a highly bistable value. However, our study additionally finds that for a sufficiently small ischemic region, *increasing* the size of curvature increases the width of the range of γ_{isch} over which pacing occurs. The latter trend is consistent with the conventional argument, based on source-to-sink ratio, that a current source with lower positive curvature is more likely to generate waves.

In the two-cell model, using both simulations and bifurcation analysis, we find that relative oscillatory/ischemic cell size – representing curvature at the interface – influences the ischemic cell's ability to pace the excitable cell in a complex manner. We observe two steady states in the system, which we refer to as "wave suppression" and "depolarization block": in the "wave suppression" steady state, both cells remain fixed at hyperpolarized resting potentials; in the "depolarization block" case, the excitable cell remains at its resting potential, while the ischemic cell rests at a depolarized potential. Each steady state undergoes a separate, subcritical Hopf bifurcation (HB) depending on both the size ratio between the two cells and the excitability of the ischemic cell. The two Hopf bifurcations occur independently of one another, and the threshold γ_{isch} for the two HBs depend on curvature in an opposite manner. While increased curvature decreases the threshold γ_{isch} for a HB of the wave suppression steady state, increased curvature increases the threhsold of γ_{isch} for a HB in the depolarization block steady state. The latter trend aligns with the result from [**69**], as they find that a stationary solution is destabilized at higher γ_{isch} for higher curvature. However, the threshold behavior for the "wave suppression" steady state affirms the conventional wisdom that a higher source:sink ratio increases the propensity for oscillations. We therefore expect the results of [**69**] to apply in the subset of cases in which depolarization block is an attainable steady state.

In addition to the two steady states, we also observe a stable limit cycle in some parameter regimes, in which periodic action potentials occur consistently in both cells. In some parameter regimes, this stable limit cycle coexists with the stable depolarization block steady state. As γ_{isch} increases, the limit cycle disappears and the system exhibits bistability

between the two steady states. For sufficiently low γ_{isch}, neither steady state is stable, and instead periodic action potentials are the only stable manifold of the system. In this parameter regime, we observe period-doubling wherein 1:1 oscillations transition to 2:1 oscillations as the relative size of the ischemic cell decreases.

The results from the two-cell system suggest the conditions in which a small ischemic region might be at greater risk for producing ectopic beats. When curvature is high, i.e., when the ischemic region is small, the depolarization block steady state is more likely to destabilize in oscillations. Thus, a small ischemic region with parameters in the regime for depolarization block (primarily high γ_{isch}) is more likely to produce ectopic beats than a small region with, say, lower γ_{isch} and higher α_{isch}, closer to the oscillatory regime. Finally, due to the non-monotonic dependence of the threshold defining the onset of oscillations on r, our results suggest the existence of an "optimal" size, at the intersection of the two curves of opposite slope defining the threshold for the onset of oscillation. At this intermediate size, oscillating waves are most likely to arise via the destabilization of either steady state.

The "depolarization block" steady state observed in both the two-cell and two-domain models seems to play an essential role in the counterintuitive dependence of oscillation threshold on curvature. In the two-cell model, we show explicitly that this steady state exhibits negative dependence of the HB threhsold on curvature, as opposed to positive dependence for the "wave suppresion" steady state. In line with this pattern, in our PDE simulations the far-field hyperpolarized Dirichlet boundary of $V(L) = 0$ appears to make a large difference to the behavior of the system. In some cases, oscillations arise as a result of the fixed, hyperpolarized boundary pulling the neighboring region of tissue down from an elevated, depolarized level. Indeed [**69**] uses this fixed hyperpolarized boundary at the ischemic-excitable interface, and explains the counterintuitive result with a similar "backward wave" description. In our two-cell model as well, the depolarization block phenomenon is eliminated when the excitable cell becomes sufficiently large that its coupling current can "pull" the bistable cell away from the depolarized membrane potential. Thus, the results from both the PDE and

two-cell ODE models support the argument that the depolarization block steady state is essential to the counterintuitive positive dependence of periodic wave stability on curvature.

The results of this work give rise to several important directions for future study. First, the bifurcation analysis in the two-cell model should be extended; as this study served as an exploratory first step, further analysis is needed fully identify the connections between steady states and limit cycles, thoroughly examine the period-doubling bifurcations, and relate the full bifurcation diagrams to the simulated results. The preliminary comparison between simulations and analysis suggests that the two align closely, and therefore that the full bifurcation picture will provide meaningful insight into explaining the results. Second, we observed interesting period-doubling behavior in the PDE. Our spectral analysis in the single-domain PDE was limited to linearization around the stationary solution and identifying bifurcations to the stability of this solution. An important future direction is to linearize the PDE around the periodic traveling wave, and investigate the spectral properties giving rise to the period-doubling bifurcation as well as any other bifurcations. It is also of interest, especially noting fig. 4.6, to investigate whether both the period-change phenomena in region 4 and region 5 are strictly period doubling, or if region 4 arises from a more gradual period-increase bifurcation. Finally, given that our PDE simulations were limited to radially symmetric domains, an important next step is to extend our study to ellipses and more complex shapes to fully examine how the predictions generated by our results apply in practice to a more realistic scenario with non-homogeneous curvature around the ischemic region.

Bibliography

[1] S. Alonso, R. W. D. Santos, and M. Bär, *Reentry and ectopic pacemakers emerge in a three-dimensional model for a slab of cardiac tissue with diffuse microfibrosis near the percolation threshold*, PLoS ONE, 11 (2016), p. e0166972.

[2] R. K. Amanfu and J. J. Saucerman, *Modeling the Effects of β1-Adrenergic Receptor Blockers and Polymorphisms on Cardiac Myocyte Ca2+ Handling*, Molecular Pharmacology, 86 (2014), pp. 222–230.

[3] J. L. Ashton, M. L. Trew, I. J. Legrice, D. J. Paterson, J. F. Paton, A. M. Gillis, and B. H. Smaill, *Shift of leading pacemaker site during reflex vagal stimulation and altered electrical source-to-sink balance*, The Authors. The Journal of Physiology C, 597 (2019), pp. 3297–3313.

[4] T. Banyasz, Z. Jian, B. Horvath, S. Khabbaz, L. T. Izu, and Y. Chen-Izu, *Beta-adrenergic stimulation reverses the I Kr–I Ks dominant pattern during cardiac action potential*, Pflugers Archiv European Journal of Physiology, 466 (2014), pp. 2067–2076.

[5] D. M. Bers, *Calcium Cycling and Signaling in Cardiac Myocytes*, Annual Review of Physiology, 70 (2008), pp. 23–49.

[6] M. Bohm and C. Maack, *Treatment of heart failure with beta-blockers. Mechanisms and results*, Basic Research in Cardiology, 95 (2000), p. 38.

[7] A. Bouzamondo, J.-S. Hulot, P. Sanchez, and P. Lechat, *Beta-blocker benefit according to severity of heart failure*, European Journal of Heart Failure, 5 (2003), pp. 281–289.

[8] M. Boyett, H. Honjo, and I. Kodama, *The sinoatrial node, a heterogeneous pacemaker structure*, Cardiovascular Research, 47 (2000), pp. 658–687.

[9] M. Boyett, S. Inada, S. Yoo, J. Li, J. Liu, J. Tellez, I. Greener, H. Honjo, R. Billeter, M. Lei, H. Zhang, I. Efimov, and H. Dobrzynski, *Connexins in the Sinoatrial and Atrioventricular Nodes*, in Cardiovascular Gap Junctions, vol. 42, KARGER, Basel, 2006, pp. 175–197.

[10] M. R. Boyett, H. Dobrzynski, M. K. Lancaster, S. A. Jones, H. Honjo, and I. Kodama, *Sophisticated Architecture is Required for the Sinoatrial Node to Perform Its Normal Pacemaker Function*, Journal of Cardiovascular Electrophysiology, 14 (2003), pp. 104–106.

[11] P. M. Boyle, T. Zghaib, S. Zahid, R. L. Ali, D. Deng, W. H. Franceschi, J. B. Hakim, M. J. Murphy, A. Prakosa, S. L. Zimmerman, H. Ashikaga, J. E. Marine, A. Kolandaivelu, S. Nazarian, D. D. Spragg, H. Calkins, and N. A. Trayanova, *Computationally guided personalized targeted ablation of persistent atrial fibrillation*, Nature Biomedical Engineering, 3 (2019), pp. 870–879.

[12] H. Brunner-La Rocca, M. Esler, G. Jennings, and D. Kaye, *Effect of cardiac sympathetic nervous activity on mode of death in congestive heart failure*, European Heart Journal, 22 (2001), pp. 1136–1143.

[13] A. Cannavo, D. Liccardo, and W. J. Koch, *Targeting cardiac β-adrenergic signaling via GRK2 inhibition for heart failure therapy*, Frontiers in Physiology, 4 SEP (2013), pp. 1–7.

[14] C. E. Clancy and Y. Rudy, *Linking a genetic defect to its cellular phenotype in a cardiac arrhythmia*, Nature, 400 (1999), pp. 566–569.

[15] S. R. Coppen, I. Kodama, M. R. Boyett, H. Dobrzynski, Y. Takagishi, H. Honjo, H. I. Yeh, and N. J. Severs, *Connexin45, a major connexin of the rabbit sinoatrial node, is co- expressed with connexin43 in a restricted zone at the nodal-crista terminalis border*, Journal of Histochemistry and Cytochemistry, 47 (1999), pp. 907–918.

[16] R. Coronel, R. Wilders, A. O. Verkerk, R. F. Wiegerinck, D. Benoist, and O. Bernus, *Electrophysiological changes in heart failure and their implications for arrhythmogenesis*, Biochimica et Biophysica Acta - Molecular Basis of Disease, 1832 (2013), pp. 2432–2441.

[17] J. M. Cruickshank, *Beta-blockers continue to surprise us*, European Heart Journal, 21 (2000), pp. 354–364.

[18] T. Desplantez, E. Dupont, N. J. Severs, and R. Weingart, *Gap junction channels and cardiac impulse propagation*, Journal of Membrane Biology, 218 (2007), pp. 13–28.

[19] T. Desplantez, D. Halliday, E. Dupont, and R. Weingart, *Cardiac connexins Cx43 and Cx45: Formation of diverse gap junction channels with diverse electrical properties*, Pflugers Archiv European Journal of Physiology, 448 (2004), pp. 363–375.

[20] G. Ermentrout, *Simulating, Analyzing, and Animating Dynamical Systems*, 2002.

[21] V. V. Fedorov, R. B. Schuessler, M. Hemphill, C. M. Ambrosi, R. Chang, A. S. Voloshina, K. Brown, W. J. Hucker, and I. R. Efimov, *Structural and functional evidence for discrete exit pathways that connect the canine sinoatrial node and atria*, Circulation Research, 104 (2009), pp. 915–923.

[22] V. G. Florea and J. N. Cohn, *The autonomic nervous system and heart failure*, Circulation Research, 114 (2014), pp. 1815–1826.

[23] K. Freeman, W. Tao, H. Sun, M. H. Soonpaa, and M. Rubart, *In situ three-dimensional reconstruction of mouse heart sympathetic innervation by two-photon excitation fluorescence imaging*, Journal of Neuroscience Methods, 221 (2014), pp. 48–61.

[24] E. Grandi and C. M. Ripplinger, *Antiarrhythmic mechanisms of beta blocker therapy*, aug 2019.

[25] J. Guckenheimer and P. Holmes, *Nonlinear Oscillations, Dynamical Systems, and Bifurcations of Vector Field... - Google Books*, Springer, New York, 7 ed., 2002.

[26] M. R. Guevara, A. C. van Ginneken, and H. J. Jongsma, *Patterns of Activity in a Reduced Ionic Model of a Cell from the Rabbit Sinoatrial Node*, Chaos in Biological Systems, (1987), pp. 5–12.

[27] A. S. HARRIS, *Delayed development of ventricular ectopic rhythms following experimental coronary occlusion.*, Circulation, 1 (1950), pp. 1318–1328.

[28] J. S. Hayes, L. L. Brunton, and S. E. Mayer, *Selective Activation of Particulate CAMP-dependent Protein Kinase by Isoproterenol and Prostaglandin E_1*, THE JOURNAL OF BIOLOGICAL CHEMISTRY, 255 (1980), pp. 5113–5119.

[29] N. Herring, M. Kalla, and D. J. Paterson, *The autonomic nervous system and cardiac arrhythmias: current concepts and emerging therapies*, Nature Reviews Cardiology, (2019).

[30] R. V. Iancu, S. W. Jones, and R. D. Harvey, *Compartmentation of cAMP signaling in cardiac myocytes: A computational study*, Biophysical Journal, 92 (2007), pp. 3317–3331.

[31] R. V. Iancu, G. Ramamurthy, and R. D. Harvey, *Spatial and temporal aspects of cAMP signalling in cardiac myocytes*, Clinical and Experimental Pharmacology and Physiology, 35 (2008), pp. 1343–1348.

[32] H. Irisawa and A. Noma, *Pacemaker Mechanisms of Rabbit Sinoatrial Node Cells*, Springer, Dordrecht, 1982, pp. 35–51.

[33] M. J. Janse, *Electrophysiological changes in heart failure and their relationship to arrhythmogenesis*, Cardiovascular Research, 61 (2004), pp. 208–217.

[34] R. W. Joyner and F. J. van Capelle, *Propagation through electrically coupled cells. How a small SA node drives a large atrium*, Biophysical Journal, 50 (1986), pp. 1157–1164.

[35] J. Keener and J. Sneyd, *Mathematical Physiology*, vol. 8, Springer, 2 ed., 2009.

[36] G. Kember, J. Ardell, K. Shivkumar, and J. Armour, *Recurrent myocardial infarction: Mechanisms of free-floating adaptation and autonomic derangement in networked cardiac neural control*, PLoS ONE, 12 (2017).

[37] D. Kotecha, M. D. Flather, D. G. Altman, J. Holmes, G. Rosano, J. Wikstrand, M. Packer, A. J. Coats, L. Manzano, M. Böhm, D. J. van Veldhuisen, B. Andersson, H. Wedel, T. G. von Lueder, A. S. Rigby, Å. Hjalmarson, J. Kjekshus, and J. G. Cleland, *Heart Rate and Rhythm and the Benefit of Beta-Blockers in Patients With Heart Failure*, Journal of the American College of Cardiology, 69 (2017), pp. 2885–2896.

[38] E. G. Lakatta, V. A. Maltsev, and T. M. Vinogradova, *A Coupled SYSTEM of intracellular Ca2+ clocks and surface membrane voltage clocks controls the timekeeping mechanism of the heart's pacemaker*, mar 2010.

[39] L. Leybaert, P. D. Lampe, S. Dhein, B. R. Kwak, P. Ferdinandy, E. C. Beyer, D. W. Laird, C. C. Naus, C. R. Green, and R. Schulz, *Connexins in cardiovascular and neurovascular health and disease: Pharmacological implications*, Pharmacological Reviews, 69 (2017), pp. 396–478.

[40] K. Liu, D. Li, G. Hao, D. McCaffary, O. Neely, L. Woodward, D. Ioannides, C. J. Lu, M. Brescia, M. Zaccolo, H. Tandri, O. A. Ajijola, J. L. Ardell, K. Shivkumar, and D. J. Paterson, *Phosphodiesterase 2A as a therapeutic target to restore cardiac neurotransmission during sympathetic hyperactivity*, JCI Insight, 3 (2018).

[41] C. Ly and S. H. Weinberg, *Analysis of heterogeneous cardiac pacemaker tissue models and traveling wave dynamics*, Journal of Theoretical Biology, 459 (2018), pp. 18–35.

[42] A. Lymperopoulos, G. Rengo, and W. J. Koch, *Adrenergic nervous system in heart failure: Pathophysiology and therapy*, Circulation Research, 113 (2013), pp. 739–753.

[43] A. Madamanchi, *B-Adrenergic Receptor Signaling in Cardiac Function and Heart Failure*, McGill Journal of Medicine, 10 (2007), pp. 99–104.

[44] T. A. Matsuyama, S. Inoue, Y. Kobayashi, T. Sakai, T. Saito, T. Katagiri, and H. Ota, *Anatomical diversity and age-related histological changes in the human right atrial posterolateral wall*, Europace, 6 (2004), pp. 307–315.

[45] E. Meyer, C. Clancy, and T. Lewis, *Dynamics of adrenergic signaling in cardiac myocytes and implications for pharmacological treatment*, Journal of Theoretical Biology, 519 (2021), p. 110619.

[46] O. Monfredi, H. Dobrzynski, T. Mondal, M. R. Boyett, and G. M. Morris, *The anatomy and physiology of the sinoatrial node-A contemporary review*, PACE - Pacing and Clinical Electrophysiology, 33 (2010), pp. 1392–1406.

[47] A. Najafi, V. Sequeira, D. W. Kuster, and J. van der Velden, *β-adrenergic receptor signalling and its functional consequences in the diseased heart*, European Journal of Clinical Investigation, 46 (2016), pp. 362–374.

[48] T. Nikolaidou, O. V. Aslanidi, H. Zhang, and I. R. Efimov, *Structure-function relationship in the sinus and atrioventricular nodes*, in Pediatric Cardiology, vol. 33, Springer, aug 2012, pp. 890–899.

[49] M. Nishimura, T. Tokoro, M. Nishida, T. Hashimoto, H. Kobayashi, S. Yamazaki, R. Imai, K. Okino, N. Iwamoto, H. Takahashi, and T. Ono, *Sympathetic overactivity and sudden cardiac death among hemodialysis patients with left ventricular hypertrophy*, International Journal of Cardiology, 142 (2010), pp. 80–86.

[50] R. S. Oliveira, S. Alonso, F. O. Campos, B. M. Rocha, J. F. Fernandes, T. Kuehne, and R. W. dos Santos, *Ectopic beats arise from micro-reentries near infarct regions in simulations of a patient-specific heart model*, Scientific Reports, 8 (2018), pp. 1–14.

[51] R. V. Oren and C. E. Clancy, *Determinants of heterogeneity, excitation and conduction in the sinoatrial node: A model study*, PLoS Computational Biology, 6 (2010).

[52] B. E. Peercy and J. P. Keener, *Coupled Cell Model of Border Zone Arrhythmias*, SIAM Journal on Applied Dynamical Systems, 4 (2005), pp. 679–710.

[53] P. Penela, C. Murga, C. Ribas, V. Lafarga, and F. M. Jr, *The complex G protein-coupled receptor kinase 2 (GRK2) interactome unveils new physiopathological targets*, (2010), pp. 821–832.

[54] A. Prakosa, H. J. Arevalo, D. Deng, P. M. Boyle, P. P. Nikolov, H. Ashikaga, J. J. Blauer, E. Ghafoori, C. J. Park, R. C. Blake, F. T. Han, R. S. MacLeod, H. R. Halperin, D. J. Callans, R. Ranjan, J. Chrispin, S. Nazarian, and N. A. Trayanova, *Personalized virtual-heart technology for guiding the ablation of infarct-related ventricular tachycardia*, Nature Biomedical Engineering, 2 (2018), pp. 732–740.

[55] M. Rackauskas, M. M. Kreuzberg, M. Pranevicius, K. Willecke, V. K. Verselis, and F. F. Bukauskas, *Gating properties of heterotypic gap junction channels formed of connexins 40, 43, and 45*, Biophysical Journal, 92 (2007), pp. 1952–1965.

[56] J. Rinzel and J. P. Keener, *Hopf bifurcation to Repetitive Activity in Nerve*, SIAM Journal of Applied Mathematics, 43 (1983), pp. 2–6.

[57] C. M. Ripplinger, S. F. Noujaim, and D. Linz, *The nervous heart*, Progress in Biophysics and Molecular Biology, 120 (2016), pp. 199–209.

[58] D. Sánchez-Quintana, J. A. Cabrera, J. Farré, V. Climent, R. H. Anderson, and S. Y. Ho, *Sinus node revisited in the era of electroanatomical mapping and catheter ablation*, Heart, 91 (2005), pp. 189–194.

[59] J. J. Saucerman, L. L. Brunton, A. P. Michailova, and A. D. McCulloch, *Modeling β-Adrenergic Control of Cardiac Myocyte Contractility in Silico*, Journal of Biological Chemistry, 278 (2003), pp. 47997–48003.

[60] J. J. Saucerman, S. N. Healy, M. E. Belik, J. L. Puglisi, and A. D. McCulloch, *Proarrhythmic consequences of a KCNQ1 AKAP-binding domain mutation: Computational models of whole cells and heterogeneous tissue*, Circulation Research, 95 (2004), pp. 1216–1224.

[61] B. J. Scherlag, N. El Sherif, R. Hope, and R. Lazzara, *Characterization and localization of ventricular arrhythmias resulting from myocardial ischemia and infarction*, Circulation Research, 35 (1974), pp. 372–383.

[62] S. M. Schumacher, E. Gao, W. Zhu, X. Chen, J. Kurt Chuprun, A. M. Feldman, J. J. Tesmer, and W. J. Koch, *Paroxetine-mediated GRK2 inhibition reverses cardiac dysfunction and remodeling after myocardial infarction*, Science Translational Medicine, 7 (2015), pp. 277ra31–277ra31.

[63] P. J. Schwartz, S. Priori, C. Spazzolini, A. Moss, G. Vincent, C. Napolitano, I. Denjoy, P. Guicheney, G. Breithardt, M. Keating, J. Towbin, B. AH, P. Brink, and A. Wilde, *Genotype-phenotype correlation in the long-QT syndrome: gene-specific triggers for life-threatening arrhythmias.*, Circulation, 103 (2001), pp. 89–95.

[64] M. A. Schwemmer and T. J. Lewis, *The Theory of Weakly Coupled Oscillators.*

[65] A. R. Soltis and J. J. Saucerman, *Synergy between CaMKII substrates and β-adrenergic signaling in regulation of cardiac myocyte Ca2 handling*, Biophysical Journal, 99 (2010), pp. 2038–2047.

[66] P. Spector, *Principles of cardiac electric propagation and their implications for re-entrant arrhythmias*, Circulation: Arrhythmia and Electrophysiology, 6 (2013), pp. 655–661.

[67] D. C. Spray and M. V. L. Bennett, *JUNCTIONS*, (1985), pp. 281–303.

[68] I. Ten Velde, B. De Jonge, E. E. Verheijck, M. J. Van Kempen, L. Analbers, D. Gros, and H. J. Jongsma, *Spatial distribution of connexin43, the major cardiac gap junction protein, visualizes the cellular network for impulse propagation from sinoatrial node to atrium*, Circulation Research, 76 (1995), pp. 802–811.

[69] A. S. Teplenin, H. Dierckx, A. A. De Vries, D. A. Pijnappels, and A. V. Panfilov, *Paradoxical Onset of Arrhythmic Waves from Depolarized Areas in Cardiac Tissue Due to Curvature-Dependent Instability*, Physical Review X, 8 (2018), pp. 1–14.

[70] G. F. Tomaselli and D. P. Zipes, *What Causes Sudden Death in Heart Failure?*, (2004).

[71] G. Tse, *Mechanisms of cardiac arrhythmias*, apr 2016.

[72] S. D. Unudurthi, R. M. Wolf, and T. J. Hund, *Role of sinoatrial node architecture in maintaining a balanced source-sink relationship and synchronous cardiac pacemaking*, Frontiers in Physiology, 5 (2014), p. 446.

[73] G. Vincent, P. J. Schwartz, I. Denjoy, H. Swan, C. Bithell, and C. Spazzolini, *High efficacy of β-blockers in long-QT syndrome type 1*, Circulation, (2009), pp. 215–221.

[74] J. N. Weiss, A. Garfinkel, H. S. Karagueuzian, P. S. Chen, and Z. Qu, *Early afterdepolarizations and cardiac arrhythmias*, Heart Rhythm, 7 (2010), pp. 1891–1899.

[75] T. Zaglia and M. Mongillo, *Cardiac sympathetic innervation, from a different point of (re)view*, The Journal of Physiology, 595 (2017), pp. 3919–3930.